1-1-2002

Modeling polymeric systems.

Paul M. Welch
University of Massachusetts Amherst

MODELING POLYMERIC SYSTEMS

A Dissertation Presented

by

PAUL M. WELCH

Submitted to the Graduate School of the
University of Massachusetts Amherst in partial fulfillment
of the requirements for the degree of

DOCTOR OF PHILOSOPHY

May 2002

Department of Polymer Science and Engineering

MODELING POLYMERIC SYSTEMS

A Dissertation Presented

by

PAUL M. WELCH

Approved as to style and content by:

M. Muthukumar, Chair

Samuel P. Gido, Member

David A. Hoagland, Member

Thomas P. Russell, Member

Thomas J. McCarthy, Department Head
Polymer Science and Engineering

Dedication

To my companion, tutor, fellow scientist, and wife. To Cindy.

ACKNOWLEDGMENTS

I owe a debt of gratitude to many great professors and students for their tutelage and friendship. In particular, I thank my committee members for their guidance throughout my time in Amherst. Their direction has been vital not only to my research, but also to my development as a member of the scientific community. My committee chair merits special mention. Muthu's energy, creativity, and intellectual acumen made our research a constant joy and challenge. He is a true pearl amongst educators. I also thank my fellow research group members, Vivek, Gus, Chester, Dirk, Lars, Joey, Kings, Ashok, Shulan, Yvonne, Radu, Sonoko, and Joe. The rich environment they cultivated was a source of motivation and an education in itself. I am fortunate to have been accompanied on my adventure by such active minds! I also thank the faculty of my undergraduate institution for fostering my curiosity while still new to scientific endeavors, especially Dr. C. L. McCormick who provided me with my first research experience. I am deeply in debt to my wife, Cindy. Her patience, support, and friendship have carried me far. Thanks to all of these, for the past thirteen years my passion and my work have been one and the same. I hope that I find such companions to help maintain this link in the years to come. Finally, I thank my Creator for instilling in me an earnest desire for one of His greatest gifts to man, the opportunity to discover.

It is the glory of God to conceal a matter; to search out a matter is the glory of kings. (Proverbs 25:2)

ABSTRACT

MODELING POLYMERIC SYSTEMS

MAY 2002

PAUL M. WELCH, B.S., UNIVERSITY OF SOUTHERN MISSISSIPPI

M.S., UNIVERSITY OF SOUTHERN MISSISSIPPI

PH.D., UNIVERSITY OF MASSACHUSETTS, AMHERST

Directed by: Professor M. Muthukumar

This thesis investigates the physics of various polymeric systems via the tool of computer simulation. The problems addressed include the tunable conformations of dendritic polyelectrolytes, the complexation of oppositely charged linear polyelectrolytes to charged dendrimers, the molecular mechanisms of polymer crystallization, and the retractive response of polymers perturbed from their equilibrium conformations. The algorithms employed include both equilibrium Metropolis Monte Carlo and Brownian dynamics methods. The computational investigations are augmented by scaling and variational theory treatments. The results of these studies complement experimental ventures in the respective fields and provide new insight into the limitations of existing theoretical descriptions.

TABLE OF CONTENTS

LIST OF FIGURES

CHAPTER 1

INTRODUCTION

1.1 Simulation as Experiment

Traditionally, scientific investigations were easily classified as either experimental or theoretical. Over the past 50 years, however, computer simulation emerged as a bridge between these two modes of research. Though computer modeling has primarily been applied by theorists to move beyond the limits of mathematical tractability, the rapid growth of the availability and speed of digital computers is beginning to effect a major research paradigm shift toward a new kind of "experiment," the computer experiment. The interdisciplinary field of polymer science has long embraced this approach to investigation, and the modern capabilities of even personal computers means that the day of the computational polymer scientist has certainly arrived. Within the coming decades computational scientists may indeed deliver the oft promised economical alternative to bench top chemical exploration. Today, however, the appeal of computer experiments for polymer scientists lies in the ability of simulations to provide a molecular level view of the physical behavior of polymers. This thesis exploits this ability to provide new insights into both old challenges and new problems. The diversity of the problems addressed here testifies to the power and flexibility of computer simulations.

1.2 Dendrimer Studies

Chapters 2 and 3 address the nature of a new class of highly branched polymers known as dendrimers for their tree like topology. Specifically, Chapter 2 demonstrates that the shape of the intramolecular density profile of dendritic polyelectrolytes in solution can be tailored by varying the ionic strength of the solvent. Further, the simulations show that a reversible transition between a "dense core" and a "dense shell" dendritic structure may be observed as the ionic strength is cycled from high to low. Chapter 2 also presents the necessary conditions in terms of salt concentration and various molecular variables such as generation number, spacer length, and number of charges, for realizing the potential of dendrimers as hosts in controlled-release and similar applications.

Chapter 3 investigates the interaction between oppositely charged linear and dendritic polyelectrolytes. Much of the experimental effort to realize the possible uses of dendrimers has focused on the complexation of charged dendrimers to oppositely charged polyelectrolytes to form controlled delivery systems. Employing computer simulation and theory, Chapter 3 presents a molecular-level picture of these guest-host aggregates and the conditions necessary for forming them. Specifically, the simulations examine the equilibrium and dynamic complexation behavior of a monocentric dendrimer with charged terminal groups to a flexible, oppositely charged polyelectrolyte. Three different types of complexes are noted depending upon the solution ionic strength and the sizes of the dendrimer and chain. This study finds that a dendrimer may encapsulate a chain, a chain and a dendrimer may mutually interpenetrate, or a unique "chain-walking" phenomenon may be observed. The critical conditions for complexation, density profiles of the polyelectrolyte and the dendrimer in the complex, and the curious dynamics observed are

discussed. A closed formula is proposed via a variational approach to describe the critical conditions for complexation between a dendrimer and a polyelectrolyte.

1.3 Polymer Crystallization Studies

Chapter 4 focuses on the long-standing challenges of polymer crystallization. This chapter delineates the results of Brownian dynamics simulations of the early and intermediate stages of polymer crystallization from dilute solution. The simulations demonstrate that the mechanism of polymer crystallization in the earliest stages is nucleation and growth, in contradiction to the recently proposed spinodal mode. Chapter 4 also details a study of the mechanism of fold thickness selection, the activity at the growth front, and the internal dynamics of a growing polymer crystal. These Brownian dynamics simulations show that (1) entropic barriers control the selection of the initial lamellar thickness, (2) growth at the crystalline interface is chain adsorption followed by crystallographic registry, and (3) that lamellar thickening is a highly cooperative process requiring the mobility of all chains in the crystal. These results, especially the latter, challenge the conventional Lauritzen-Hoffman theory and its generalizations.

1.4 Single Molecule Force Spectroscopy Studies

Chapter 5 demonstrates the use of a Brownian dynamics simulation technique for investigating the response of chains to an external force. The specific system examined is the simple case of an excluded volume chain tethered to an athermal surface pulled upon by a model atomic force microscopy probe. This system, while

simple, only recently was examined experimentally. The results from this chapter show excellent agreement with the experimental observations and illustrate how to reconstruct the underlying equilibrium free energy of a polymer from such non-equilibrium processes.

1.5 Pedagogical Goals

Finally, while the results of these computer experiments comprise my primary scientific contributions to the field of polymer science, I also hope that this thesis will be of pedagogical value and serve as an aid to future students by providing detailed examples of how to implement computer simulations of polymers. With this goal in mind, Appendix B and the accompanying CD-ROM provide the schematic for the computational facility I used throughout this work and the source code for the version of my simulation software that provided most of these results. In addition to the problems addressed in this thesis, I have applied variations of this software to many other problems such as polymer translocation through a hole, charged dendrimer adsorbtion to oppositely charged surfaces, and single molecule force spectroscopy on a variety of polymer systems including double stranded DNA, adsorbed linear polyelectrolytes, and tethered polymer crystals. The code therefore offers a rich mine of data awaiting further excavation.

CHAPTER 2

TUNING THE DENSITY PROFILE OF DENDRITIC POLYELECTROLYTES

2.1 Introduction

The potential application of dendrimers in an array of technologically important roles has fueled the rapid growth of research in this field. A wide synthetic variety of dendrimers have been made with the aim of utilizing these molecules as hosts in controlled-release systems and as catalytic substrates.[1–3] The nature of the intramolecular density profile and the position of the terminal groups are critical in these applications. Ideally, the branches of the dendrimer would be highly extended at each generation of growth, with branch termini lying at the periphery of the molecule, as illustrated in Figure 2.1A. Several theoretical[4–12] and experimental[13–20] studies have addressed the possibility of this occurring in flexible dendritic systems. Some experimental evidence,[16–20] however, suggests that this behavior is not realized. Consideration of the conformational entropy of the molecule provides an understanding of the observed phenomena. In order to maximize the entropy, flexible dendrimers access many conformations that are inconsistent with the "dense shell" picture.[4] This exploration of phase space results in a "dense core"[5, 7–12] average conformation, as pictured in Figure 2.1B. If, however, the extended branch conformations were made far more energetically

favorable, then the entropy would be reduced to accommodate this energy difference, and the dense shell picture would be recovered. In this chapter we present a prescription for achieving this goal by exploiting Coulombic interactions.

In polyelectrolytic dendrimers, charge-charge repulsions may be minimized by forcing the charged moieties as far apart as possible. This should result in an expansion of the dendrimer with a corresponding rearrangement of the density profile. The DOSY NMR studies of Young and co-workers[21] and the SANS work of Briber and co-workers[22] both suggest this. These studies indicate that changing the pH of dendritic solutions results in a corresponding change in observed conformational properties. We explore this polyelectrolytic behavior in this study. Our results indicate not only that the dense shell picture may be realized, but also that the intramolecular density profile may be tuned from that of the dense core to that of the dense shell model with experimentally accessible parameters such as salt concentration or solvent pH, as illustrated in Figure 2.1.

To test this hypothesis, we applied the Monte Carlo computer simulation technique to the problem. The details of the model and algorithm are presented in Section 2.2. In Section 2.3, results which support our conjecture and a brief discussion of the possible applications of these findings are presented. A summary is provided in Section 2.4.

2.2 Model and Simulation Technique

2.2.1 Model

A bead-spring, united atom model was utilized to represent the synthetic dendrimers, as shown in Figure 2.2. The springs play the role of bonds and the beads that of the molecule's mass. Each bead is of the same diameter. The coarse-grained models studied are topologically the analog of poly(propylene imine) dendrimer. Unit charge was placed at all branch junctions and terminal groups, corresponding to a fully methylated or highly charged pH-sensitive synthetic system. The charged beads are illustrated in grey in Figure 2.2.

Bonded interactions, excluded volume interactions, and charge-charge repulsions were considered in our study, as illustrated in Figure 2.2. The energetics of the model dendrimers were described by the following potential:

$$\frac{\mathcal{U}}{k_B T} = -KR^2 \sum_{i=1}^{N-1} \log\left[1 - \left(\frac{l_i - l_\circ}{R}\right)^2\right] + \frac{\sigma}{k_B T} \sum_{i,j=1}^{N} \left[\left(e^{-\alpha(r_{ij}-d)} - 1\right)^2 - 1\right] + l_B {\sum_{i,j=1}^{N_f}}' \frac{e^{-\kappa r_{ij}}}{r_{ij}} \qquad (2.1)$$

The first term, a finitely extensible nonlinear elastic (FENE) potential, maintains the elastic connectivity of the bonds. This term permits fluctuations in the statistical bond length to facilitate equilibration of the model. The FENE potential is similar to the harmonic, "spring" potential, but maintains a maximum and minimum limit on the bond length. Here, N is the total number of beads in the molecule and K is the spring constant. $R = l_{max} - l_\circ$ with $l_\circ = \frac{l_{max}+l_{min}}{2}$. l_i, l_{max}, and l_{min} are the length of bond i, the maximum, and the minimum bond lengths, respectively. The values of the parameters were chosen to scale the simulation in units

of Bjerrum length and to prevent the occurrence of phantom chains. The value of the Bjerrum length, l_B, in water at room temperature is 7.1Å.[23] In synthetic systems, the distance between branch points is estimated to be on the order of 5Å. For model systems with one spring between branch points, $l_\circ$ should correspond to this experimental value. Therefore, we set $l_\circ = \frac{5\mathring{A}}{l_B} = 0.7$ to yield one simulational unit equal to 7.1 Å. To prevent non-physical bond crossing, after Binder et al.,[24] we have taken $K = 20.0/l_B^2$, $l_{min} = 0.4l_B$ and $l_{max} = 1.0l_B$.

The second term, the Morse potential, models the excluded volume interactions between non-bonded beads. Similar to the Lennard-Jones potential, this term is characterized by a repulsive core at short distances and an attractive tail at long distances. Therefore, simulations may be performed in good, θ, and poor solvents. However, this potential is more computationally efficient because the attractive tail falls off more rapidly with distance than does the Lennard-Jones expression. Thus, a linked-cell technique was employed to truncate this term at a length of one cell box. σ and α are strength and range parameters, respectively. r_{ij} is the distance between beads i and j. d is the bead diameter. In order to ensure computational efficiency, after Binder et al.,[24] we chose $\alpha = 24.0/l_B$ such that the Morse term falls to zero for $r_{ij} \geq 1.25d$. Thus, $d = 0.8l_B$ yields a linked-cell of unit dimension. σ was set to unity and solvent quality determined by k_BT, the thermal energy. Rather than calculate the FENE and Morse potentials exactly for every new state generated in the simulation, a table of discrete energy values was created at the beginning of the simulations. The bonded interactions were thus approximated by searching the table for the energy value that most closely corresponded to the calculated bond length. A Δl_i value of $6.00 \times 10^{-4} l_B$ was used in creating the table. A value of Δr_{ij} equal to $8.75 \times 10^{-4} l_B$ was used in constructing the Morse table.

No difference in accuracy was observed between simulations employing these tables and those that used exact calculation of the potentials.

The third term, the Debye-Hückel potential, approximates the repulsive Coulombic interactions. This term allows for the parameterization of solvent ionic strength via κ, the inverse Debye screening length, which is proportional to the square root of the added salt concentration.

$$\kappa^2 = 4\pi l_B \sum_i c_i z_i^2 \tag{2.2}$$

Here, c_i and z_i are the concentration and valence of the ith ion, respectively. The potential falls off rapidly at low values of Debye length, corresponding to high salt concentrations, but is long-ranged for large values, representing low salt concentrations. Σ' indicates that the summation runs over N_f tri-functional and terminal beads. κ^{-1} was adjusted within the range of experimentally obtainable values, 3Åto 300Å, corresponding to salt concentrations of 1 molar to 0.1 millimolar. This term was calculated exactly for every pair-wise interaction in the system: no truncation was performed on the charge-charge interactions.

Since our objective was to simulate polyelectrolytic dendrimers in good solvent conditions, solvent quality was studied for non-charged analogs by analysis of the dependence of the mean-squared radius of gyration, $\langle R_g^2 \rangle$, relative to its value at θ-conditions, $\langle R_g^2 \rangle_\theta$, as a function of temperature. $\langle R_g^2 \rangle_\theta$ was determined from the Gaussian form factor via Guinier law plots. The details of these calculations are outlined in reference [25]. $k_B T$ was set to 0.7σ, well within the good solvent region for these models.

2.2.2 Algorithm

Metropolis Monte Carlo simulations employing a bond-fluctuation algorithm adopted from Milchev and Binder[24] were used to generate the statistical ensembles. Random self avoiding walks complying with the bond length constraints were generated for initial conditions. These configurations were then relaxed for $30,000$ perturbations prior to collecting statistics. The algorithm is straight-forward. A bead is chosen at random and its location perturbed by ΔX, ΔY and ΔZ in the range of ± 0.5 simulational units. The energy change, ΔU, for the transition from the prior conformation to the new conformation is then calculated. If ΔU is negative, the new conformation is accepted. If not, it is accepted or rejected according to the Metropolis criteria.[26] Specifically, a random number in the range of 0 to 1 is chosen. If the random number is less than the Boltzmann factor for the transition, $e^{-\frac{\Delta U}{k_B T}}$, then the new conformation is accepted. Otherwise, the previous conformation is restored. This process is repeated for millions of cycles and the physical properties of the molecule are calculated every $10,000$ Monte Carlo steps (MCS), each step representing N perturbations. These instantaneous values are used to generate running averages.

Three variables were examined in this study: the number of generations of growth, the number of springs and non-charged beads between branch points, and κ^{-1}. Statistics were collected for 3 to 6 million MCS. Approximately 1/3 of the perturbations were successful, leading to ensemble populations of at least 1 million configurations per simulation. Rapid equilibration of the models was observed. Doubling the number of MCS led to only a 0.7% change in $\langle R_g^2 \rangle$ for the largest model studied.

2.3 Results and Discussions

2.3.1 Scaling Analysis

Monte Carlo trajectories were constructed from $\langle R_g^2 \rangle$ to monitor the approach to equilibrium. A strong dependence of $\langle R_g^2 \rangle$ on κ and N was observed. An analysis of these results was facilitated by a simple Flory argument. The conformational free energy for polyelectrolytic dendrimers is governed by three components: an elastic connectivity term, an excluded volume term, and a Coulombic interaction term.

$$\frac{F}{k_B T} = F_{elastic} + F_{excluded} + F_{Coulombic} \tag{2.3}$$

$F_{elastic}$ should, as in the linear case, reflect the scaling behavior of dendrimers without excluded volume. Zimm and Stockmayer[27] showed that $R_g^2 \propto N^{1/2}$ for random dendritic molecules. Thus,

$$F_{elastic} \propto \frac{R_g^2}{N^{1/2}} \tag{2.4}$$

Examination of the pairwise interaction portion of the Edwards Hamiltonian yields the sought after dependence for the excluded volume and Coulombic repulsion terms. In the limit of high salt concentration, the two terms may be combined into an effective delta function potential.[28]

$$\frac{H}{k_B T} = \frac{1}{2l_0^2} \int_0^{Nl_0} ds \int_0^{Nl_0} ds' \delta \left[\vec{R}(s) - \vec{R}(s') \right] \left(w + \frac{4\pi l_B}{\kappa^2} \right) \tag{2.5}$$

Here, w is the familiar effective excluded volume interaction magnitude and is given by the binary-cluster integral:

$$w = \int d^3 r_{ij} \left[1 - e^{-\frac{u_{ij}}{k_B T}} \right] \tag{2.6}$$

u_{ij} is the pairwise non-bonded interaction, the Morse potential in this study. Numerical evaluation of eq. (2.6) yields a value of 0.11 for w in this study. This was found to be in good agreement with the value obtained by fitting data from simulated linear molecules with the well known Flory cross-over equation.[29] $\vec{R}(s)$ is the spatial location of the segments. s is the contour position variable along the chain. The delta function contributes a R_g^{-3} scaling. Thus,

$$F_{excluded} + F_{Coulombic} \propto \left(w + \frac{4\pi l_B}{\kappa^2} \right) \frac{N^2}{R_g^3}. \tag{2.7}$$

Combination of eqs (2.4) and (2.7) and minimization of F/k_BT with respect to R_g yields the following expected scaling behavior for higher salt concentrations:

$$\frac{R_g}{N^{1/4}} \propto \left[\left(w + \frac{4\pi l_B}{\kappa^2} \right) N^{5/4} \right]^{1/5}. \tag{2.8}$$

Figure 2.3 illustrates the simulations' agreement with this prediction for generations three, four, and five with 1, 2, and 4 springs between branch points. The predicted behavior is observed for much of the data. The scaling argument is most effective at reducing the data for high values of κ corresponding to the high salt concentration limit, and for 4 springs between branch points, corresponding to higher values of N where the mean-field nature of the treatment is expected to be more applicable. However, the simulations included Debye lengths spanning the range from high to low salt concentrations. This is reflected in Figure 2.3 by the deviation away from the predicted behavior at low values of κ and by the slope of approximately 1/10 as opposed to the predicted 1/5.

2.3.2 Smart Behavior Observed

Figure 2.4 exemplifies the "smart" behavior predicted for these molecules. Results from a single simulation of a fifth generation dendrimer with 2 springs between branch points in which κ^{-1} was cycled from 3Åto 300Åare presented. This figure demonstrates not only that a large percent change in $\langle R_g^2 \rangle$, 65% in this case, is effected with varying Coulombic screening, but also that the proposed corresponding conformational rearrangement is achieved: the model dendrimer redistributes its mass from a dense core picture to that reflecting a dense shell representation. This figure also demonstrates two important traits of the simulation. Since the same average value of $\langle R_g^2 \rangle$ is recovered rapidly from differing initial conformations, the results indicate the algorithm's ergodicity and speed of equilibration.

2.3.3 Density Profiles

The density profiles better illustrate the transition from a dense core to a dense shell average conformation. The average density profiles were calculated by dividing the space around the configurational center of the model dendrimers into concentric shells of thickness d. The average segment density in each shell at a distance r away from the center, $\langle \rho(r) \rangle$, is given as:

$$\langle \rho(r) \rangle = \langle n(r) \rangle \frac{V_b}{V_s(r)}. \tag{2.9}$$

$\langle n(r) \rangle$ is the ensemble average number of beads in the shell at distance r. V_b and $V_s(r)$ are the volumes of the beads and shells, respectively.

At $\kappa^{-1} = 3\text{Å}$, corresponding to high salt concentration, the density is observed to be monotonically decaying with radial distance in accordance with the dense core

picture, as predicted by Lescanec and Muthukumar.[5] However, as κ^{-1} is increased to 64Å, corresponding to low salt concentration, a minimum occurs near the core, indicating increased porosity in the interior of the molecule. This minimum is followed by a secondary peak in density near the model's periphery, approaching the dense shell picture. The depth of this minimum and the radial position of the secondary peak increases with increasing κ^{-1}. This effect is most pronounced for the higher generations and is absent in generations one and two for 1, 2, and 4 springs between branch points. Figure 2.5 is representative of the density profile behavior. Results for the fifth generation of growth with 2 springs between branch points are illustrated.

The density profiles of the terminal segments were also examined. Regardless of the value of κ^{-1}, the terminal groups are found to be dispersed throughout the molecule. However, the location of maximum terminal group density does shift towards the periphery with increasing κ^{-1}. This behavior is demonstrated in Figure 2.6 in which results for the fifth generation dendrimer with 4 springs between branch points are illustrated. κ^{-1} was cycled from 3Åto 300Å. In the high salt limit the maximum terminal group density lies below the $\langle R_g^2 \rangle^{1/2}/l_B$ value of 4.80. However, in the low salt limit the maximum falls above the $\langle R_g^2 \rangle^{1/2}/l_B$ value of 9.22. Further, the value of $\langle R_g^2 \rangle_T$ of the terminal groups is found to be higher than that for the whole molecule, regardless of the value of κ^{-1} and the corresponding terminal group distribution. For example, in simulations of sixth generation monocentric model dendrimers analogous to poly(amido amine) with an ammonia core and charged terminal groups, the ratio of $\langle R_g^2 \rangle_T / \langle R_g^2 \rangle$ shifts from 1.81 to 4.65 when κ^{-1} is varied from 3Åto 300Å.

2.3.4 Form Factors

To facilitate comparison with SANS data, the spherically averaged single particle form factor, $S(\vec{q})$, was calculated.

$$S(\vec{q}) = \frac{1}{N^2} \sum_{i=1}^{N} \sum_{j=1}^{N} \frac{\sin(\vec{q} \cdot \vec{r_{ij}})}{\vec{q} \cdot \vec{r_{ij}}} \tag{2.10}$$

where

$$|\vec{q}| = \frac{4\pi}{\lambda} \sin\left(\frac{\theta}{2}\right). \tag{2.11}$$

A secondary peak in the single particle form factor is observed to arise, and the magnitude of the peak is seen to increase with increasing κ^{-1} for generations three and above. The location of the maximum shifts to lower values of $|\vec{q}|$ with increasing κ^{-1}. This peak corresponds to the development of internal order whose length scale increases with decreasing Coulombic screening. This behavior, shown in Figure 2.7, is in qualitative agreement with experimental observations for poly(amido amine) dendrimers studied via SANS,[22] though the experiments were carried out at a higher concentration and include intermolecular correlations. Results for the fifth generation of growth with 4 springs between branch points are presented with κ^{-1} in the range of 3 to 64Å.

2.3.5 Non-Charged Limit

Figure 2.8 illustrates the model's relevance to experimentally realizable synthetic systems. SANS results for poly(propylene imine) dendrimers from the literature[30] and our simulation results in the non-charged limit are presented. Good

agreement is observed with a slight over-prediction at higher generations. This systematic deviation likely arises from the thermodynamic nature of the simulation. Specifically, the exact value of k_BT in the simulational units corresponding to the solvent quality or magnitude of the excluded volume interaction of the experimental system is difficult to ascertain. Nonetheless, this comparison does illustrate the applicability of the model and algorithm to the study of synthetic systems.

2.3.6 Discussion

These results demonstrate two technologically important properties of polyelectrolytic dendrimers. First, the position of most terminal moieties in the low electrostatic screening limit is on the surface of the molecule. This is of particular significance for the proposed catalytic and high-density crosslinking applications that would take advantage of the large number of reactive terminal groups. Second, not only may the hollow core conformation be obtained in the limit of low salt concentration or by adjusting the pH, but the density profile may also be tuned to the dense core picture by simply adjusting external experimental constraints. This behavior is requisite for the controlled release applications proposed for these molecules.[1–3] One might imagine trapping a small molecule inside a polyelectrolytic dendrimer at low salt concentration or at low pH. Then, the small molecule, a drug for example, may be delivered by placing the guest-host complex in a high salt or neutral pH medium to effect a rearrangement of the density profile. This rearrangement may be expected to eject the guest from its dendritic cage.

2.4 Conclusions

In conclusion, the dilute solution behavior of polyelectrolytic dendrimers in solvents of various ionic strengths has been examined by Monte Carlo simulations. The intramolecular density profile is observed to be heavily dependent upon the Debye screening length. Based upon these results, we predict that the density profiles of synthetic systems are tunable from that of the dense core to that of the dense shell picture by manipulation of the salt concentration or pH in aqueous solutions. Studies in the literature suggest this possibility, but we present here the first clear demonstration of the large changes in molecular dimension that are realizable. Finally, experimental realization of these predictions continues to be debated in the literature.[31–35]

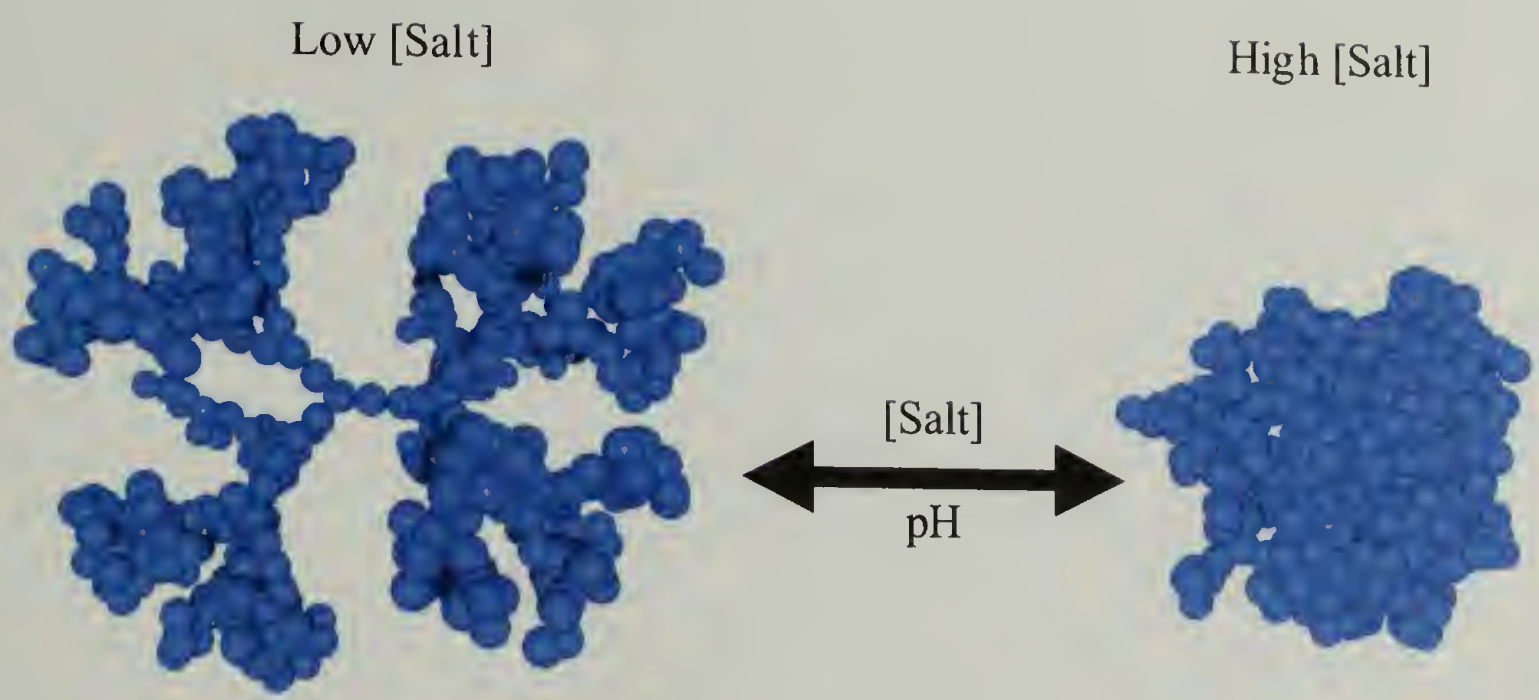

Figure 2.1: A) The hollow core, "dense shell" picture. B) The "dense core" picture. These are representative snapshots from the statistical ensembles generated in this study for the 6^{th} generation with 2 springs between branch points.

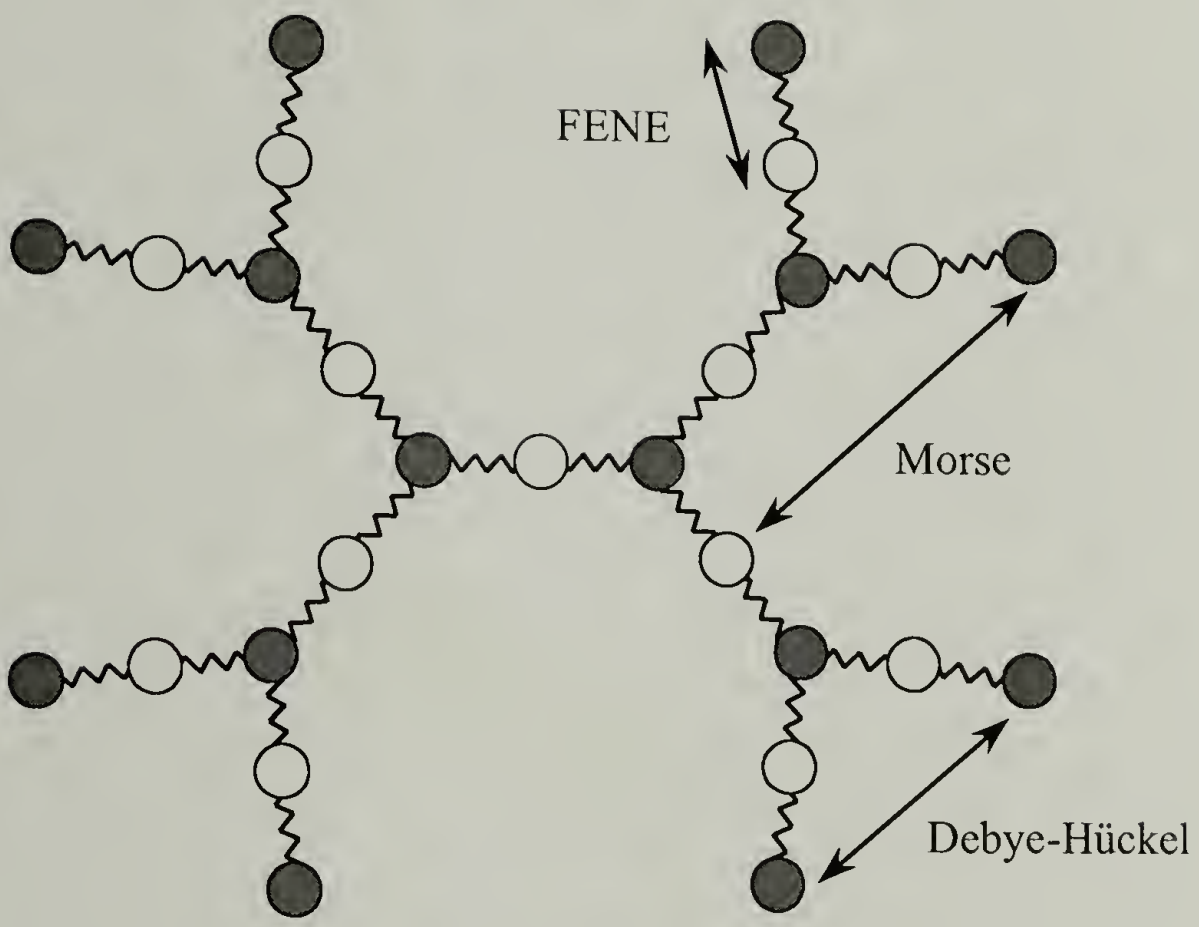

Figure 2.2: The bead-spring model employed in this study. The charged beads are colored grey.

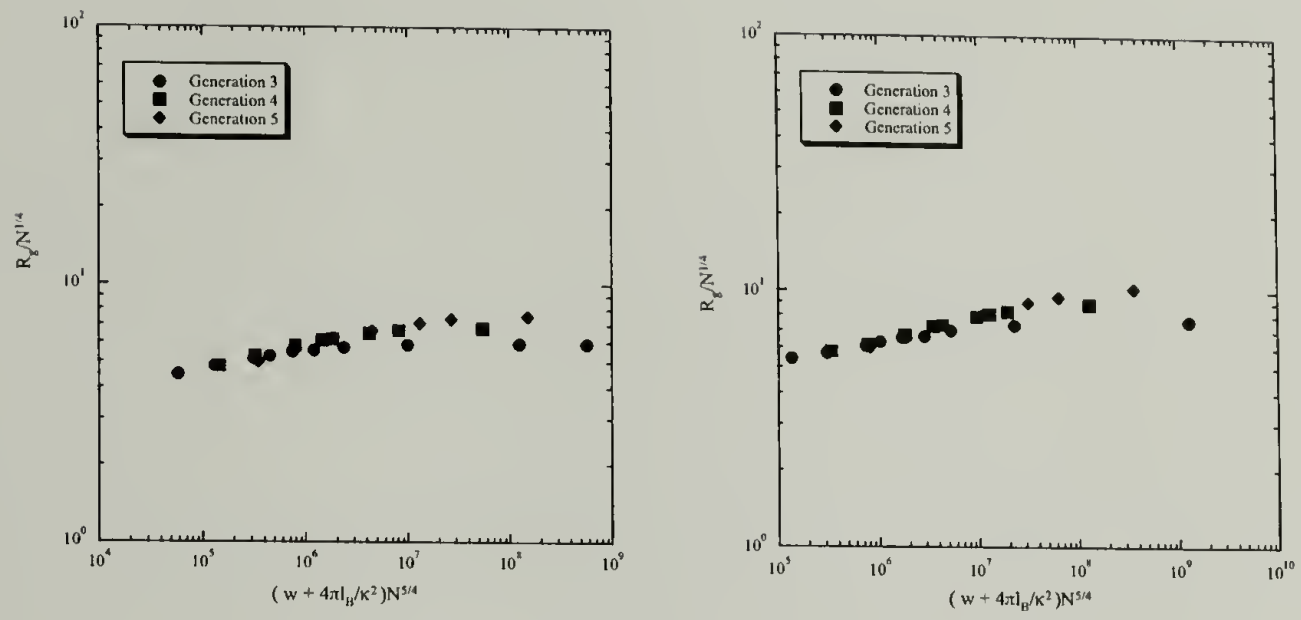

Figure 2.3: The $\langle R_g^2 \rangle^{1/2}$ as a function of N and κ for the, 3^{rd}, 4^{th}, and 5^{th} generations. Data for 1, 2, and 4 springs between branch points is presented in A), B), and C), respectively. All lengths are in units of Angstroms.

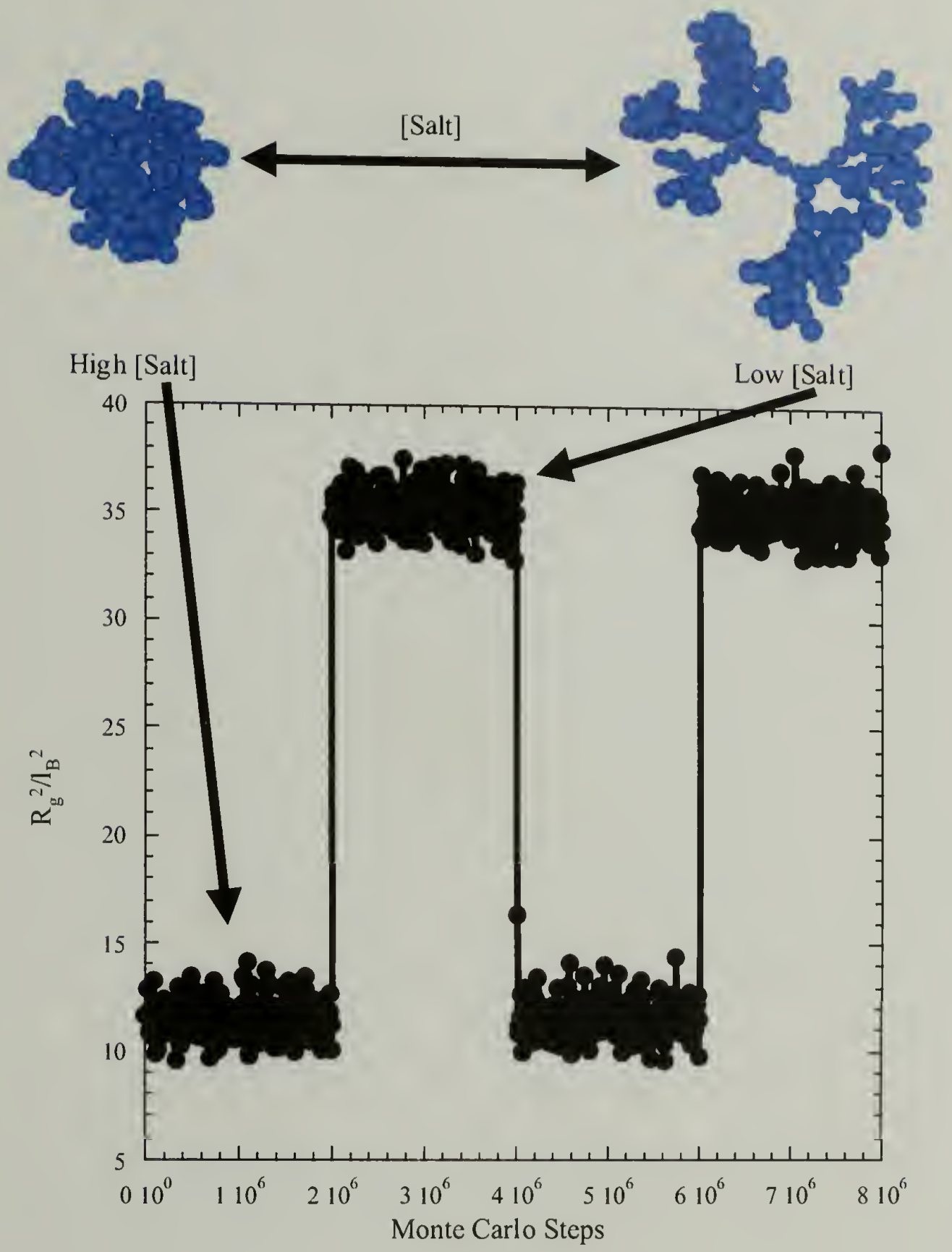

Figure 2.4: Smart behavior demonstrated in a polyelectrolytic 5^{th} generation dendrimer with 2 springs between branch points. κ^{-1} was cycled from $3\mathring{A}$ (high salt concentration) to $300\mathring{A}$ (low salt concentration).

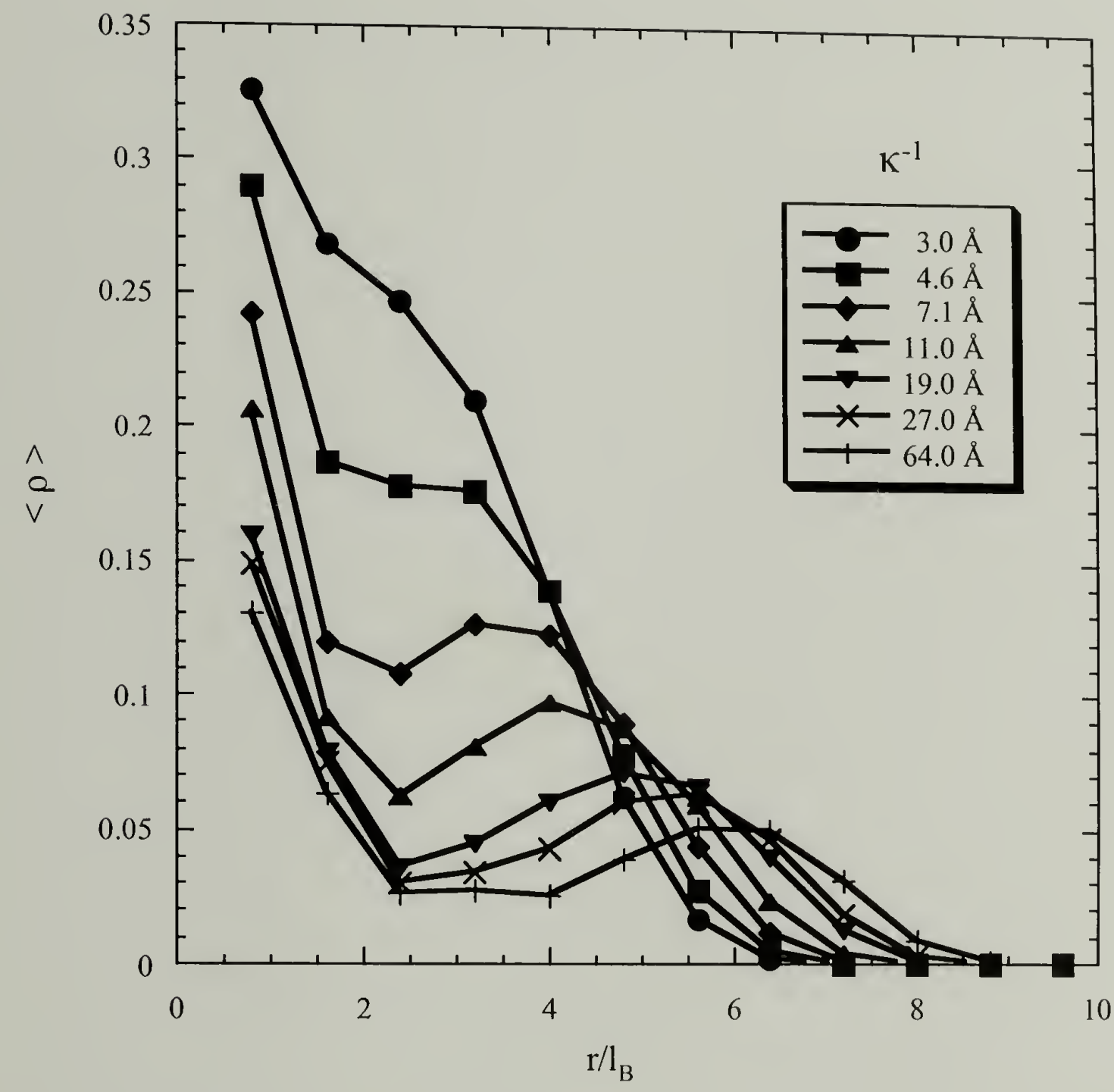

Figure 2.5: Typical density profiles. Data for a 5^{th} generation dendrimer with 2 springs between branch points are shown.

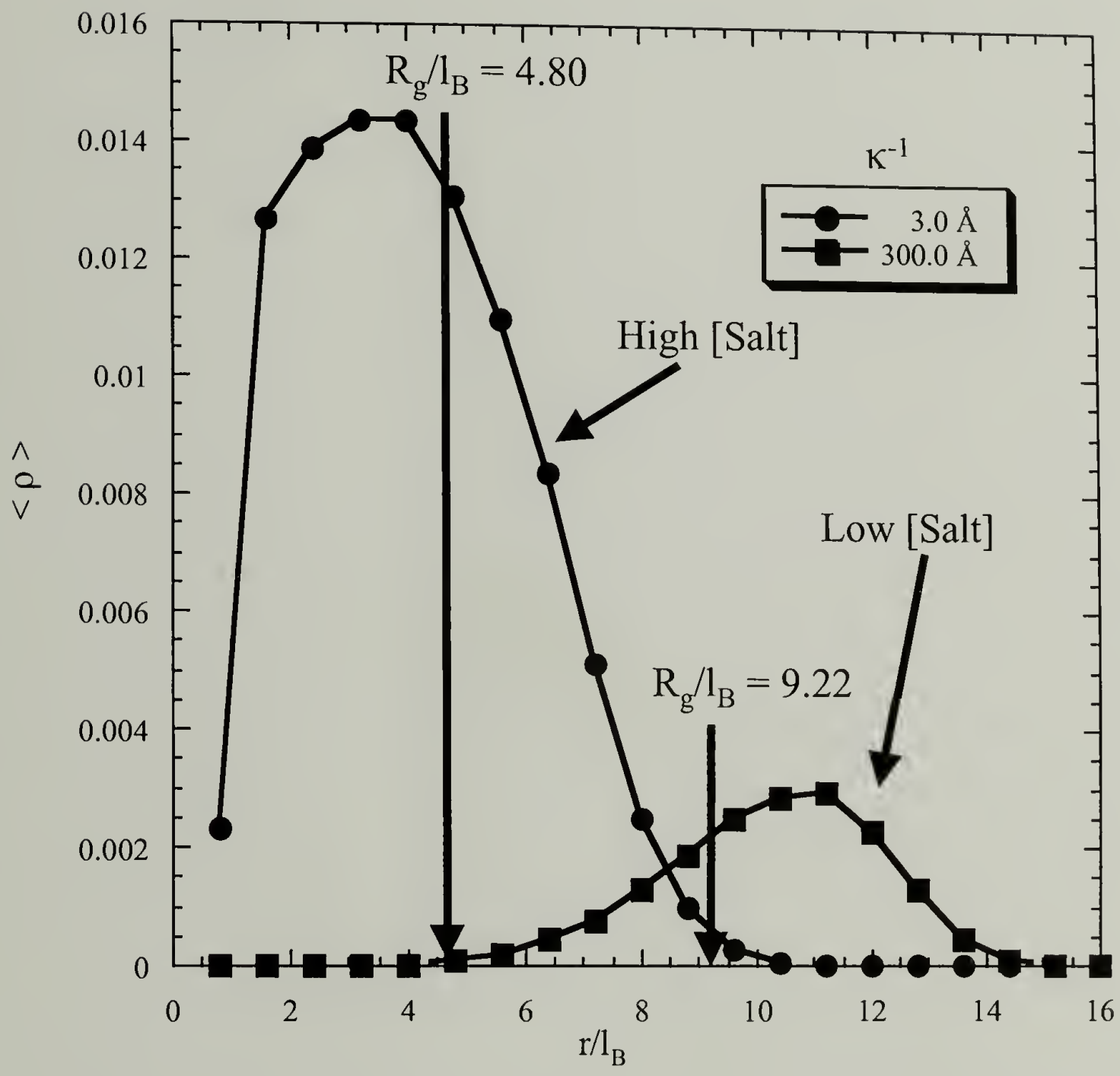

Figure 2.6: Typical density profiles for the terminal segments. Data for a 5^{th} generation dendrimer with 4 springs between branch points are shown.

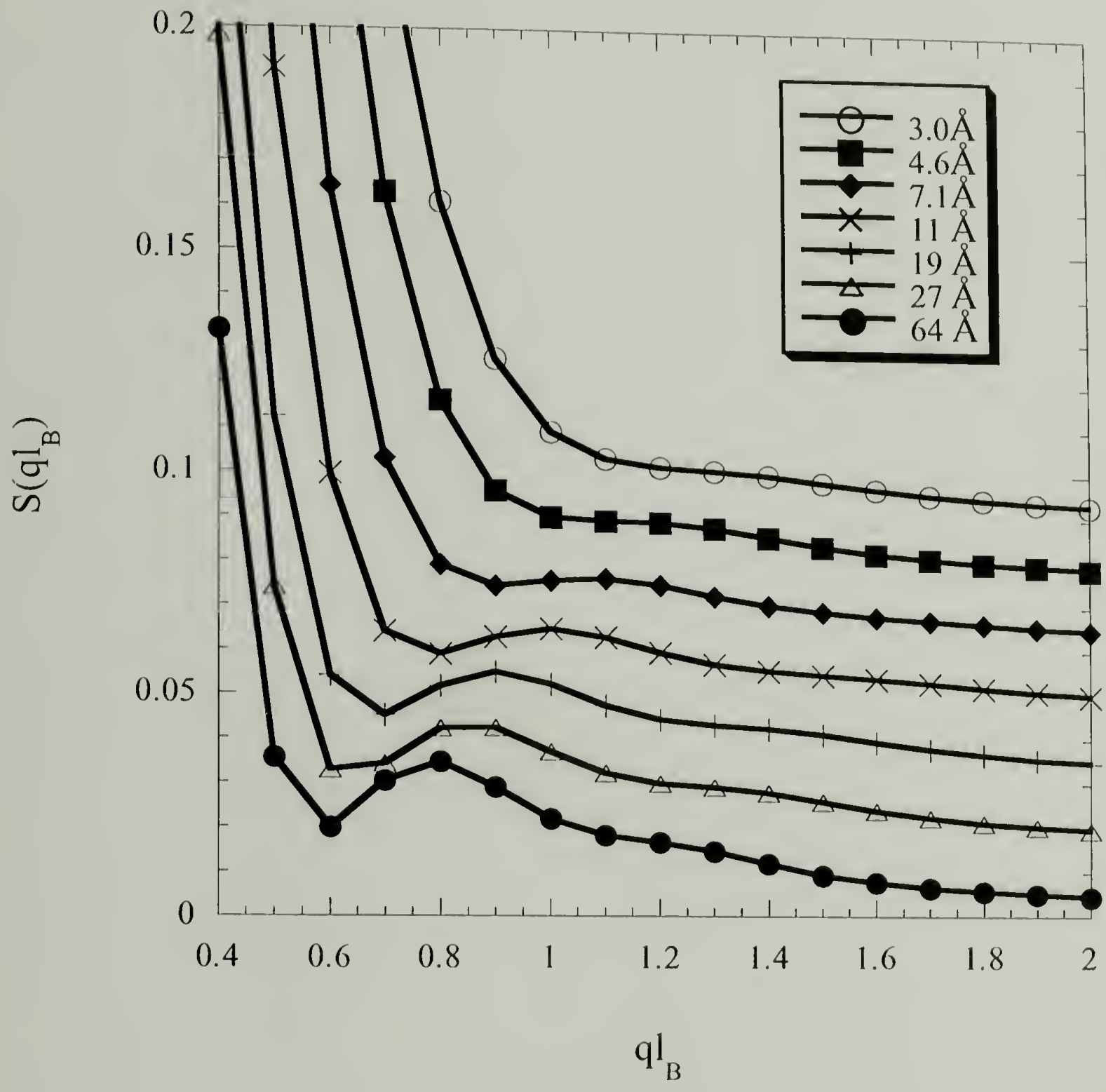

Figure 2.7: Typical structure factors for the model dendrimers. The data have been shifted along the y-axis by $\delta = n \times 0.015$ with $n = 0$ for $\kappa^{-1} = 64\mathring{A}$ and $n = 6$ for $\kappa^{-1} = 3\mathring{A}$. Data for a 5^{th} generation dendrimer with 2 springs between branch points are shown.

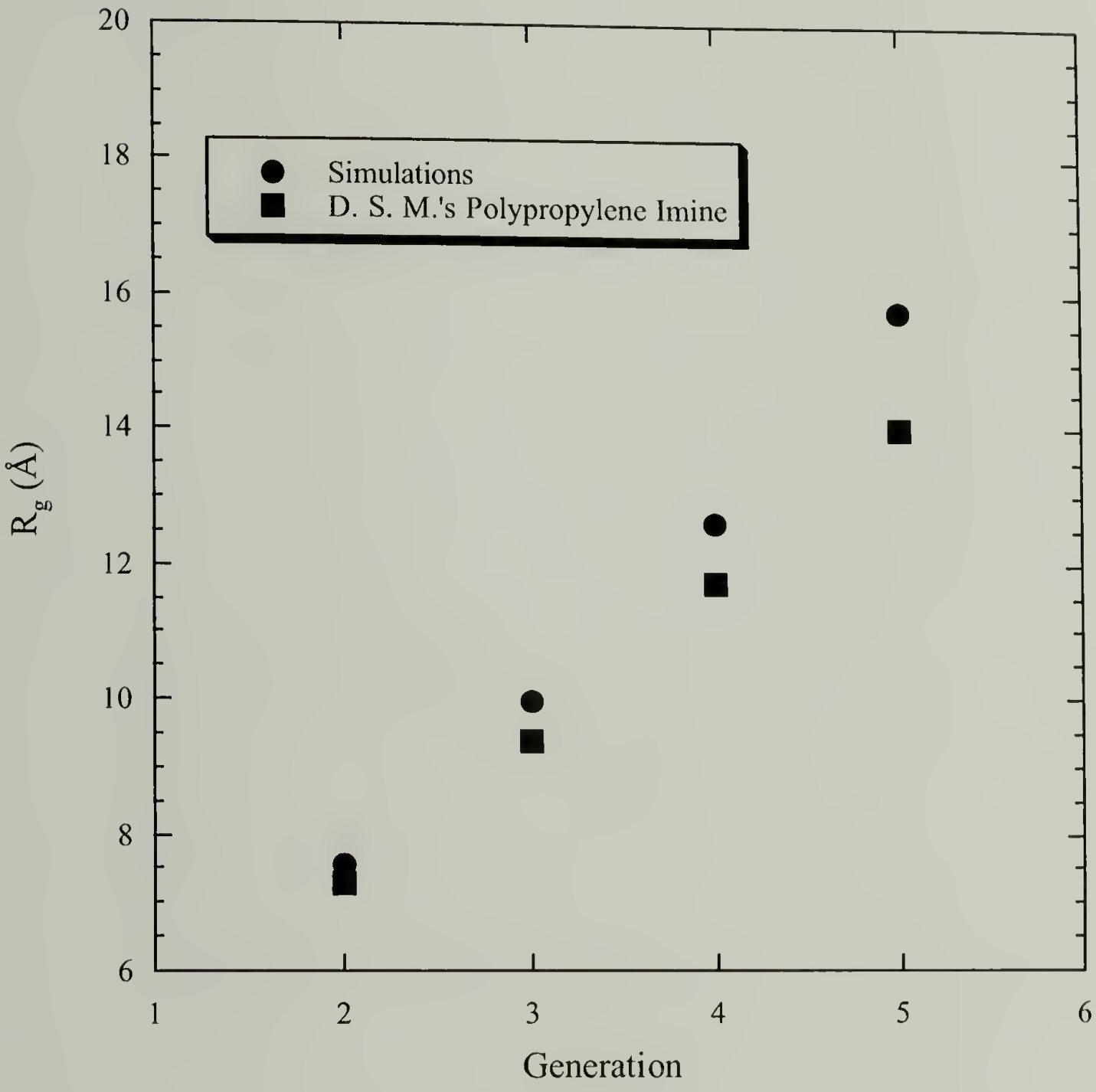

Figure 2.8: A comparison of experimental results for poly(propylene imine) dendrimers and the Monte Carlo results for their bead-spring, topological analogs in the non-charged limit.

CHAPTER 3

DENDRIMER-POLYELECTROLYTE COMPLEXATION: A MODEL GUEST-HOST SYSTEM

3.1 Introduction

There has recently been an increased interest in studying complexation between polyelectrolytes and oppositely charged entities.[28, 36–49] The dendritic polymer topology offers many unique and interesting opportunities within this context. The growing list of possible applications includes their use as molecular cages and controlled delivery agents.[50] Pioneering experimental work has been carried out to explore and develop these proposed uses for dendrimers.[2, 3, 50–56] Much of this effort has focused on the complexation of charged dendrimers to oppositely charged polyelectrolytes. Of particular note are the DNA transport studies of Kukowska-Latallo and Ottaviani and their coworkers,[52–54] the light scattering investigation of polycation - dendrimer complexation by Li et al,[55] and the potentiometric titration studies of Kabanov and company.[56] These works clearly demonstrate that charged dendrimers may be employed to capture and transport oppositely charged polyelectrolytes. Although these experimental works elegantly demonstrate the potential these molecules possess to fulfill this role, a clear understanding of the criteria to form these complexes and the attendant molecular behavior is not easily discerned. Here, we attempt to elucidate a clearer molecular-level picture via

analytical and computer simulation techniques. Specifically, we examine the equilibrium complexation behavior of a monocentric dendrimer with charged terminal groups to a flexible, oppositely charged polyelectrolyte in solutions. Our approach is to investigate the molecular nature of the complex via bond-fluctuation Monte Carlo simulations and to predict the critical complexation conditions with a variational calculation. Questions pertaining to the chain location within the complex, the permeability of the dendrimer, and the change in dimension of both species upon complexation are addressed.

In section 3.2 we present the computer simulation model and technique used to calculate the equilibrium behavior of the complexes. The results of our simulations are presented in section 3.3. In section 3.4 we present our analytical prediction for the critical complexation conditions and a comparison of that result with our simulations. The significance of our findings are discussed in light of the above mentioned experimental work in section 3.5 and we make some concluding remarks in section 3.6.

3.2 Simulation Model and Algorithm

3.2.1 Model

A bead-spring, united atom model was employed to represent both the monocentric dendrimer with charged terminal groups and the fully-charged chain-electrolyte. The springs serve to maintain the topological connectivity in the molecules and have the same average length in both. The beads represent the mass and are the sites of the pair-wise interactions. All beads are of the same diameter, d. Three

generations of dendritic growth, 4, 5, and 6, and three chain molecular weights, 15, 30, and 60, were examined. The terminal groups of the dendrimer and every bead on the chain have charge qe, where e is the fundamental unit of charge. The charge-charge interaction between the two molecules is attractive, corresponding to the interaction of a polyanion with a polycation. Charged beads are illustrated in black and gray in Figure 3.1. This model is analogous to the experimentally realizable system of an ammonia core based dendritic poly(amido amine)[57] or dendritic poly(propylene imine)[58] with charged terminal groups complexing to a flexible polyelectrolyte such as poly(acrylic acid).

This simulation incorporated three classes of interactions: bonded, excluded volume, and Coulombic. The "finitely extensible nonlinear elastic" (FENE)[59] potential was employed to maintain the bond constraints and is given by eq. (3.1).

$$\frac{\mathcal{U}_{\mathcal{B}}}{k_B T} = -KR^2 \left(\sum_{i=1}^{N_L - 1} \log \left[1 - \left(\frac{l_i - l_\circ}{R} \right)^2 \right] + \sum_{i=1}^{N_D - 1} \log \left[1 - \left(\frac{l_i - l_\circ}{R} \right)^2 \right] \right) \quad (3.1)$$

Here, N_D and N_L are the number of dendritic and linear beads, respectively. K is the spring constant and is set to $20.0/l_B^2$. $R = l_{max} - l_\circ$ where $l_\circ = \frac{l_{max}+l_{min}}{2}$. l_i, l_{max}, and l_{min} are the bond length of bond i, the maximum, and the minimum bond lengths, respectively. The values of these parameters were chosen to scale the simulation lengths by the Bjerrum length, l_B (defined below), and to prevent the occurrence of "phantom chains." As in Chapter 2, we have taken $l_\circ = 0.7 l_B$, $l_{max} = 1.0 l_B$, and $l_{min} = 0.4 l_B$ for both the dendrimer and the linear chain. Also as in Chapter 2, the FENE potential was approximated by a table of discrete values.

The electrostatic attractions and repulsions were approximated by the Debye-Hückel potential,[60] eq. (3.2) below.

$$\frac{\mathcal{U}_C}{k_B T} = l_B|q|^2 \sum_{i,j=1}^{N_T}{}' \frac{e^{-\kappa r_{ij}}}{r_{ij}} + l_B|q|^2 \sum_{i,j=1}^{N_L} \frac{e^{-\kappa r_{ij}}}{r_{ij}} - l_B|q|^2 \sum_{i=1}^{N_T}{}' \sum_{j=1}^{N_L} \frac{e^{-\kappa r_{ij}}}{r_{ij}}. \tag{3.2}$$

The primes indicate summation over only the terminal groups of the dendrimer. N_T is the number of dendritic terminal groups and r_{ij} is the distance between two charged beads. The inverse Debye length, κ, is a measure of the solution ionic strength and is given by:

$$\kappa^2 = 4\pi l_B \sum_i c_i z_i^2. \tag{3.3}$$

$$l_B = \frac{e^2}{4\pi\epsilon_\circ \epsilon k_B T}. \tag{3.4}$$

Here, c_i and z_i are the concentration and valence of the ith ion, respectively. $\epsilon_\circ$ is the permittivity of vacuum and ϵ is the dielectric constant. κ^{-1} was varied from $0.42 l_B$ to $42.0 l_B$, spanning the range of aqueous salt concentrations from 1 molar to 0.1 millimolar at 25°C. In the limit of high solvent ionic strength the potential falls off rapidly but is long ranged in the low salt concentration limit. We have studied different values of $|q| = 1.0, 0.5$, and 0.1. In realistic situations, smaller counter ions may play a substantial role and at present the correct form of the potential between two charges on two macromolecules in an electrolyte solution is not known. To facilitate an understanding of the large scale behavior of complexation between macromolecules, however, we have assumed the Debye-Hückel potential between two charges.

Finally, the excluded volume interactions between all the beads in the system were modeled by eq. (3.5), the Morse[60] potential.

$$\frac{\mathcal{U}_{\mathcal{E}}}{k_BT} = \frac{\sigma'}{k_BT}\sum_{i=1}^{N_L}\sum_{j=1}^{N_D}\left[\left(e^{-\alpha'(r_{ij}-d)}-1\right)^2-1\right]$$
$$+\frac{\sigma}{k_BT}\left(\sum_{i,j=1}^{N_L}\left[\left(e^{-\alpha(r_{ij}-d)}-1\right)^2-1\right]+\sum_{i,j=1}^{N_D}\left[\left(e^{-\alpha(r_{ij}-d)}-1\right)^2-1\right]\right) \quad (3.5)$$

σ and α^{-1} are, respectively, the strength and range parameters employed for the intramolecular potentials. In this study, $\alpha^{-1} = l_B/24$ and $d = 0.8l_B$ in order to prevent bond-crossing and to provide a short truncation length of $3.5l_B$ for the interaction.[24] σ was chosen as our fundamental unit of energy and solvent quality was determined by k_BT. The simulation was carried out in a "good" solvent regime for both molecules with $k_BT = 0.7\sigma$.[24, 25] Different values for the strength and range parameters were used for the intermolecular interactions. To mimic a purely hard-bead interaction, α'^{-1} and σ' were assigned the values of $l_B/80.0$ and 0.01σ, respectively. As in Chapter 2, a discrete table of energy values was generated at the beginning of the simulations and used to approximate the Morse energy values.

3.2.2 Algorithm

A generalization to multiple molecules of the algorithm presented in Chapter 2 was employed in this study. Bond-fluctuation was accomplished by randomly displacing beads by ΔX, ΔY, and ΔZ in the range $\pm 0.5l_B$ and constraining the bond lengths to lie within the above stated bounds. The transition to each new state, corresponding to a new link in the Markovian chain, was accepted with the Metropolis criteria.[26] Specifically, a new conformation was generated and the change in energy, $\Delta\mathcal{U} = \Delta\mathcal{U}_{\mathcal{B}} + \Delta\mathcal{U}_{\mathcal{C}} + \Delta\mathcal{U}_{\mathcal{E}}$, computed. If the system decreased in energy, the new state was accepted. Otherwise a random number between 0 and 1

was obtained and the new state was accepted if the random number was less than the Boltzmann factor for the transition, $e^{\frac{-\Delta \mathcal{U}}{k_B T}}$.

The simulations were carried out in two stages. First, the chain and dendrimer were equilibrated in isolation at a given ionic strength. A linear rod was used as an initial configuration for the chains. Depending upon molecular weight, statistics for the chains were accumulated over 5 to 10 million Monte Carlo steps (MCS), each step comprising a number of attempted perturbations equal to the chain length. Samples from the ensemble were taken at a frequency of 1 every 10,000 to 40,000 MCS, varying with chain length. Similarly, an initially random, self-avoiding dendrimer was simulated for 5 to 10 million MCS and statistics were gathered once every 10,000 MCS. The sample frequencies were determined using standard statistical techniques[61] and were chosen to ensure that statistically independent values were averaged. In both cases, the ensemble average radius of gyration for each molecule was calculated to monitor the approach to equilibrium.

Next, samples from the equilibrium ensembles generated in the single molecule simulations were placed in close proximity to one another, usually $7l_B$-$3l_B$ apart. The bond-fluctuation algorithm then continued for 5 million more MCS and the population was sampled every 10,000 MCS after an initial 1 million MCS had elapsed for complexation and equilibration. Slow relaxation processes may be expected to be operational in this system. However, in order to verify that complexation did or did not occur for values of κ near the critical value, samples from complexes equilibrated under lower ionic strengths were used as initial conditions. The critical value of κ demonstrated no dependence on the initial condition used, and the ensemble averages obtained proved independent of both initial conditions and Monte Carlo trajectory (differing random number seed). Thus, though the

statistics may not be rigorously uncorrelated, we do expect that they are representative of equilibrium complexes.

The instantaneous adsorption energy defined as the total interaction between the dendrimer and the chain, $E_a = \mathcal{U}_\mathcal{E} + \mathcal{U}_\mathcal{C}$, was calculated to monitor the approach to equilibrium. Ensemble averages of several conformational characteristics were obtained post-simulation. The mean-square radii of gyration for the chain, $\langle R_g^2 \rangle_L$, and the dendrimer, $\langle R_g^2 \rangle_D$, in the complex were calculated. Further, to facilitate a clear picture of the chain's location relative to the dendrimer, the dendrimer-centered chain density profile, $\langle \rho \rangle_L$, and dendrimer terminal group density profile, $\langle \rho \rangle_T$, were calculated post-simulation using eq. (3.6) below.

$$\langle \rho(r) \rangle = \langle n(r) \rangle \frac{V_b}{V_s(r)}. \tag{3.6}$$

$\langle n(r) \rangle$ is the ensemble average number of beads in the shell at distance r. V_b and $V_s(r)$ are the volumes of the beads and shells, respectively.

3.3 Simulation Results

3.3.1 Dendrimer Density Profile

As described below, the role of the chain in the guest-host system depends upon several variables. However, the basic requirement for the encapsulation of a molecule by the dendrimer is the presence of dendritic cavities. In Chapter 2 we proposed the conditions under which flexible dicentric dendrimers with charges at each branch and terminal group might form such cavities. In this study, we also find that the density profile of monocentric dendrimers with charges at only the

terminal groups may be similarly tuned with ionic strength of the solution. For generations 4 and 5, $\langle\rho\rangle_D$ is found to be monotonically decreasing[5] in the high salt limit and a pronounced depression [4] is observed near the center of the dendrimer in the low salt limit for generation 5. Generation 6 presents similar behavior in the low salt limit, but also expresses a dip in density one bead diameter away from the center in the high salt limit due to the strong correlation of the location of the first three branch points as noted in other theoretical studies.[7, 8] This behavior is illustrated in Figure 3.2.

The radial distribution of charged terminal groups is critical in determining the complexation conditions, as suggested by our variational result discussed below. For all generations of growth, the location of the terminal groups was found to be distributed throughout the molecule in the high salt limit and pushed to the periphery in the low salt regime. This is illustrated in Figure 3.3. Note that the depletion of terminal groups near the center for all solvent conditions yields a consistently higher value for $\langle R_g^2\rangle_T$, the squared radius of gyration for the terminal groups, than that for the total molecule. This is illustrated for generation 6 in Figure 3.4.

3.3.2 Complexation-Induced Collapse

In all cases both the dendrimer and the chain shrank in their radial dimension upon complexation. This change in size is illustrated in Figures 3.5-3.7. Figure 3.5 presents $\langle R_g^2\rangle_L^{1/2}$ for a 30 bead chain. Note that as κ increases, the size of the complexed chain approaches that of the chain in free solution. Similar behavior was observed for 15 bead chains. 60 bead chains present a more complicated picture, as illustrated in Figure 3.6. For complexes formed with generation 5 and 6 dendrimer, the above noted behavior was recovered. However, generation 4 appears to interact

with the 60 bead chain in a markedly different fashion than the larger dendrimers yielding a much smaller change in chain size. Note that the apparent dip in $\langle R_g^2 \rangle_L^{1/2}$ for the generation 4 complex at $\kappa l_B \approx 0.6$ is within the standard deviation of $\pm 0.5 l_B$. The dendrimers displayed much more uniform behavior. In all cases the dendrimer shrank upon complexation and approached the free solution limit with increasing ionic shielding, as illustrated in Figure 3.7.

3.3.3 Guest-Host Behavior

Three types of complexes were observed to form depending upon the solution ionic strength and relative sizes and charge densities of the molecules. Varying these parameters led to a continuous transition from one type of complex to another. Nevertheless, this qualitative classification scheme presented below is useful for understanding the variety of behaviors that may be realized in these systems.

(i) For large dendrimers and short chains, the dendrimer encapsulates the chain and the chain collapses to a coil wrapped within the dendrimer. This is clearly demonstrated when the distribution of terminal groups is compared to the density of chain segments about the center of the dendrimer. Figures 3.8 and 3.9 illustrate this for a generation 6 dendrimer complexed to a 15 bead chain with $\kappa^{-1} = 42.0 l_B$ and $|q| = 1.0$. For visual contrast, all chains are rendered as worms and only the terminal groups of the dendrimer are drawn as beads. Here, the chain is seen to fall completely within the radial location of the maximum terminal group density. This behavior is representative of complexes between small chain electrolytes and large dendrimers.

(ii) The second type of complex is one in which the chain not only penetrates, but also has significant density outside of the dendrimer. This is illustrated in

Figures 3.10 and 3.11 for a generation 5 dendrimer complexed to a 60 bead chain with $\kappa^{-1} = 1.0 l_B$ and $|q| = 1.0$.

(iii) In the limit of the smallest dendrimer and largest chain studied, closest to a true polymer-dendrimer system, a unique complex is formed in which the dendrimer does not possess sufficient charge to shield the chain's self-repulsion to the extent that the chain will shrink. In this case, the chain is only perturbed from its stretched behavior in the immediate vicinity of the dendrimer. This is illustrated by Figures 3.12 and 3.13 in which a generation 4 dendrimer has complexed to a 60 bead chain at the solution ionic strength, $\kappa^{-1} = 8.96 l_B$ and $|q| = 1.0$. Note that near the dendrimer the chain has coiled, but that the rest of the chain remains extended. In addition to the "ball-and-chain" configuration shown here, the complex demonstrates interesting and novel dynamics: the dendrimer is observed to "walk" along the chain. Due to the fluctuations in both chain and dendrimer conformations the dendrimer illustrated in Figure 3.14 is observed to migrate from one chain end at $3.89X10^6$MCS to the other chain end at $4.89X10^6$MCS. The dendrimer's migration is not deterministic, beginning at one end and moving towards the other before reversing direction, but the dendrimer is observed to complete several laps in the course of the simulation. This type of complex was observed for all values of κ^{-1} above the critical value for 60 bead chains and generation 4 dendrimer. Though similar behavior has been observed for polyelectrolyte-sphere complexes,[48] Monte Carlo does not capture actual dynamics and this chain walking phenomenon may prove to be only a transient.

The above described complexes are qualitatively different from complexes[47] formed by two oppositely charged polyelectrolytes.

3.4 Critical Complexation Conditions

3.4.1 Theoretical Prediction

Complexation was observed to occur for a broad range of solution ionic strengths for all combinations of dendrimer and chain molecular weights studied. However, to identify the conditions necessary for complexation, we resort to a theoretical technique. Much analytical effort has been applied to the study of adsorption of a polyelectrolyte molecule to various surfaces.[28, 36–46] Particularly germane to the current investigation is the earlier work by von Goeler and Muthukumar[39], where a polyelectrolyte interacting via the Debye-Hückel potential with a single, impenetrable sphere of opposite charge was considered. Working within the ground state-dominance approximation and using the variational technique, they derived the critical conditions necessary for complexation to occur in terms of various molecular and solvent parameters. A straightforward extension of this analytical approach yields insight into the question addressed in this chapter. Below, we only present our model and result. A brief outline of the derivation is presented in Appendix A. However, we refer the reader to ref [39] for further details of the technique.

The conditions for complexation between the dendrimer and polymer may be expected to be dictated by the nature of the system prior to contact between the two species.[39, 49] The dendrimer may therefore be viewed as acting only as an electrostatic potential source and physical barrier. The dendritic charge distribution due to the location of the charged terminal groups is of primary concern. Our studies of polyelectrolytic dendrimers show that there is an ionic strength dependent, broad distribution of terminal groups instead of the delta function distribution considered in von Goeler and Muthukumar's earlier work. Thus, whereas von Goeler and Muthukumar considered a single charged shell, we model the dendrimer as a

continuous series of concentric shells. Further, when we consider the shell lying at the radial distance Z away from the dendrimer's center, shells lying outside Z are assumed to be permeable to the polyelectrolyte chain. The impenetrable shell at Z accounts for the excluded volume interaction. The charge-charge interaction between each shell and polymer segment is described by the spherically averaged Debye-Hückel interaction. This model is illustrated in Figure 3.15. Here, we have assumed that the terminal groups can fall between the radial distances A and B away from the center of dendrimer.

The total charge-interaction between one polymer segment and the dendrimer is the sum of the segment's attractions to each shell. This potential is given by eq. (3.7) below.

$$V = \frac{-4\pi l_B |q| e^{-\kappa r}}{\kappa r b} \frac{\Delta i}{\Delta a} \int_A^B da |\sigma(a)| a \, Sinh(\kappa a) \tag{3.7}$$

$\frac{\Delta i}{\Delta a}$ is the radial density of shells (1/length), l_B is the Bjerrum length, qe is the charge per segment, b is the bare polymer step length, r is the distance from the polymer segment to the center of the dendrimer, and $\sigma(a)$ (1/length^2) is the surface charge density due to the terminal groups on the shell situated at distance a away from the dendrimer's center.

Working within this picture and following the same essential steps as von Goeler and Muthukumar, we deduce the following as the criterion for complexation:

$$\left[1 - e^{-2\kappa Z}\right] \frac{l_B |q| \sigma_e}{b b_e \kappa^3} > \frac{0.12}{\pi}. \tag{3.8}$$

b_e is the effective step length of the chain due to intramolecular interactions and is defined in terms of the radius of gyration, R_g, and chain length, L, by:

$$R_g^2 = \frac{b_e L}{6}. \tag{3.9}$$

The result is similar to the solution for the chain-sphere case except that the distribution of terminal groups contributes an effective sphere of radius Z and surface charge density, σ_e, defined as:

$$\sigma_e = \frac{1}{Sinh(\kappa Z) Z} \frac{\Delta i}{\Delta a} \int_A^B da |\sigma(a)| a \, Sinh(\kappa a). \tag{3.10}$$

One requires values for A, B, $\sigma(a)$, $\frac{\Delta i}{\Delta a}$, and Z to utilize this prediction. Experimentally obtained knowledge of the terminal group distribution from scattering techniques will yield the former three. The latter two may be obtained via the conservation of charge constraint indicated by eq. (3.11) below.

$$N_T = 4\pi Z^2 \frac{\sigma_e}{|q|} = \frac{4\pi}{|q|} \frac{\Delta i}{\Delta a} \int_A^B da |\sigma(a)| a^2 \tag{3.11}$$

3.4.2 Comparison with Simulation

We compared our simulation results to our analytical prediction by first approximating $\sigma(a)$ based upon the isolated dendrimer's terminal group distribution using eq. (3.12) below.

$$\langle \sigma(a) \rangle = \frac{\langle n(r) \rangle}{A_s(r)}. \tag{3.12}$$

$\langle n(r) \rangle$ is the ensemble average number of beads between the shells at distances r and $r + dr$. $A_s(r)$ is the surface area of the shell falling at r. dr was set to $0.2 l_B$.

We then fit a sixth order polynomial to $\sigma(a)$. σ_e, Z, and $\frac{\Delta i}{\Delta a}$ were obtained via numerical integration using the mathematical software Mathematica version 3.0. A and B are also known from the isolated dendrimer simulations. The simulations of the isolated chains provided values for b_e via eq. (3.9). b was taken to be l_o. The remaining required values are simply input parameters from the simulation reflecting ionic strength and charge per bead. The prediction was found to be in excellent agreement with the simulations, as illustrated in Figure 3.16. Data for $N = 60$ chains, all generations of dendrimer, κ^{-1} in the range of $42.0l_B - 0.80l_B$ and $|q| = 1.0 - 0.1$ is shown.

The vertical axis captures all the chain's variables while the horizontal axis represents those of the dendrimer. The line is the theoretical boundary for complexation. All points to the left of the line should not be complexed, all points to the right should be. A system was classified as non-complexed if at any point in the simulation after the total interaction energy, $|E_a/k_BT|$, became nonzero, $|E_a/k_BT|$ fell below 10^{-6}. Typical values of $|E_a/k_BT|$ for systems with κ^{-1} just above the critical value was on the order of 10^{-2}. The difference in κ^{-1} between the two closest complexed and non-complexed points in Figure 3.16 is only $1.0l_B$.

3.5 Discussion

These results address the nature of polyelectrolyte-dendrimer complexation and criteria for its occurrence, essential to our understanding and use of these materials as guest-host systems. The variational calculation suggests (i) that there is a critical effective dendritic charge density, (ii) that increasing the chain's stiffness reduces its interaction with the dendrimer, and (iii) that there is a critical ionic strength

above which no complexation will occur. The former two predictions have been observed in the experimental studies found in the literature.[52–56] The latter is confirmed by our simulations. The simulations also indicate that complexes formed at lower salt concentrations may be disrupted by increasing the ionic strength to above the critical value. Difficulty in accomplishing this release experimentally has been noted by Kukowska-Latallo and coworkers.[52, 53] However, strong non-charged secondary interactions such as hydrogen bonding may play an important role in maintaining the complex once formed and thus hinder a salt or pH triggered release.

The molecular weight and charge density not only play a decisive role in complex formation, but also are important in determining the type of complex formed. If the chain is small and the dendrimer is large, the chain is encapsulated by the dendrimer. This encapsulation, in combination with the reversibility of complexation, is especially significant in the context of controlled delivery and also indicates that dendrimers should not be viewed as hard spheres. Conversely, if a smaller dendrimer and a larger chain are complexed, a significant chain density will lie outside of the dendrimer. The observation that the chain can penetrate a dendrimer is consistent with experimental studies.[56] Further, though highly soluble in a variety of solvents, dendrimers are occasionally observed to form aggregates[22, 62]. The presence of chains loosely attached to the surface of the dendrimer may prove useful in such applications as steric stabilization of semi-dilute solutions of catalytic dendrimers. This stabilization is also suggested in the literature.[52, 53] Finally, in the limit of large chains and small dendrimers, most closely reflecting a dendrimer-polymer system, novel "chain-walking" dynamics are observed. The mechanism of this behavior may be expected to play an important role in transporting polyelectrolytes and should studied further.

The simulations also indicate that the dimensions of both the dendrimer and chain change upon complexation. However, the extent to which the molecules shrink from their free solution sizes depends upon how close the ionic strength is to its critical value. Further, in the limit of a large polyelectrolyte and small dendrimer, the chain collapses only in the vicinity of the dendrimer, yielding a smaller change in dimension.

3.6 Conclusions

We have examined the dilute solution nature of complexes of dendrimers with charged terminal groups and oppositely charged polyelectrolytes via Monte Carlo simulation and variational theory. Critical values of salt concentration, dendrimer charge density, and chain stiffness were noted. Three types of reversible complexes were observed. Under the proper conditions, a dendrimer may encapsulate a chain, a chain may interpenetrate a dendrimer, or a unique "chain-walking" phenomenon may be observed. Though both chain and dendrimer undergo a shrinkage in size upon complexation, the extent of the rearrangement depends upon the proximity of the system to the complexation threshold and the relative shielding ability of the two molecules.

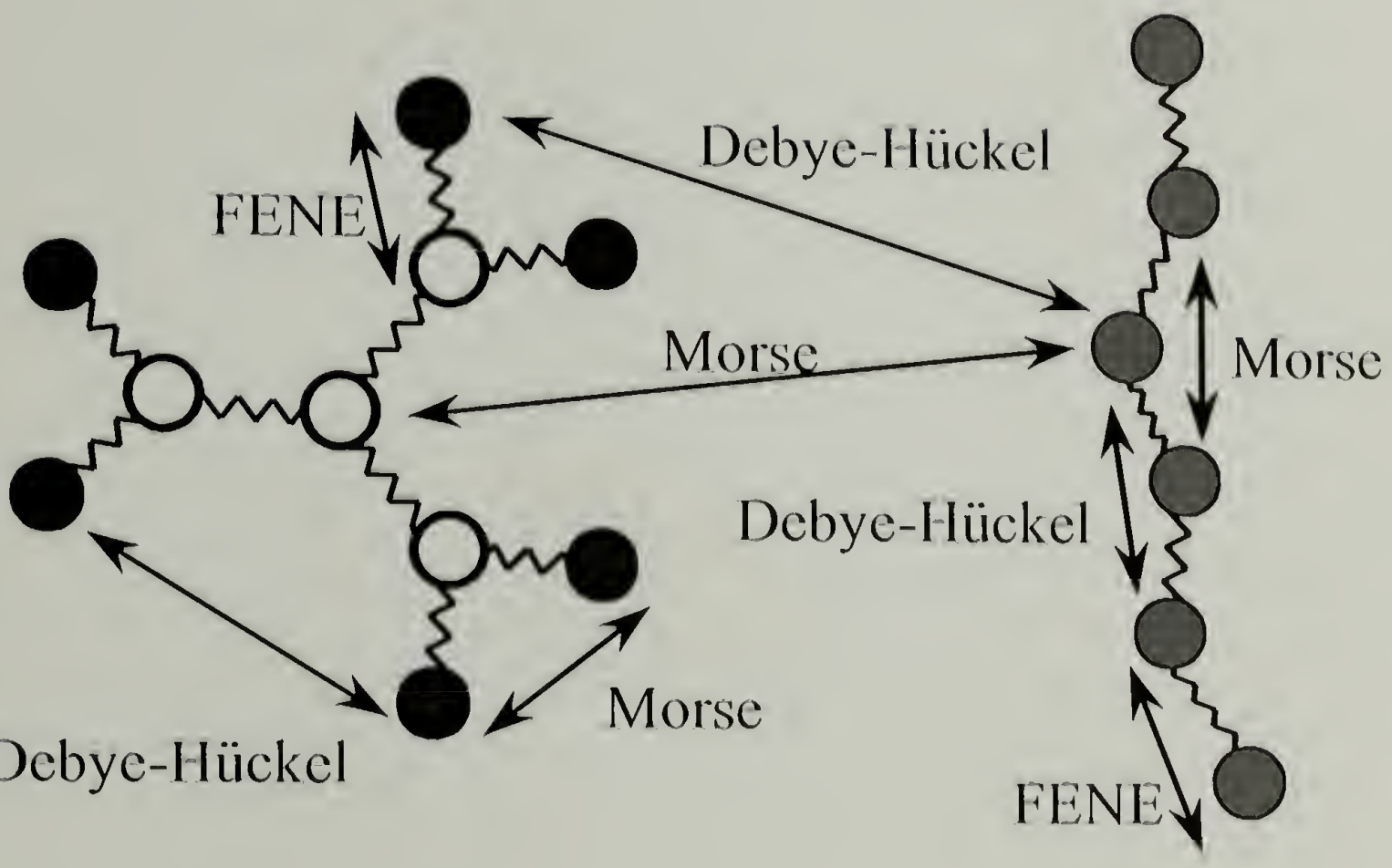

Figure 3.1: Bead-spring model used in simulations. The chain and dendrimer have oppositely charged beads, shaded in gray and black.

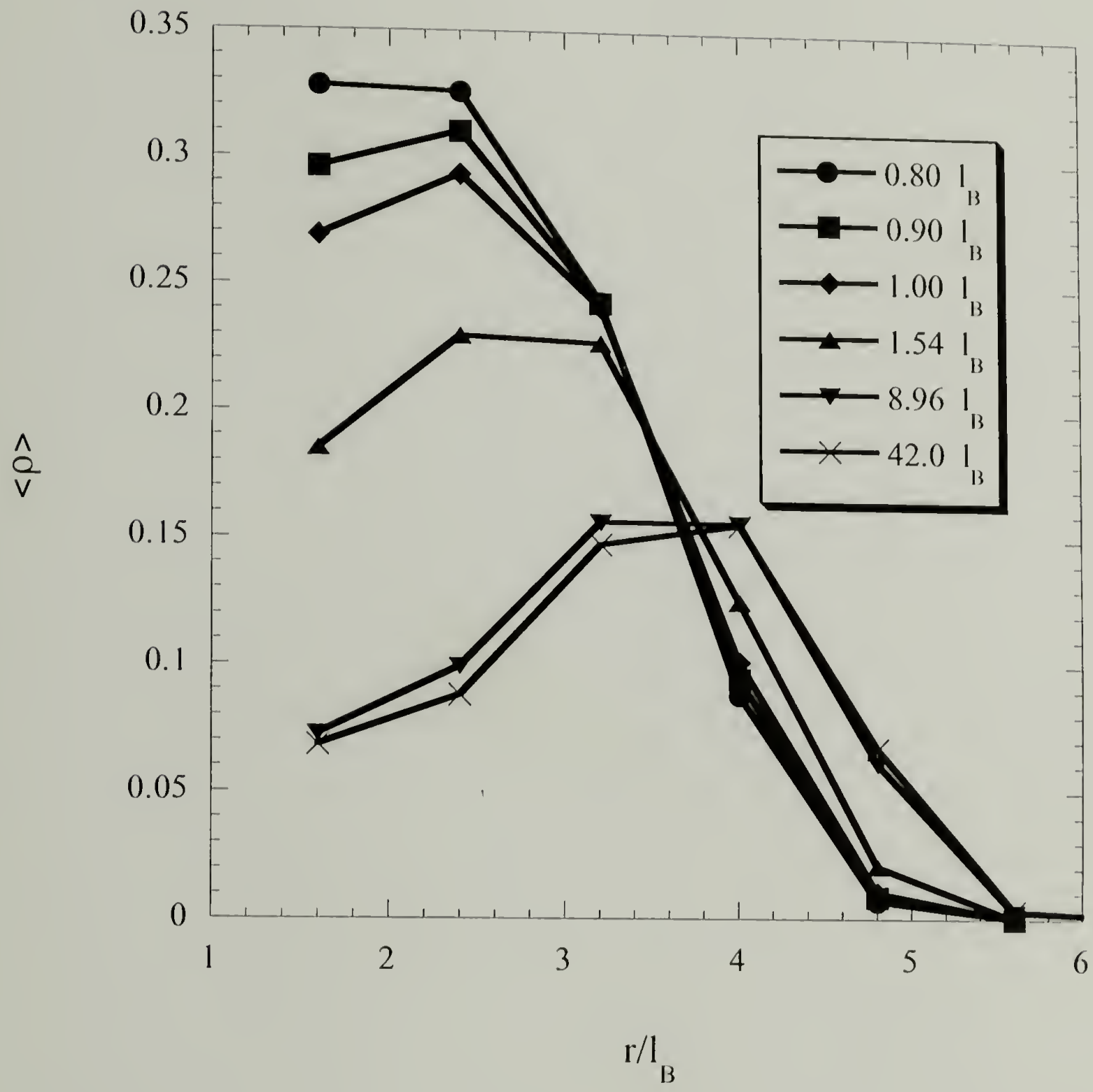

Figure 3.2: Typical dendrimer density profiles. Data for 6^{th} generation with $|q| = 1.0$ shown.

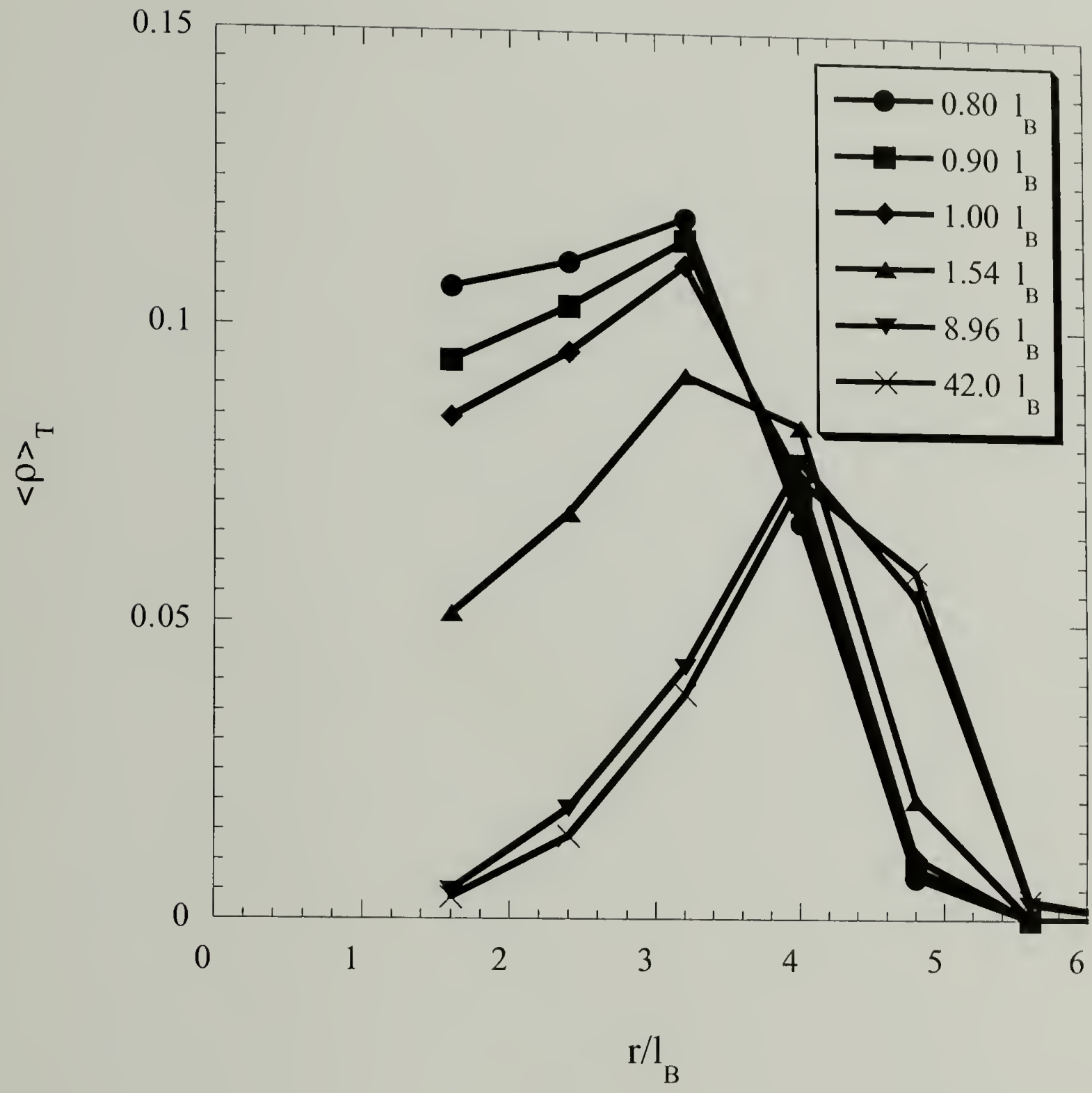

Figure 3.3: Typical dendrimer terminal group distributions. Data for 6^{th} generation with $|q| = 1.0$ shown.

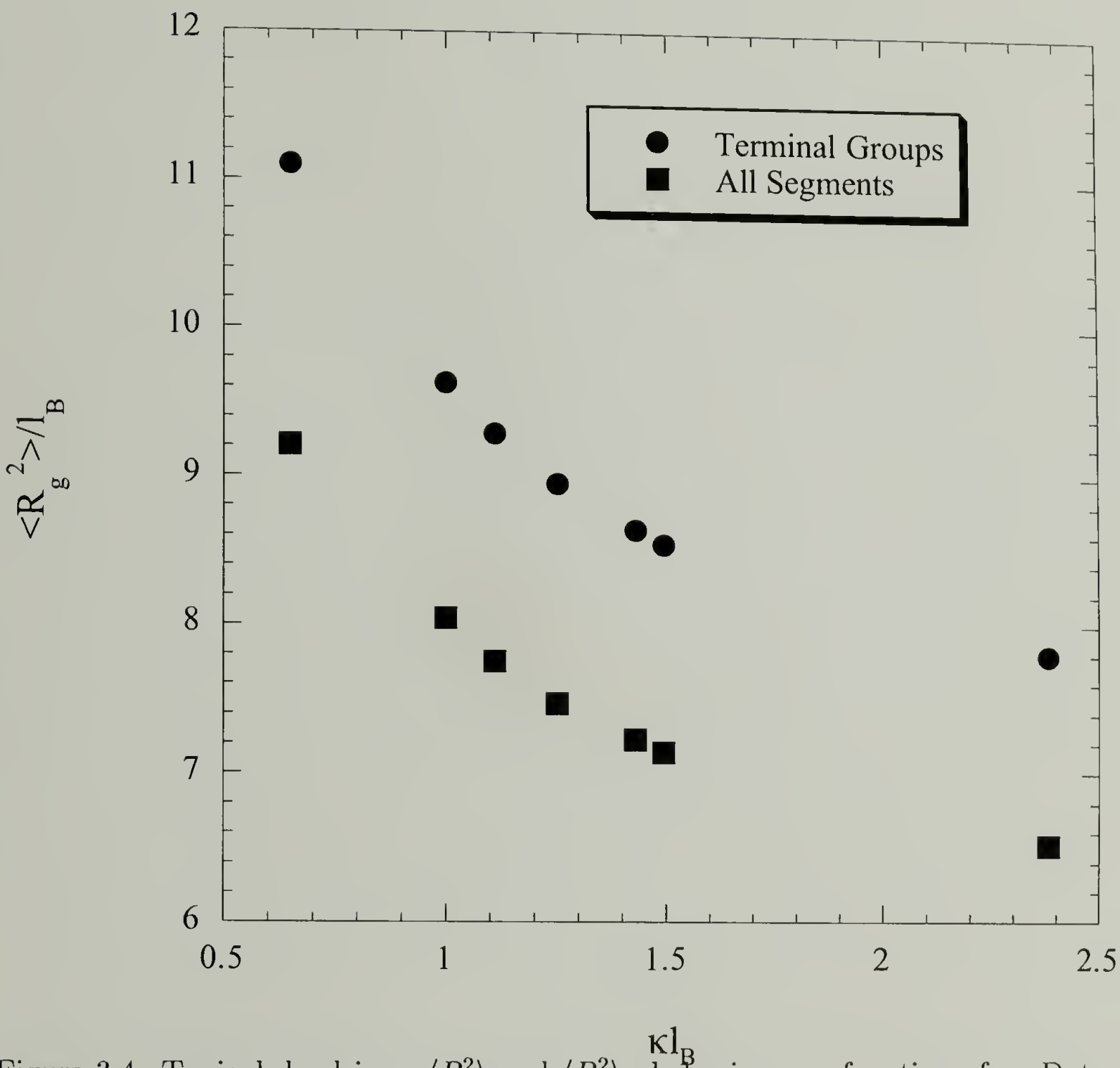

Figure 3.4: Typical dendrimer $\langle R_g^2 \rangle$ and $\langle R_g^2 \rangle_T$ behavior as a function of κ. Data for 6^{th} generation with $|q| = 1.0$ shown.

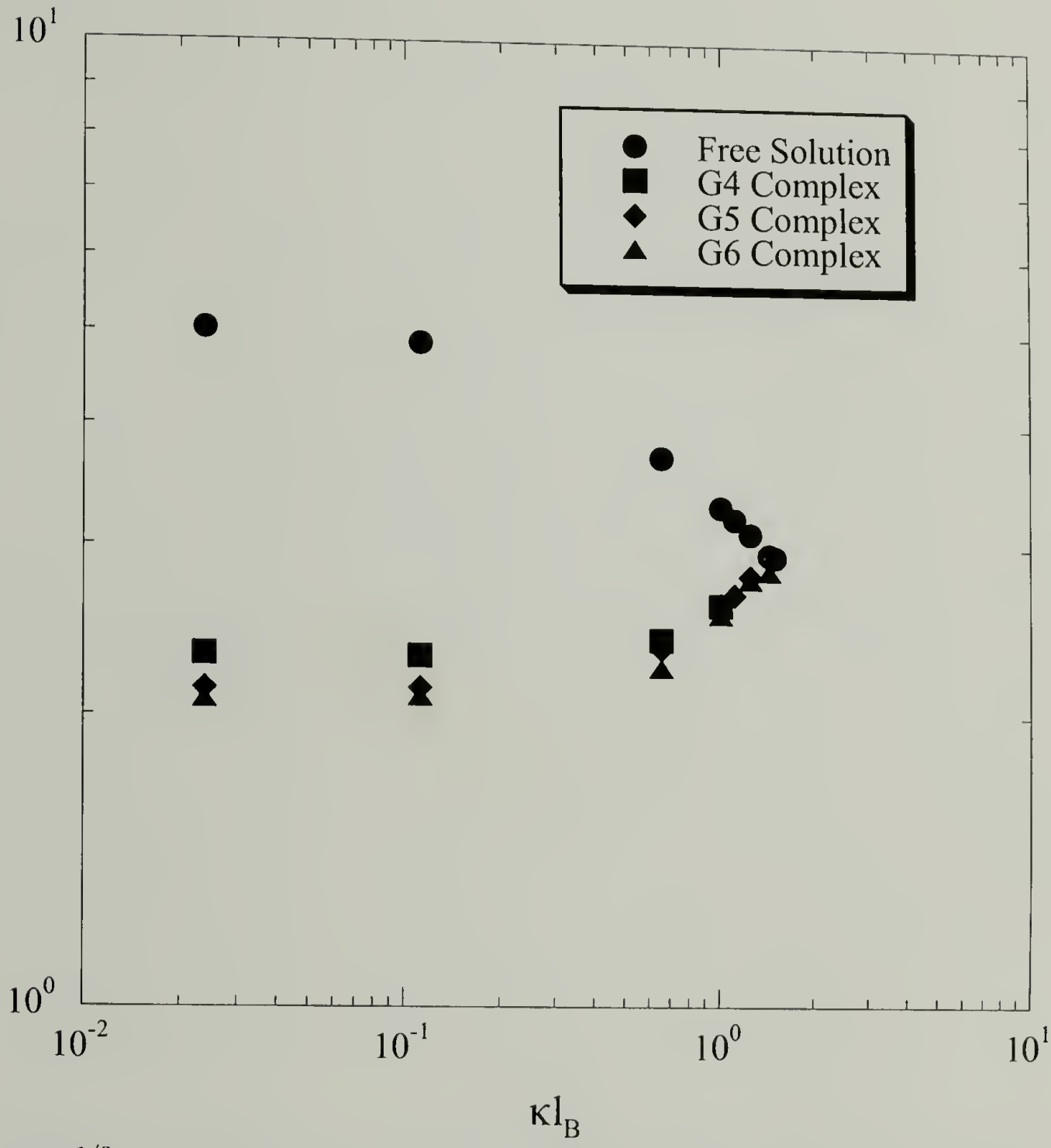

Figure 3.5: $\langle R_g^2 \rangle_L^{1/2}$ as a function of κ and complexing dendrimer generation. Data for 30 bead chain with $|q| = 1.0$ shown.

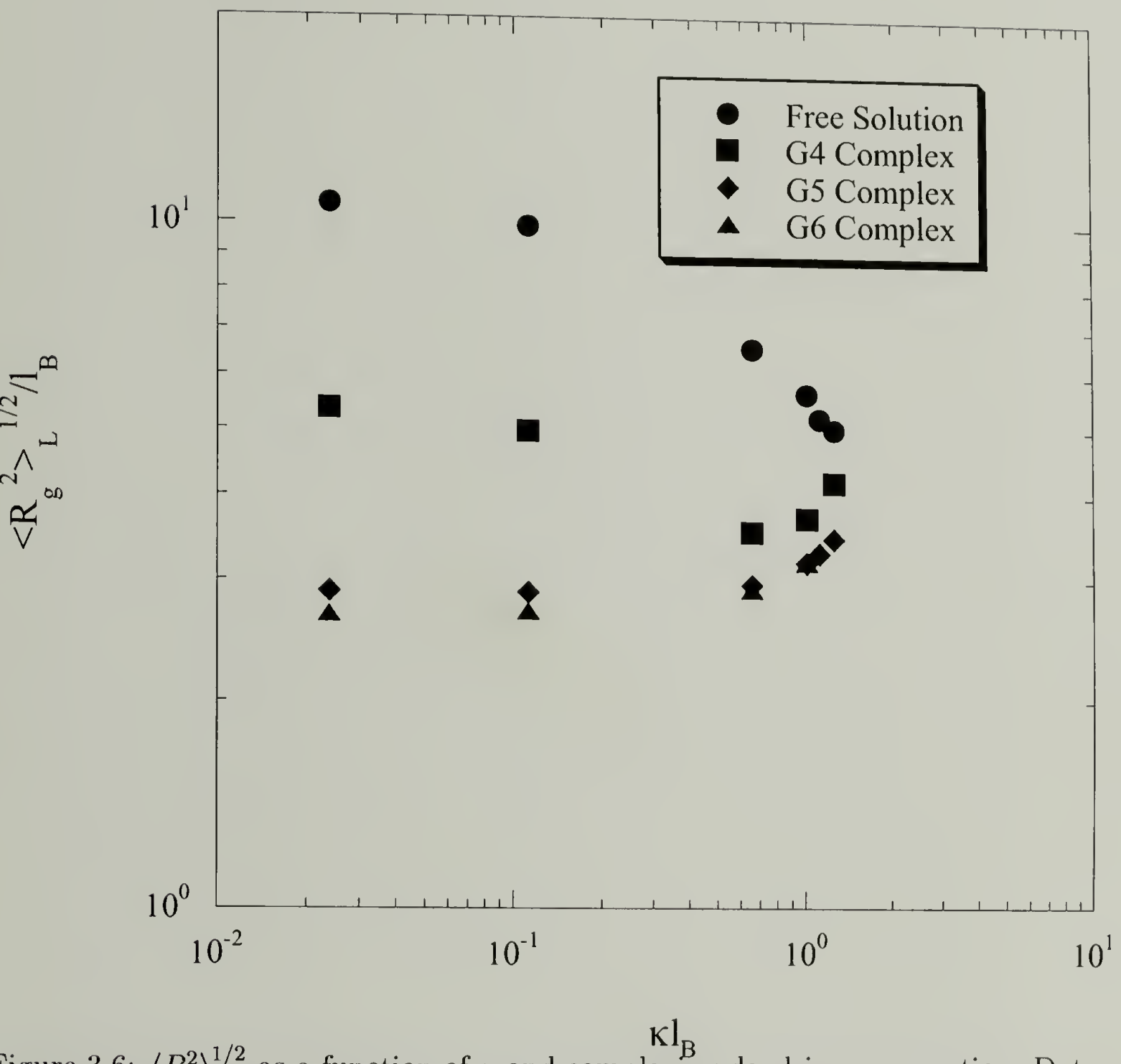

Figure 3.6: $\langle R_g^2 \rangle_L^{1/2}$ as a function of κ and complexing dendrimer generation. Data for 60 bead chain with $|q| = 1.0$ shown.

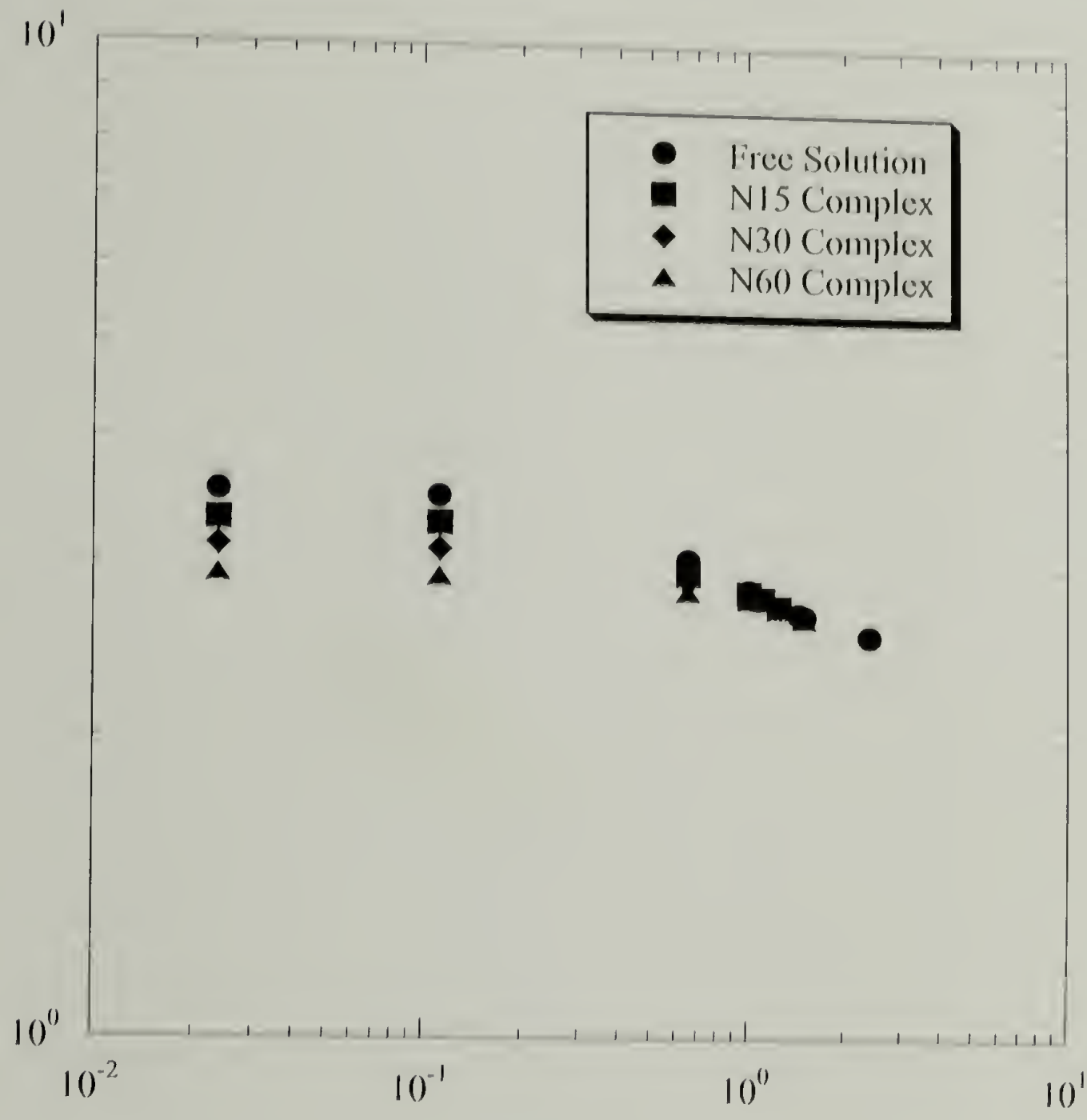

Figure 3.7: $\langle R_g^2 \rangle_D^{1/2}$ as a function of κ and complexing chain length. Data for 6^{th} generation with $|q| = 1.0$ shown.

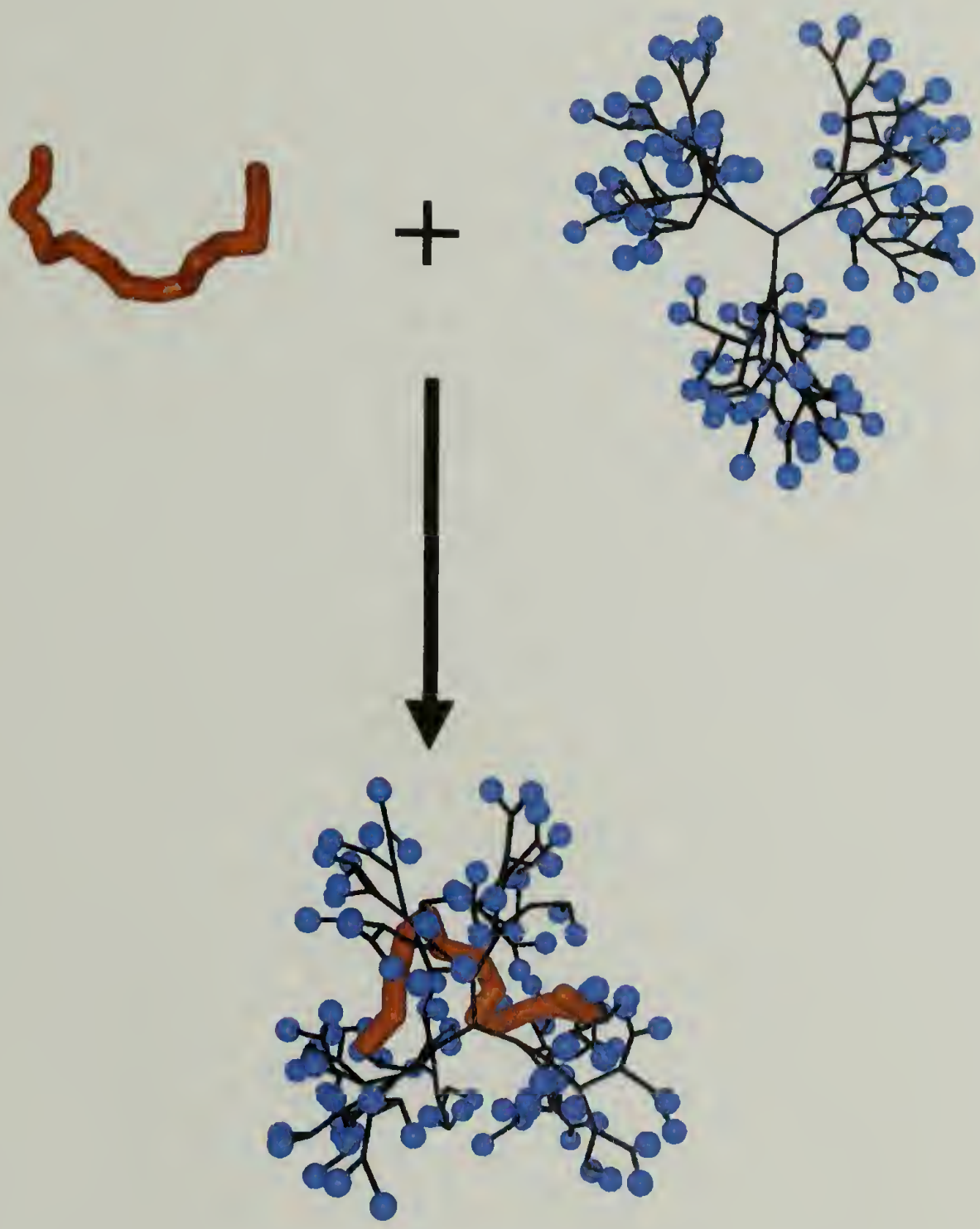

Figure 3.8: Encapsulation of a 15 bead chain by a 6^{th} generation dendrimer with $\kappa = 42.0 l_B$ and $|q| = 1.0$.

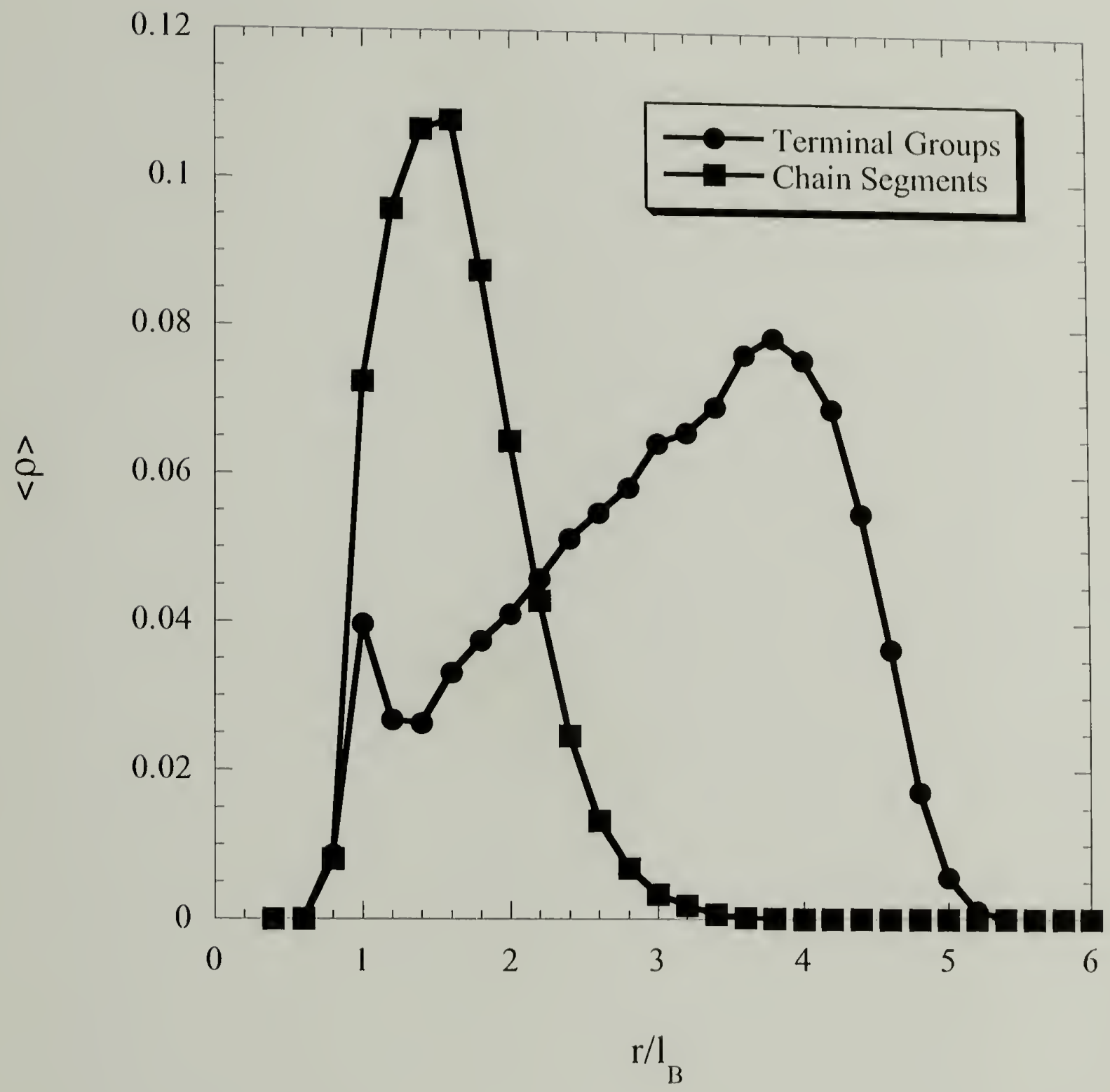

Figure 3.9: Terminal group and chain density profiles for a 6^{th} generation dendrimer encapsulating a 15 bead chain. Data for $\kappa = 42.0 l_B$ and $|q| = 1.0$ shown.

Figure 3.10: Encapsulation of a 5^{th} generation dendrimer by a 60 bead chain with $\kappa = 1.0 l_B$ and $|q| = 1.0$.

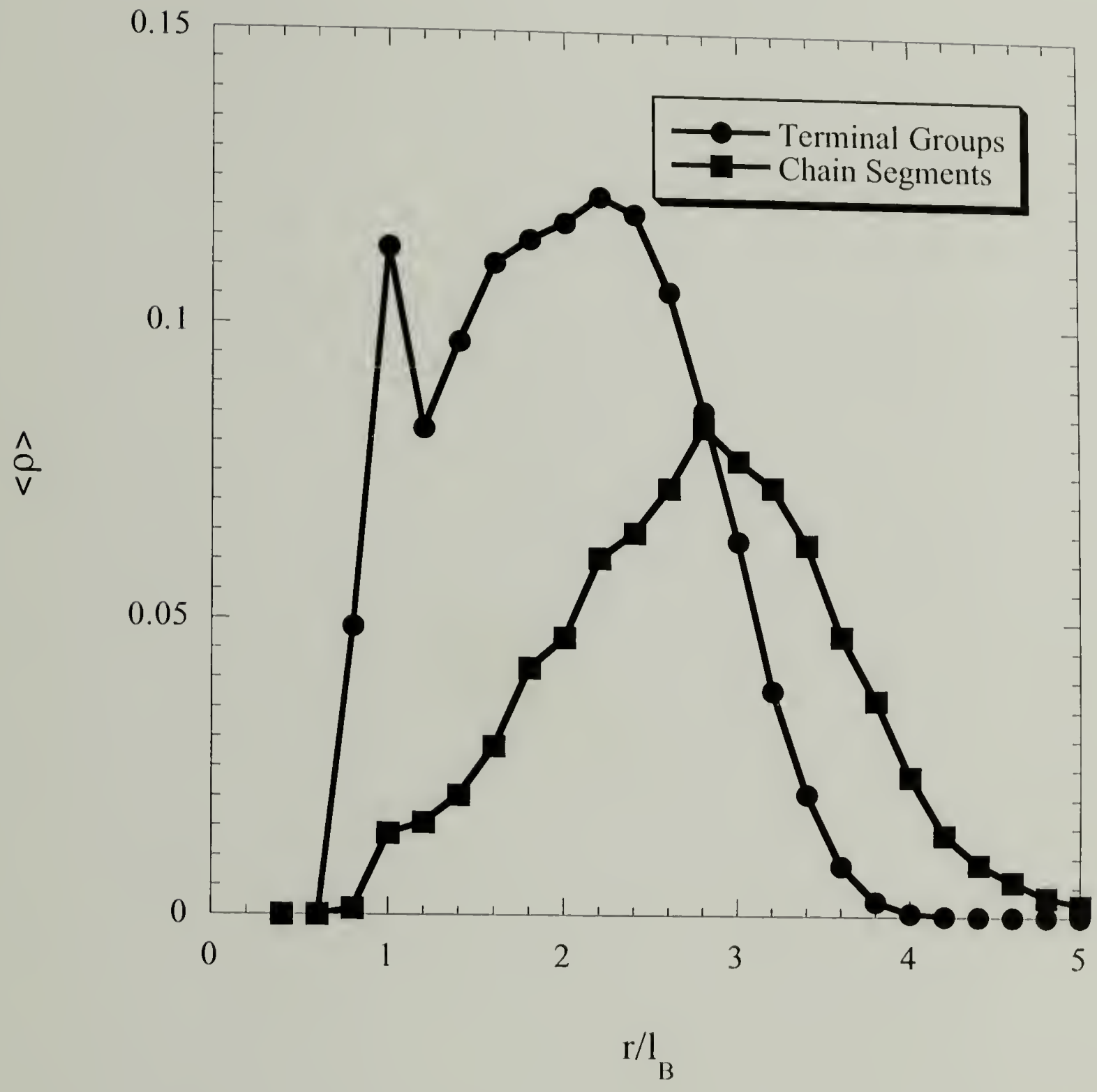

Figure 3.11: Terminal group and chain density profiles for a 60 bead chain encapsulating a 5^{th} generation dendrimer. Data for $\kappa = 1.0 l_B$ and $|q| = 1.0$ shown.

Figure 3.12: The "ball and chain" configuration of a 60 bead chain complexing to a 4^{th} generation dendrimer with $\kappa = 8.96 l_B$ and $|q| = 1.0$.

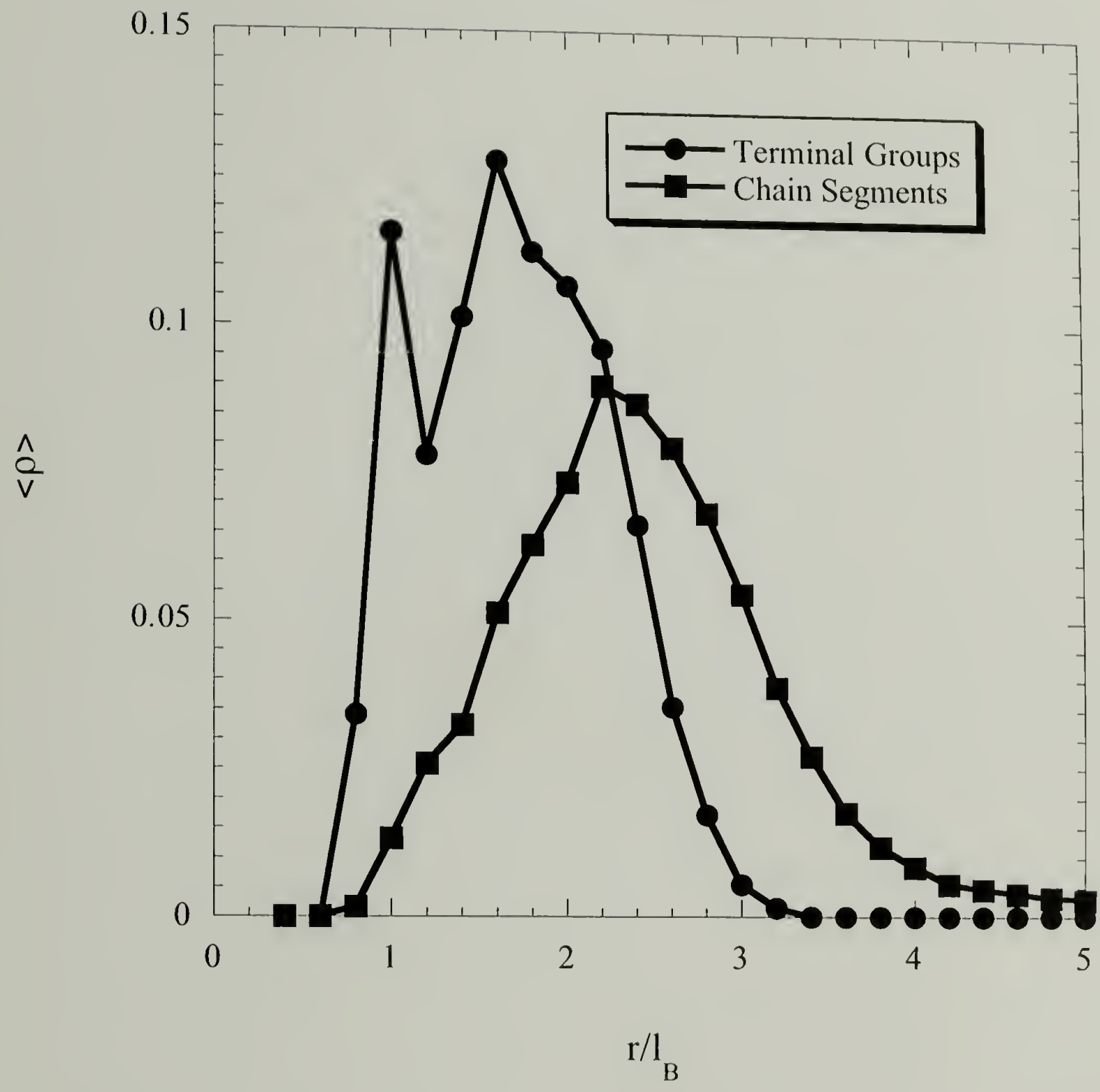

Figure 3.13: Terminal group and chain density profiles for a 60 bead chain complexing to a 4^{th} generation dendrimer with $\kappa = 8.96 l_B$ and $|q| = 1.0$.

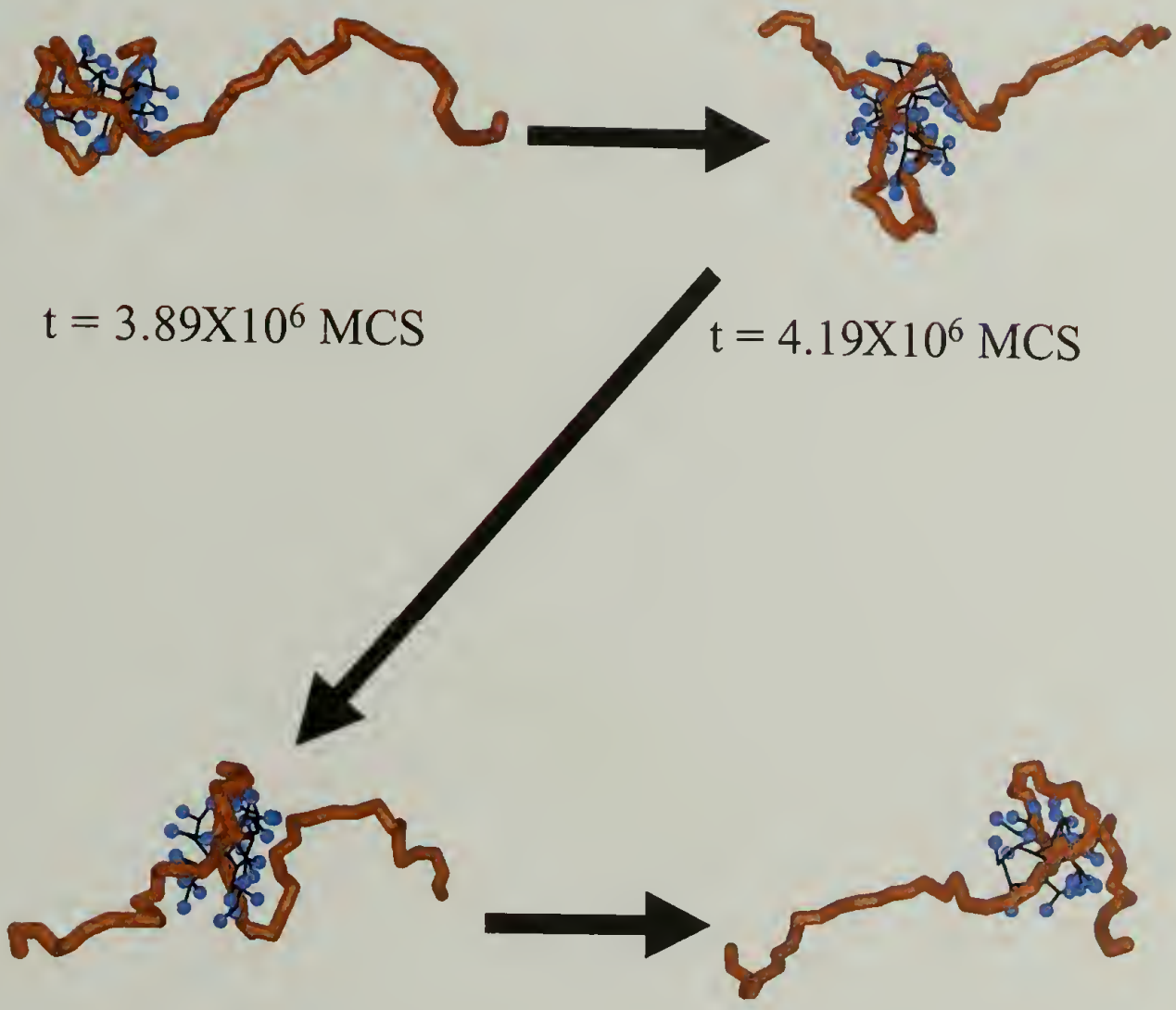

Figure 3.14: 4^{th} generation dendrimer "walking" along a 60 bead chain with $\kappa = 8.96 l_B$ and $|q| = 1.0$.

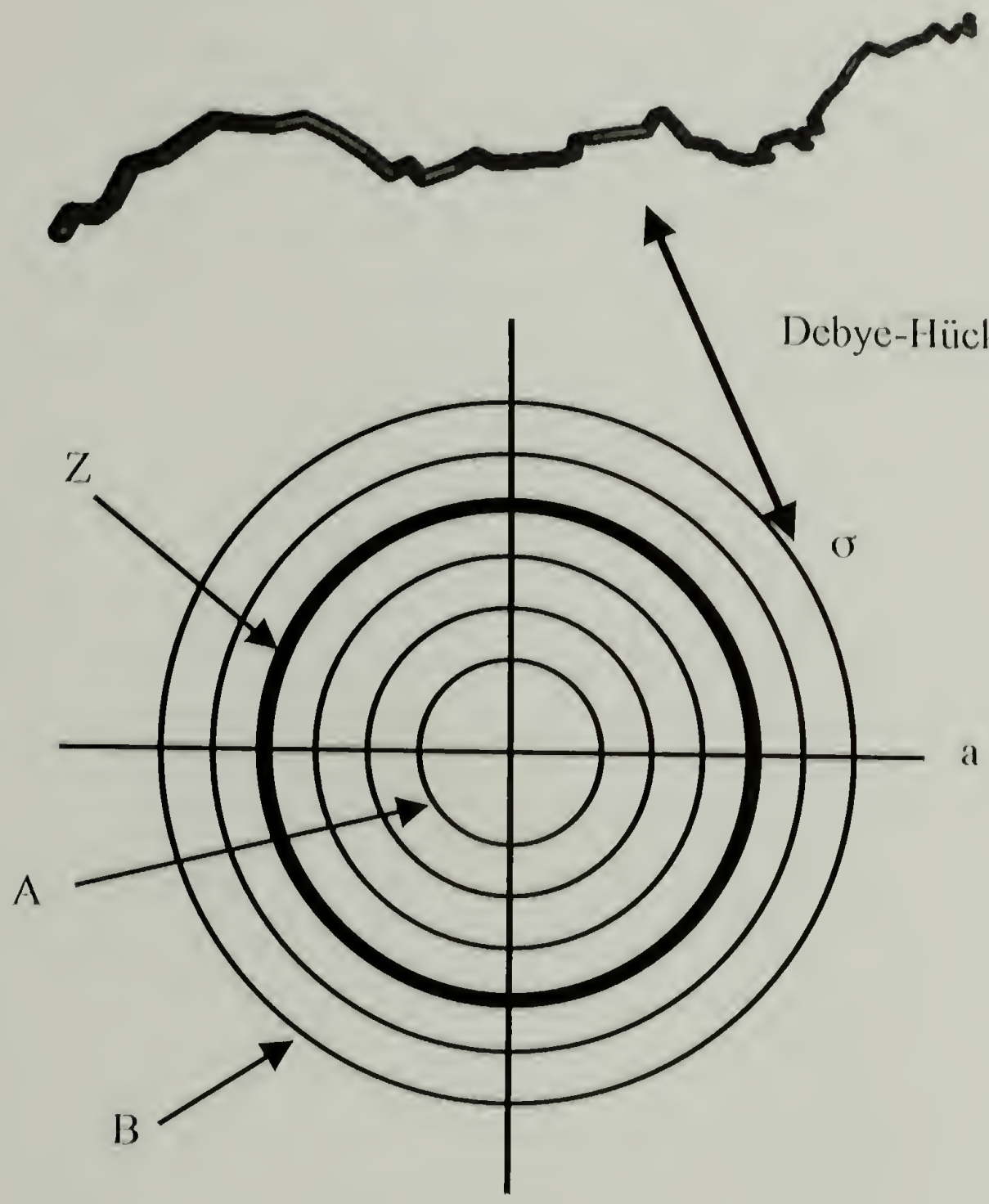

Figure 3.15: Charged concentric shell model for polymer-dendrimer complexation employed in theoretical analysis. Every shell except that falling at Z is permeable. All shells fall between A and B away from the center of the dendrimer. σ for each is determined by the dendritic terminal group distribution.

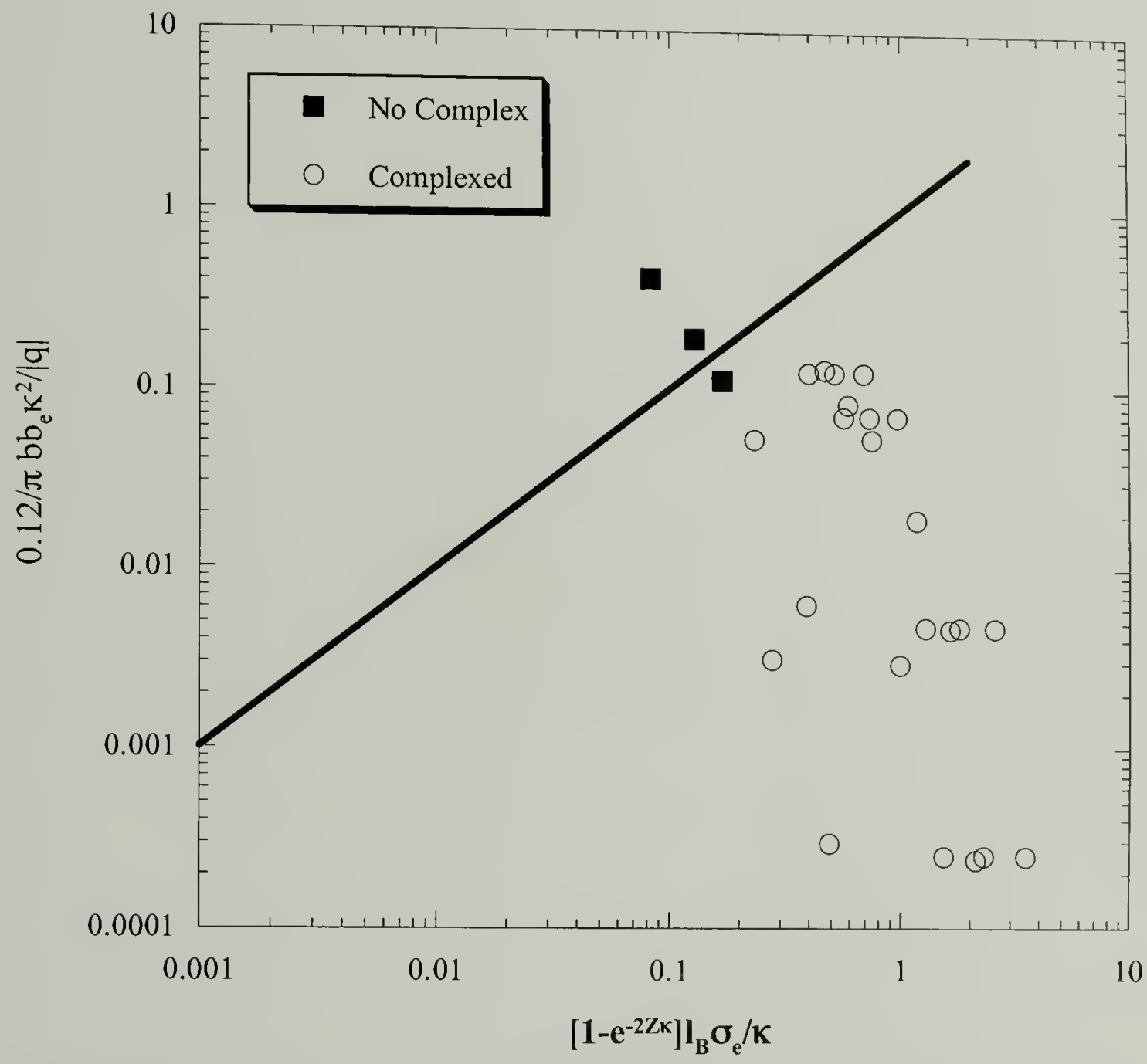

Figure 3.16: Simulation results for 60 bead chains complexing to $4^{th}, 5^{th}$, and 6^{th} generation dendrimers. $|q| = 1.0, 0.5$, and 0.1. κ^{-1} in the range $42.0l_B - 0.8l_B$.

CHAPTER 4

POLYMER CRYSTALLIZATION

4.1 Introduction

Small molecules undergo a first order phase transition from an amorphous liquid into a crystal via a nucleation and growth mechanism when quenched to temperatures in the metastable region.[63] In this process, thermal fluctuations give rise to crystal nuclei larger than the critical size required for stability. These nuclei then provide growth surfaces for further ordering of the surrounding amorphous material. In this case, the characteristic size of the molecules is much smaller than that of the crystal and each molecule only participates in an individual crystalline domain. The picture becomes much more complicated when these small molecules are tethered together into a polymer.[64–66] On first examination, one may doubt that long, possibly entangled chains are even capable of forming crystals. However, as first proposed by Storks[67] in 1938 and later verified by Keller[68] in 1957, polymers do form ordered domains of chain folded structures. The thickness of these lamellae is orders of magnitude less than the contour length of the polymer and, hence, individual chains may also participate in multiple crystalline domains.

Given these fundamental differences between small molecule and polymer crystals, one may reasonably ask how the connectivity of the polymer alters the growth mechanism of the crystal. Despite 60 years of intense investigation, many questions remain unanswered regarding this mechanism. For example, experimental

evidence indicates that in the earliest stages of crystallization structural organization takes place prior to full crystallographic assembly.[69–77] In particular, simultaneous small angle and wide angle X-ray scattering results suggest that a spinodal mode, rather than nucleation and growth processes, give rise to the initial structures.[69–75] Experimental observation also demonstrates that, independent of the crystallization conditions, the initial lamellar thickness is approximately 10 nm. This is two orders of magnitude below thermodynamic estimates. Thus, the exact source of this length selection remains elusive. The widely accepted analytical model for the activity at the growth front, due to Lauritzen and Hoffman,[78–80] employs a nucleation and growth mechanism to predict many experimental observations on polymer crystallization kinetics. Unfortunately, the theory presents only a vague picture of the molecular behavior and suffers from serious criticism in the literature.[81–86] The internal dynamics of the crystal is also poorly understood. Once the crystal is formed, it is not a static entity, but rather undergoes a constant internal rearrangement that results in an increase in lamella thickness. Finally, the origin of the large-length scale structures, such as growth sectors, lamellar twisting, and spherulites, is unknown.

Motivated by the complexity of the problem and the success of Liu's[87] prior investigations, we employed Brownian dynamics simulations to provide a molecular level view of the phenomenon and to address some of these key issues. We find that five concurrent processes comprise the mechanism of polymer crystallization from dilute solution. Our simulations suggest that a nucleation and growth mechanism, not spinodal dynamics, gives birth to seed crystals in the initial stages of homogeneous crystallization. Chains diffuse to the growth front prior to contact with the seed crystal. We observe that the chains then simultaneously adsorb and crystallographically (planer zig-zag conformation) attach to the crystal, as previ-

ously suggested by other authors.[81] The newly added, folded chains undergo a rearrangement on the growth front to form stems that are commensurate with the growing crystal thickness. Meanwhile, chain dynamics within the crystal result in an overall thickening of the lamella. The combined effect of these events yields the experimentally observed phenomena, as described below.

4.2 Model and Simulation Technique

4.2.1 Model

A united atom, bead-spring model of polyethylene was employed to capture the molecular details of crystallization while preserving computational tractability. In this model, each methylene unit is treated as a bead and is described by force field parameters modeled after the work of Paul et al.[88] Our model differs slightly from that of those authors in that the terminal methyl groups are also treated as methylene units, the chain torsional stiffness is higher, and the bonds are more flexible. These slight alterations result in a higher computational efficiency. Previously, Lin and Muthukumar demonstrated that this model captures many of the salient features of polymer crystallization.[87] Similar computer simulation approaches have recently appeared in the literature.[89–97]

Crystallization occurs in our system as a result of the competition between the pairwise attractive interactions between the beads and the conformational angle constraints along the chain backbone. Figure 4.1 illustrates the force field and the united atom model. The Lennard-Jones interaction, U_{LJ}, acts between every pair of beads in the system to represent the van der Waals attractions and the hard-core repulsions. U_{LJ} is given by

$$U_{LJ} = \epsilon \left| (\sigma/r)^{12} - 2\,(\sigma/r)^{6} \right| \tag{4.1}$$

where r is the distance between the two beads. The interaction strength ϵ is set to 0.112 kcal/mol. The coefficient of 2 for the attractive portion of the potential results in a minimum at $r = \sigma$, the equilibrium distance between segments. σ is 4.53Åfor beads further than five repeat units apart along the chain backbone. In order to enhance computational stability, beads that are closer than 5 repeat units along the chain interact with a σ value of 1.54Å. This is expected to have little effect on the behavior of the chain other than slightly increasing the chain's local flexibility. However, the model's stiff torsional constraint overwhelms this enhancement. The potential energies associated with the bond angle θ and the torsion angle ϕ have the form

$$U_\theta = k_\theta \left(cos\theta - cos\theta_0\right)^2 \tag{4.2}$$

and

$$U_\phi = k_1 \left(1 - cos\phi\right) + k_2 \left(1 - cos2\phi\right) + k_3 \left(1 - cos3\phi\right) \tag{4.3}$$

where $\theta_0 = 109^o$, $k_\theta = 60.0$ kcal/mol, $k_1 = 3.02$ kcal/mol, $k_2 = -0.560$ kcal/mol, and $k_3 = 2.58$ kcal/mol. The bonded interactions are approximated by the harmonic potential

$$U_b = k\left(l - l_0\right)^2 \tag{4.4}$$

where l is the bond length and l_0 is the equilibrium bond length. The spring constant k is set to 115 kcal/mol Å^2 and $l_0 = 1.54$ Å.

The magnitudes of the force field parameters result in a model chain with essentially rigid bonds and bond angles. Thus, the torsion angles change the most during the simulations. The exact choices of bond length and bond angle stiffnesses are unimportant as long as they are high relative to the torsional flexibility.

Reduced units were used throughout the simulations and all data presented here are expressed in those units. The dimensions of the system are normalized such that the mass M of each united-atom, the equilibrium bond length l_0, and the Lennard-Jones strength parameter ϵ are all set to 1. Thus, l_0 is the fundamental unit of length, ϵ is the unit of energy, and $t^* = \frac{1}{\sqrt{\epsilon/M\sigma^2}}$ is the unit of time.

4.2.2 Algorithm

The equation of motion for this system is given by the Langevin equation[98, 99]

$$\frac{d^2\vec{R}}{dt^2} = -\zeta\frac{d\vec{R}}{dt} - \vec{\nabla}U + \vec{F}_{rand}. \tag{4.5}$$

The first term on the right hand side represents the solvent's resistance to the bead's motion. ζ is the frictional coefficient and has the arbitrary value of $1.0/t^*$. The second term on the right is the force due to the interaction of the beads with moieties other than solvent in the system. U is the sum of the potentials described above. The last term describes the molecule's coupling to the solvent thermal bath. The random force, $\vec{F}_{rand}$, has zero magnitude on average and has a correlation function described by

$$\langle \vec{F}_{rand}(t) \cdot \vec{F}_{rand}(t') \rangle = 6k_B T\zeta\delta(t - t'). \tag{4.6}$$

The Maxwell distribution given below satisfies these requirements. The Box-Muller algorithm[100] was employed in the simulations to obtain values from this distribution.

$$W(\vec{F}_{rand}) = \left(\frac{1}{4\pi\zeta k_B T}\right)^{3/2} exp\left[\frac{-\vec{F}_{rand}^2}{4\zeta k_B T}\right] \tag{4.7}$$

The velocity Verlet integration algorithm[99, 101, 102] was employed to calculate the motion of the beads. Specifically, at the beginning of the time steps of length $H = 0.04t^*$, the positions of the beads were advanced by $\Delta\vec{r} = H\vec{V} + \frac{H^2\vec{F}}{2}$ and the velocity was partially updated by $\Delta\vec{V} = \frac{H\vec{F}}{2}$. Next, the pairwise forces were updated, $\vec{F}_{rand}$ was added to each bead, and the viscous resistance calculated. Finally, the velocity due to the forces at the end of the time step was added by $\Delta\vec{V} = \frac{H\vec{F}}{2}$.

A few approximation techniques were used to further facilitate the simulation. In all the simulations, the 2-body potentials were not calculated exactly, but were estimated from a lookup table. Specifically, a table of $\vec{F}_{LJ} = -\vec{\nabla}U_{LJ}$ values was calculated at the beginning of the simulation with a Δr value of $0.0006l_0$. The range of the table spanned r values from 0.0 to $6.5l_0$. Beads separated by distances greater than $6.5l_0$ did not interact. Similarly, $\vec{F}_b = -\vec{\nabla}U_b$ was approximated within the bond length range of $0.5l_0$ to $3.5l_0$ at a spacing of $\Delta l = 0.0006l_0$. If the bond length ever fell outside of the range of the table the simulation was stopped. This constraint prevented the occurance of "phantom" chains.

In the multi-chain studies involving up to 46 chains, each of 200 beads, we benefited from a parallel scheme in calculating pairwise interactions. We divided the particles up evenly over the number of processors available and each processor carried out the above described Verlet integration for its subset of particles. Since

the integration includes the computationally intensive step of calculating the pairwise forces on that subset, each processor must have the coordinates for all of the particles at each step. To accomplish this, the new locations are communicated to a central node which collects them from all the integrating processors. The central node then updates the integrating processors with the complete set of new locations. A straight forward way to implement this would be to have each integrating processor calculate the new locations for its subset of particles, pass the new coordinates to the central node, wait for the central node to pass the complete set of new coordinates back, and then calculate the forces required for the next time step. However, we introduce an approximation to take full advantage of our Ethernet connected Alpha-based system, a so-called "Beowulf" cluster that is described in Appendix B. The distributed memory nature of such a system requires the relatively slow network communication of the coordinates between processors. If the naive route were taken, each processor would be idle for relatively long periods of time during this communication step. This situation would eliminate any gain due to parallelization. To overcome this hardware limitation, we apply the following scheme: i) each processor calculates the new locations for its subset and sends the coordinates to the central node. ii) The integrating processors then calculate the pairwise forces acting on its subset of particles using the new locations of its subset and the old locations of the other particles. Concurrently, the central node sends the complete set of new locations to each processor. iii) The integrating processors receive the new locations, calculate the remaining forces, and finish updating the velocities. Since the calculation of the pairwise forces is the most computationally intensive portion of the simulation, the slow communication step is masked if an appropriate ratio of processors to particles is chosen. This technique does violate the classical mechanics rule of symmetric forces since two interacting parti-

cles that are updated on different nodes will not know the exact locations of each other. However, because small time steps are used in this study, the locations do not change much in a single integration iteration. Thus, the error introduced due to these inaccuracies may be expected to be overwhelmed by the applied thermal noise. A comparison of results from simulations done with and without this parallel technique shows this to be the case.

4.3 Results and Discussions

4.3.1 Equilibrium Melting Temperature

The equilibrium melting temperature, T_M, of these model chains was estimated by the following procedure. First, a chain was equilibrated at $kT/\epsilon = 15.0$. Next, the chain was quenched to $kT/\epsilon = 10.0$ and crystallization was allowed to take place. Once a single chain-folded structure was obtained, we performed several simulations at different heating rates ranging from 0.0001 to $0.002\epsilon/t^*$. Discontinuities were observed in the slopes of the total potential energy at the onset and ending of melting. The equilibrium melting temperature was estimated by extrapolation of the observed melting temperature to zero heating rate. The reduced melting temperature is $kT_m/\epsilon = 11.0 \pm 0.2$ for the model parameters listed above.

4.3.2 Early Stages of Crystal Formation

In order to elucidate the mechanism of the formation of the initial polymer crystal structure in homogeneous crystallization, we investigated the behavior of a 2000 united atom chain ($N = 2000$) quenched below its melting temperature. The

chain was first equilibrated at $kT/\epsilon = 20.0$ and then quenched to $kT/\epsilon = 9.0$. This corresponds to a quench depth, $\Delta T = kT_m/\epsilon - kT/\epsilon$ of 2.0.

Nucleation and Growth

As seen in Figure 4.2, several regions of segmental aggregation with some visibly apparent local orientational order rapidly form and are connected by free strands of the same chain. We refer to these regions as "baby nuclei." As time progresses, the monomers in the flexible strands are reeled into the baby nuclei while the orientational order in each nuclei increases. Simultaneously, the competition between nuclei for further growth dissolves some nuclei while others increase in size. Thus, the phenomenology observed is essentially the same as the nucleation and growth mechanism observed in small molecule systems, except that a single polymer chain participates in several growing domains. Similar phenomenology has been observed in simulations of oligomer melts.[94]

Time Dependent Scattering

During the very earliest stages of nuclei formation, the distance between the baby nuclei does not change, but the number of connecting monomers do. To quantify this behavior and facilitate comparisons with experiment, at different times we calculated the spherically averaged single particle form factor, $S(q,t)$, as defined by eq (2.10).

As illustrated in Figure 4.3, a peak in $S(q,t)$ arises at intermediate times. In order to highlight this peak, due to the average distance between the two dominant baby nuclei in this particular study, we subtracted out the scattering of the amorphous chain at time zero. The result, shown in Figure 4.4, is strikingly similar to that observed in experiments[71] investigating the melt, where the background

scattering prior to the quench below the melting temperature is subtracted from the signal post-quench. A key feature of Figure 4.4 is a single distinct peak that remains at a constant q_{max} value and rapidly grows in amplitude.

The time-dependence of the total integrated intensity, I, is plotted in Figure 4.5. For early times, $ln(I)$ is linear in time. At later times ($t/t^* \geq 1000$), I grows very slowly with time. Again, striking agreement with melt experiments[71] is noted.

Without the benefit of the molecular level picture that computer simulation provides, one would be led to attribute this calculated scattering behavior to a spinodal mode of organization. The linearized Cahn-Hilliard-Cook theory of spinodal decomposition would therefore be expected to apply. This theory predicts $S(\vec{q}, t) \propto \exp(2\Omega_q t)$, where Ω_q is the rate of growth of fluctuations with wave vector $\vec{q}$. Further, $\Omega_q \propto q^2(1 - Bq^2)$ with B being a positive constant. Therefore, a plot of Ω_q/q^2 vs q^2 must be linear with a negative slope if spinodal decomposition is present. Figure 4.6 presents Ω_q/q^2 vs q^2 obtained from an analysis of our calculated scattering. Again, as in the case of experiments[74] on melts, we observe agreement over a limited range of q values and significant deviations at the low and high q range. The shape of the curve in Figure 4.6, including the nonlinear deviations, has recently been attributed to correlations between two nuclei connected by a single polymer strand.[66] Furthermore even though our data seems well described by the theory of spinodal decomposition over a limited range of q values, the simulations clearly indicate that nucleation and growth is the mode of structure development for the early stages of polymer crystallization. Thus, we conclude that, though our simulations are of the dilute solution case, other mechanisms than spinodal decomposition may be active in the recent melt experiments, despite the limited agreement with the phenomenology of spinodal dynamics. Whether or not our predictions hold in the dilute solution remains to be established by experiment.

Intra-Chain Crystal Growth

The simulations indicate that two mechanisms are operative in increasing the number of chain segments in the single chain crystal. Figure 4.7 illustrates the later time evolution of the chain's structure. In this figure, a portion of the chain is labeled in blue and the remainder in red to facilitate visualization of the migration of different chain segments into the different crystalline domains. Beyond $t/t^* = 500$, the chain organizes into two crystalline, chain folded lamellae. As stated earlier, the surviving nuclei compete with one another for the remaining free chain segments that tie them together. United atoms are added to each domain in a segment-wise fashion during this struggle while the crystalline lamellae maintain their constant inter-nuclei distance. This process continues until the bridging chain segment is essentially stretched out. Then, a new mechanism takes over. Further addition of segments into the lamellae results in pulling the two nuclei together until they impinge. This is followed by reorganization during which the nuclei merge to form a single lamella. The mechanism of this merger is not a sequential placing of united atoms, but rather a highly cooperative process involving all the segments in the lamellae.

The time dependence of the number of segments between two lamellae, m, may be treated with a simple Fokker-Plank analysis. The free energy of a chain with only two lamellae, such as the $N = 2000$ chain under consideration here, has two contributions as indicated by eq. (4.8) below.

$$\frac{F}{kT} = -(N-m)\,\chi - ln\left[exp\left(-\frac{3}{2}\frac{(m_F l)^2}{ml^2}\right)\right] \tag{4.8}$$

The first term on the right hand side accounts for the favorable addition of more segments to the crystalline domains. The second term represents the entropic

penalty associated with stretching the bridging segments. Here, we ignore surface effects and assume that the distance between the two lamellae is constant. $kT\chi$ is the free energy gain per chain segment for crystallization. m_F is the final value of m such that the constant distance between the two crystals is $m_F l$. l is the projected step length and drops out of the expression.

The Fokker-Plank equation for the time evolution of the distribution function for m, $W_m(t)$, is given by

$$\frac{\delta W_m(t)}{\delta t} = \frac{\delta}{\delta m}\left[\left(\chi - \frac{3m_F^2}{2m^2}\right) W_m(t)\right] + \frac{\delta^2 W_m(t)}{\delta m^2} \tag{4.9}$$

with boundary conditions $W_m(0) = \delta(m_0 - m)$ and $W_m(t_F) = \delta(m_F - m)$. No analytical solution for $W_m(t)$ exists, but a numerical answer is easily obtained via an implicit integration scheme employing standard Gaussian elimination and back substitution.[100] Once $W_m(t)$ is in hand, the most probable value of m at any given time is available. Figure 4.8 presents the comparison between the calculated values for m assuming $\chi = 0.47$ and those observed in the simulation. Good agreement is noted until later times when the two lamellae begin to move together, in violation of the assumption of the above analysis.

4.3.3 Lamellar Thickness Selection

To probe the origin of the lamellar thickness selection, we calculated the free energy landscape as a function of a measure of lamellar thickness, L, by following the folding of single chains at a given quench depth and utilizing a histogram technique[103]. L is the the radius of gyration along the axis parallel to the chain backbone within the crystal. The free energy $F(L)$ is estimated as $F(L) = -kTln\left(\frac{n(L)}{\mathcal{N}}\right)$, where $n(L)$ is the number of times the system visited

states between L and $L + \Delta L$, and $\mathcal{N}$ is the total number of states visited. $\Delta L/l_o$ is 2.0. Each estimate was constructed by performing simulations for $60{,}000t^*$ and sampling every $20t^*$. Nine independent simulations were used for $N = 200$ and $N = 250$. Twenty-eight were employed for the estimate for $N = 300$.

Effect of Torsional Constraint

The importance of the torsional constraint to the roughness of the free energy profile is made immediately obvious by comparing Figure 4.9 with Figure 4.10, the free energy profiles of $N = 200$ at $kT/\epsilon = 9.0$ with and without torsional interactions.

Effect of Chain Length

Figures 4.10-4.12 illustrate our estimates of the free energy profiles for $N = 200, 250$, and 300 at $\Delta T \approx 2$. Wells are noted in the profiles and are separated by free energy barriers. Each well corresponds to a different number of stems in the crystal. For example, 6, 5, and 4 stem structures are observed for $N = 200$. Increasing N results in the addition of more wells. Thus, the profile for $N = 300$ displays 4 wells corresponding to structures with 4 to 7 stems. The minimum in $F[L]$ is observed to be near $L/l_o \approx 9$ for all three chain lengths. This corresponds to different numbers of stems for different values of N. However, the approximate number of chain segments in each stem at this minimum is always approximately 40. Thus, as N increases, the chains increase the number of stems in the crystal to accommodate the target minimum $F[L]$ crystal thickness. Also note that the barrier in $F[L]$ between the minima increases with N.

Effect of Quench Depth

To investigate the effect of quench depth on the free energy profiles, simulations for $N = 300$ were carried out at $kT/\epsilon = 5, 7$ and 9 corresponding to $\Delta T \approx 6, 4$, and 2, respectively. Figures 4.12-4.14 illustrate these results. The obvious effect of increasing the quench depth is an increased roughness near the minimum free energy. Averaging L from the simulations also yields the well-known inverse relationship between quench depth and lamellar thickness.[104]

Kinetic Pathways to Target Thickness

Close examination of the simulations indicates that the chains tend to "melt" while jumping a barrier. We estimated the free energy landscape as a function of both lamellar thickness and orientational order, $F[L, S]$, to quantify this behavior. The global orientational order parameter, S, measures the degree of crystalline order in the chain folded structure.

$$S = \frac{\langle 3cos^2\phi - 1 \rangle_{pairs}}{2} \tag{4.10}$$

ϕ is the angle between any pair of vectors that join two chain segments. $\langle\rangle_{pairs}$ indicates an average over all such vector pairs in a given chain conformation. $F[L, S]$ was approximated using a two dimensional histogram such that $n(L, S)$ replaces $n(L)$. $n(L, S)$ is the number of times the chain visited a state between L and $L+\Delta L$ and an orientational order between S and $S+\Delta S$. Figure 4.15 presents our estimate of $F[L, S]$ for $N = 200$ at $\Delta T \approx 2.0$. Similar graphs are obtained for $N = 250$ and 300. Configurations gathered for Figure 4.10 were used in this estimate. Three valleys are noted in the landscape along the L axis. These correspond to the three chain folded structures reflected in Figure 4.10 above. Given this landscape, one

may ask what route a chain will take to travel from one valley to the next. Many paths are possible, but there are two limiting cases. The chain may maintain its orientational order and thereby jump the large free energy barrier required to get to the next well. Or, it may disorganize and cross the saddle of the landscape and then slide towards higher S values in the new valley. The latter journey is most often observed in the simulations. We therefore postulate that several metastable states may be visited in the process of chain folding, but fluctuations to increased entropy aid in the evolution of the chain to its globally stable conformation.

4.3.4 Mechanism of Crystal Growth

We carried out very long simulations with as many as 9000 united atoms with the following protocol. First, we placed a single chain crystal at the origin. Next, a self-avoiding random chain was placed at a random location on a sphere whose radius is 1.5 times the radius of gyration, Rg, of the crystal. The new system was equilibrated with the Langevin dynamics algorithm for $5000t^*$. If the chain failed to add any segments to the crystal by the end of the addition period, the run was rejected and the crystal's coordinates were reset to their values at the beginning of the period. A new attempt to add a chain was then made. If the chain added to the crystal, the process was repeated by moving the crystal to the origin and adding a new self-avoiding random chain to the simulation. This procedure corresponds to the conditions of Regime I in Hoffman's nomenclature. This process was repeated until forty-five chains were in the crystal, for $kT/\epsilon = 7.0, 8.0$, and 9.0 corresponding to $\Delta T \approx 4.0, 3.0$, and 2.0, respectively.

Figure 4.16 illustrates the addition of the 40^{th} chain to a 39 chain crystal at $\Delta T \approx 2.0$. The crystal reels in the chain one segment at a time, crystallographically attaching each to the growth face. This process continues until the entire chain

adds to the crystal. Once adsorbed, the chain continues to rearrange until its fold length is commensurate with that of the growth face. The rate limiting step for the addition of the chain to the crystal is the diffusive contact with the surface. Once a few segments have come into contact with the crystal, the chain rapidly adds to the growth front. Similar behavior is generally noted for $\Delta T \approx 3.0$ and $\Delta T \approx 4.0$. However, at the deep quench depth of $\Delta T \approx 4.0$, the incoming chain begins to crystallize prior to completely adding to the growth face, as illustrated in Figure 4.17. Thus, as in the terminal stages of single chain crystallization discussed above, a cooperative merger takes place in some cases at this value of ΔT and may result in the formation of new growth faces if the merger is imperfect, as illustrated in Figure 4.18 after the addition of the 25^{th} chain. As a result, the crystal grown at $\Delta T \approx 4.0$ began adding chains on what was once a fold surface after the addition of the 25^{th} chain. This observation is consistent with the observation that branching becomes more likely at higher undercoolings.

The rapid addition of chain segments to the growth face suggests that there is no free energy barrier for the addition of segments or stems to the crystal. We again applied the histogram technique to approximate the free energy as a function of the number of segments added to the crystal, $F[s]$. Our estimates were obtained as above, replacing $n(L)$ with $n(s)$, a histogram reflecting the number of segments, s, from an incoming chain that have added to the growth front. Figure 4.19 clearly shows that there are no large barriers to the addition of the chain segments to the crystal. $F[s]/kT$ rapidly decreases once a few segments have added to the growth face. Some small barriers may exist, corresponding to the formation of the hairpins. However, since the chains added rapidly to the growth face, relatively few samples were available for our estimate. We obtained $n(s)$ from the snapshots of the second through forty-fifth chain adding to the crystal. These snapshots

were saved at a rate of one every $50t^*$. Thus, only 4500 states were used in our approximation of $F[s]$. This limitation necessitated a broad bin width of $\Delta s = 20$ segments. Small barriers, if present, are therefore smoothed out. These results sharply contradict the underlying assumptions of the Lauritzen-Hoffman[78–80] theory and its generalizations[105–108] that assume large barriers to the addition of more chain segments to the growth front.

4.3.5 Entanglements

As a first step towards investigating the effect of competition among multiple chains for sites on the growth front, a 46 chain crystal was grown at $\Delta T \approx 2.0$ with each chain having $N = 200$. The procedure outlined above was employed with the modification that two chains in close proximity (the distance of closest approach was less than or equal to $1.7l_0$) were added every $5000t^*$. Figure 4.20 illustrates that, even though the two chains began to co-crystallize, the rapid segment-wise addition and cooperative merger described above still dominated. Figure 4.21 demonstrates that $F[s]/kT$ was also largely unchanged from the single chain addition scenario.

4.3.6 The Mechanism of Lamellar Thickening

Chains inside our model crystals move cooperatively. The center of mass of the crystal diffuses in space while the crystal thickens by a process of internal rearrangement. Labeling one chain in the growing structure reveals both this collective motion of the crystal and the internal reorganization, as shown in Figure 4.22 for $\Delta T \approx 2.0$. Here, the oldest chain in the system is depicted at both an early and a late stage of crystal growth. The coordinate origin and an x-y plane are provided for reference. In the early stages, nine other chains surround and interpenetrate the labeled chain which has arranged itself into four stems. The space visible between

the stems indicates a non-adjacent reentry mode for the chain segments. This suggests that the stems have a lateral mobility since the crystal began growing with this single tagged chain. Later, in the presence of thirty-nine other molecules, the labeled chain now spans only three stems. This demonstrates that some chain segments have moved through the crystal lattice, into the fold surface, and back into the crystalline region, in accord with recent NMR data[109]. Figure 4.23 further explores this mobility by mapping segment location for this chain as either in the crystal phase or in the amorphous phase at different times. The wells in this two-state map correspond to chain segments in the amorphous region. All other segments are in the crystal lattice. Early in the growth of the crystal, at $5150t^*$, the oldest chain occupies five stems and four hair pens. Chain segments 0 through 40 are in the crystalline region and segments 41 through 49 are on the fold surface, for example. Later, at $100{,}400t^*$, the chain only spans three stems and two hair pens. Now, segments 40 through 49 have moved into the crystal lattice. Other segments, such as 145, have moved from the lattice to the fold surface.

Figure 4.24 illustrates that two regimes are operative in the time evolution of a single segment's location. The time correlation function of the location $R_s(t)$ of a tagged segment, $\langle (R_s(t) - R_s(t+\tau))^2 \rangle$, is proportional to τ at larger values of τ, characteristic of Brownian diffusion. For smaller values of τ, a new effective power law is observed: $\langle (R_s(t) - R_s(t+\tau))^2 \rangle \propto \tau^{\gamma}$. The value of γ was obtained by averaging the behavior of 8 segments of the 6 oldest chains in the crystals and found to be 0.74, 0.77, or 0.83 for $\Delta T \approx 2.0, 3.0$, and 4.0, respectively. This new law appears as a compromise between the essentially one dimensional random walk ($\langle (R_s(t) - R_s(t+\tau))^2 \rangle \propto \tau^{1.0}$) behavior that the segments undergo within the crystal and the Rouse dynamics ($\langle (R_s(t) - R_s(t+\tau))^2 \rangle \propto \tau^{0.5}$) of the amorphous fold region.[110]

This internal motion yields crystal thickening as the crystal dimension parallel to the chain axis increases with time, as illustrated in Figure 4.25. Further, the combination of the assumed steady flux of chains diffusing to the growth front, the rapid addition of new chain segments to the crystal, and the simultaneous rearrangements also produce the experimentally observed linear radial growth law, illustrated for $\Delta T \approx 2.0$ and 3.0 in Figure 4.26. We omit the data for $\Delta T \approx 4.0$ because the formation of the new growth face on the former fold surface renders the definition of radial growth ambiguous.

4.3.7 Atomistic Details

Finally, our united atom chains, though suitable for capturing the dynamics of the crystal growth mechanism, result in cylindrical crystals with hexagonally packed stems. As a first step towards understanding realistic morphologies, we decorated our united atom chains with the proper atomistic details. Specifically, we dilated crystals obtained as described above by the ratio of the united atom bond length and the atomistic bond length (1.54). This magnified structure allowed more than sufficient room to replace the united atoms with model carbons and hydrogens. The carbons took the physical locations of the united atoms and the hydrogens were randomly placed on the carbons, respecting bond length constraints. The Amber potential[111] was employed to describe the pairwise, bonded, and bond angle interactions. Equation 4.3 continued to describe the torsional constraints. The resulting structure retained the orientational order of the original crystal, but was not crystalline since the atoms were well outside of each other's potential wells. We used this as our initial configuration and carried out our Brownian dynamics simulation as usual. The obvious advantage of this approach is that we avoid the computationally intensive process of growing these crystals one

chain at a time. This is particularly important since adding atomistic detail triples the number of particles to be considered, 12,040 in the example shown in Figure 4.27. Upon resuming the simulation, the atomistic model chains were observed to disorganize into a roughly spherical droplet in the early stages and then they cooperatively reorganized into a crystal. The resulting structure displays the orthorhombic chain orientation and the hexagonal shape observed when polyethylene crystals are prepared from dilute solution.

4.4 Conclusions

In conclusion, we investigated the effect of polymeric chain connectivity on the mechanism of crystallization. We found that in the earliest stages of crystallization, nucleation and growth properly describes the formation of growing domains. Free energy barriers also dictate the initial lamella thickness for the folding of a single chain. Once formed, however, the seed crystal grows via a process of adsorption rather than nucleation and growth. This observation differs from the model often assumed in analyzing crystallization kinetics. The initial fold length, dictated by the free energy barriers for the single chain, controls the initial thickness of the crystal since the incoming chains rearrange to match the growth front. However, as the crystal grows, the fold length increases from its initial value via an internal rearrangement that follows dynamics intermediate between Rouse and Brownian behavior. Finally, the combined effect of these processes yields the experimentally observed phenomena of linear lateral growth laws, lamella thickening, and the formation of growth sectors. The picture presented here challenges the underlying assumptions of Lauritzen-Hoffman theory and its generalizations. We therefore

hope that this work will stimulate more extensive simulations on larger systems under varying conditions, new theoretical models, and new time resolved experiments.

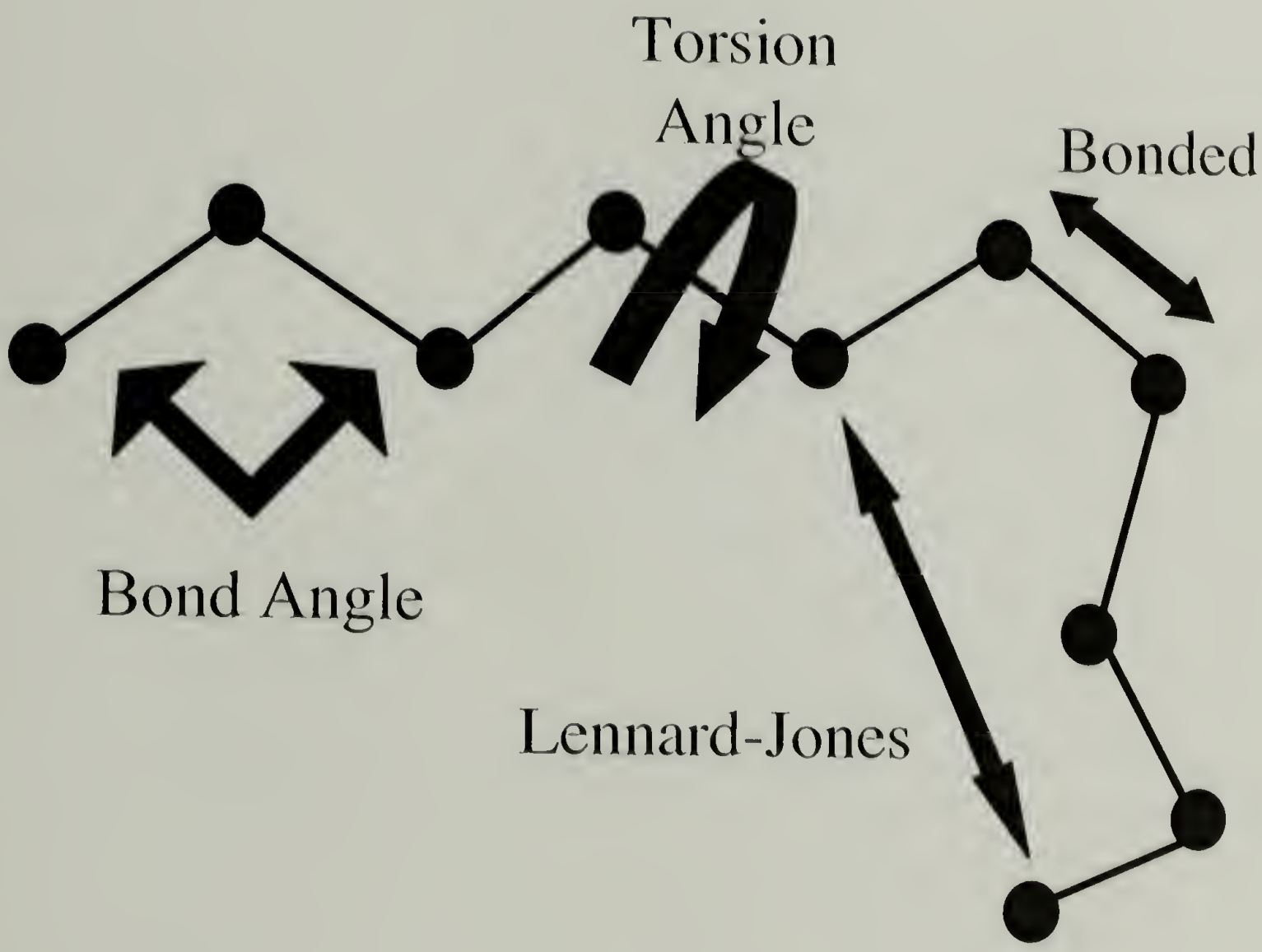

Figure 4.1: The united atom model employed in this study.

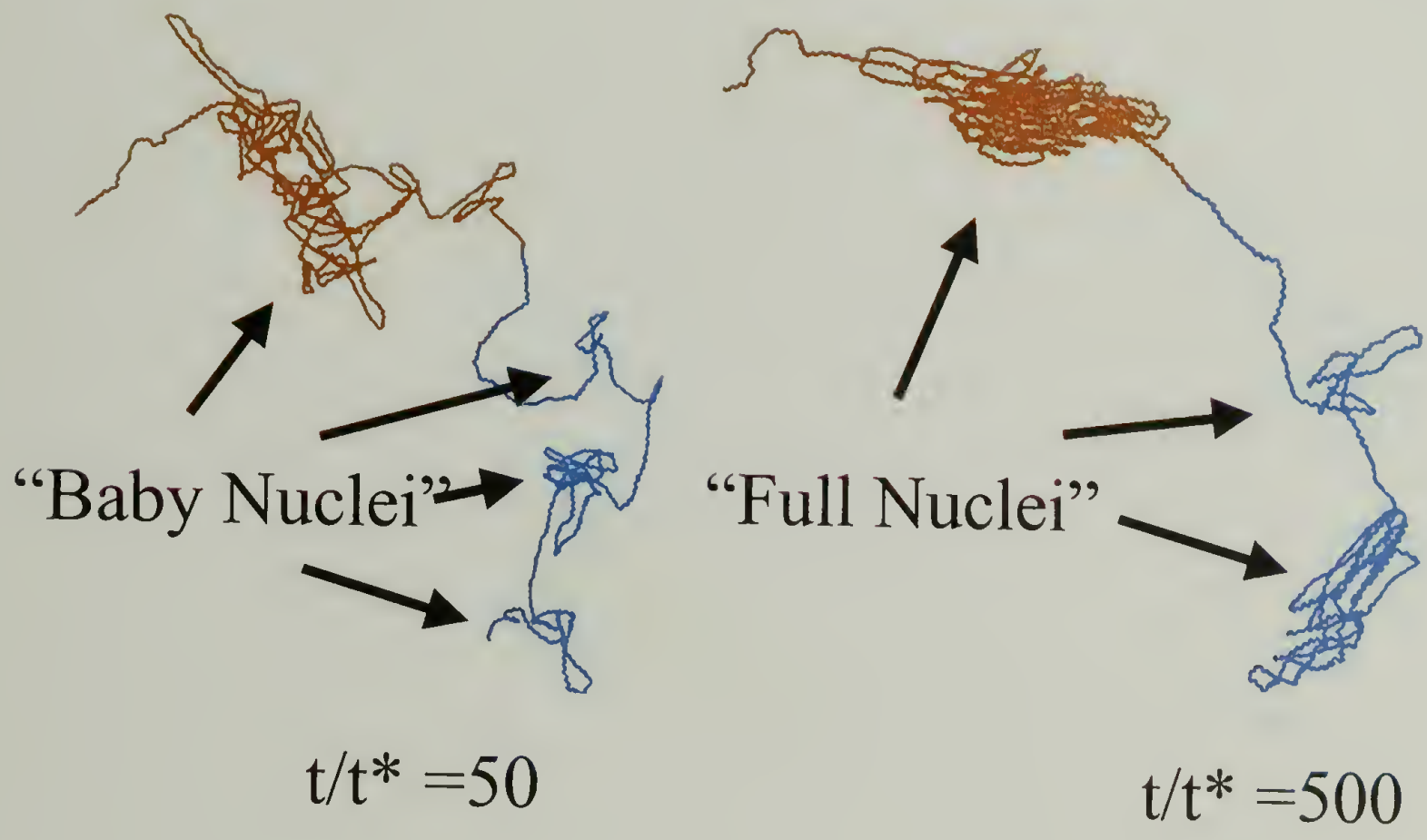

Figure 4.2: Typical chain conformational evolution in the early stages of crystallization. Snapshots for $N = 2000$ shown.

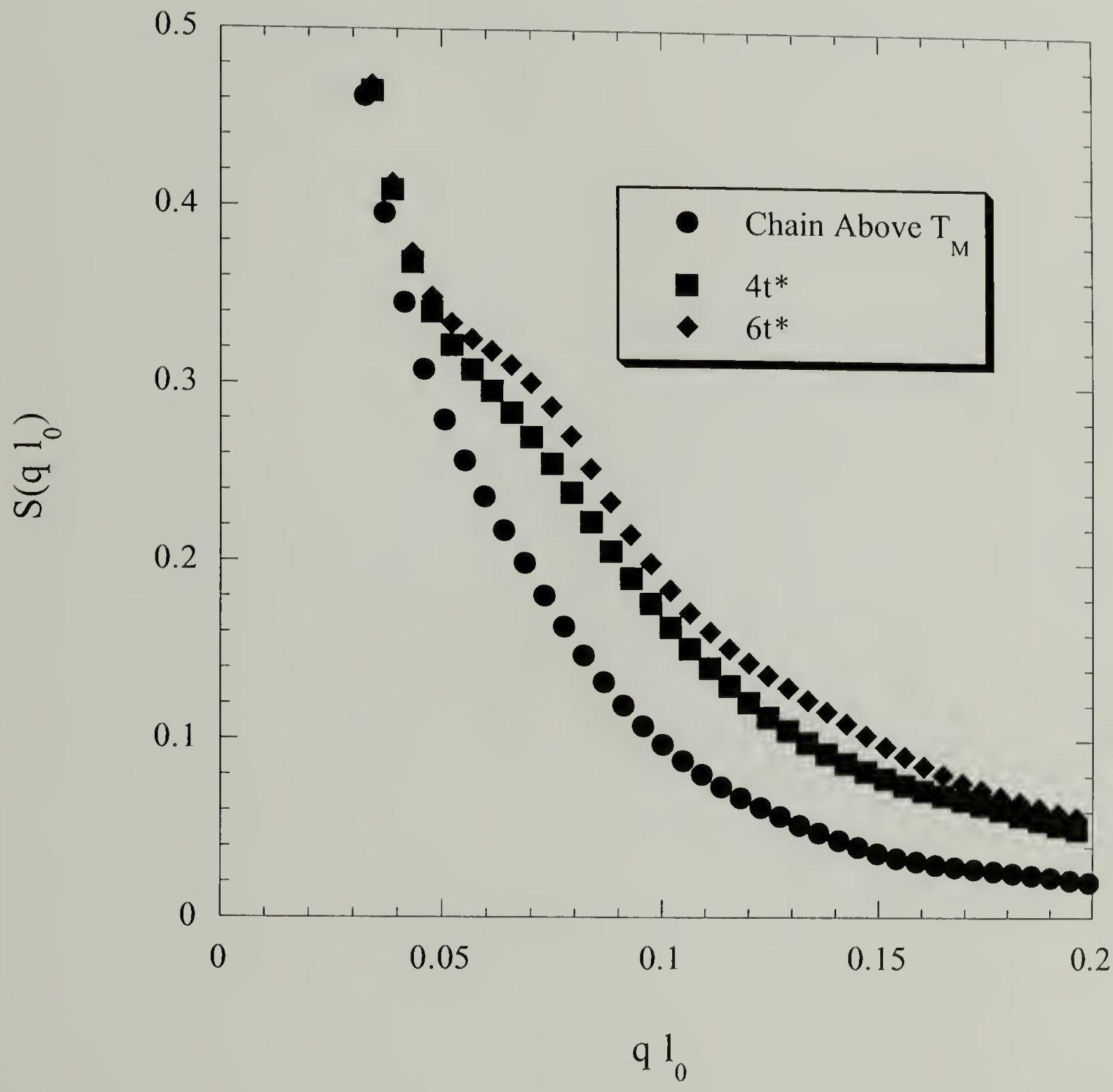

Figure 4.3: Peak in S(q).

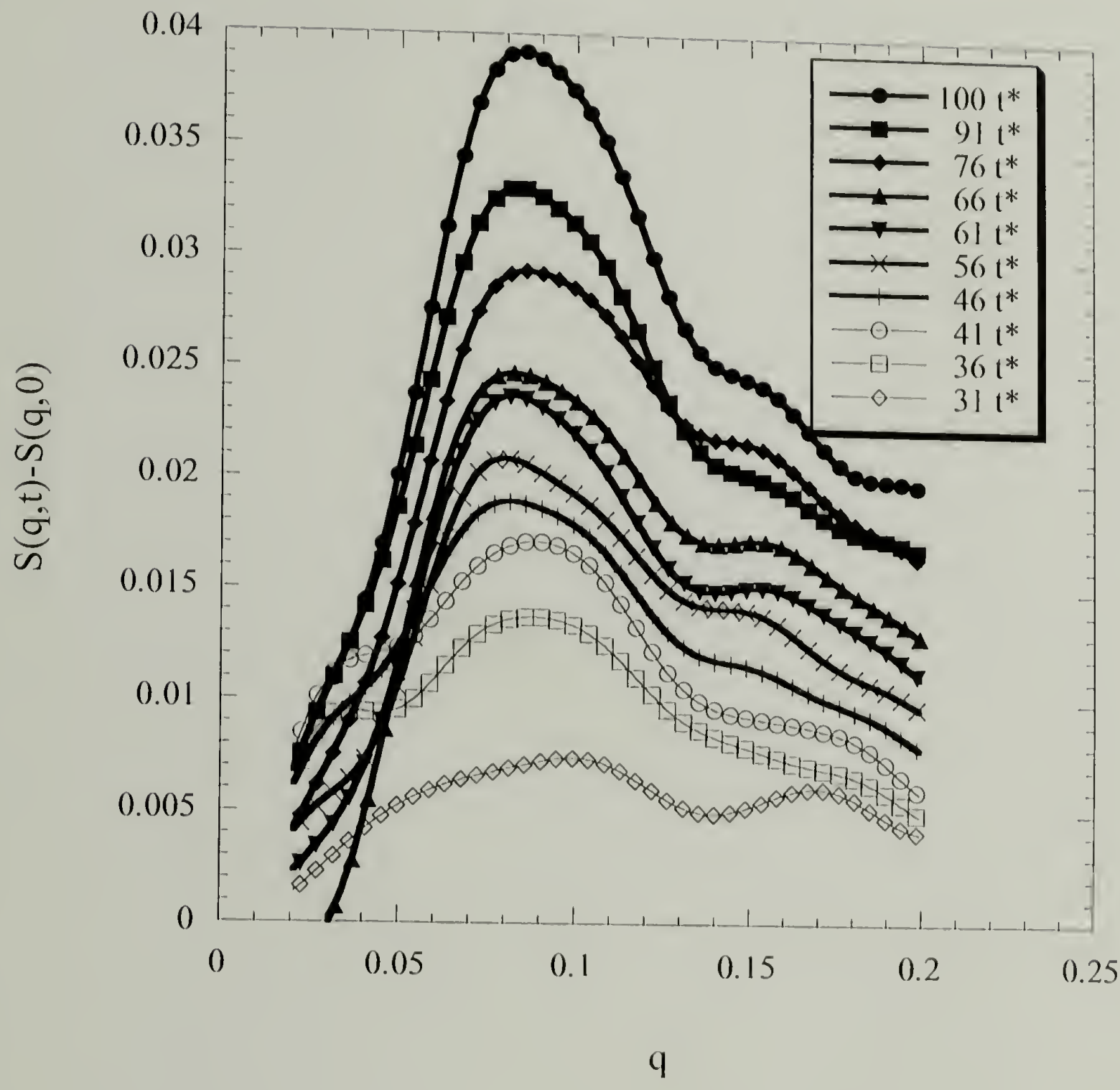

Figure 4.4: Typical scattering behavior in the early stages of crystallization. Data for $N = 2000$ shown.

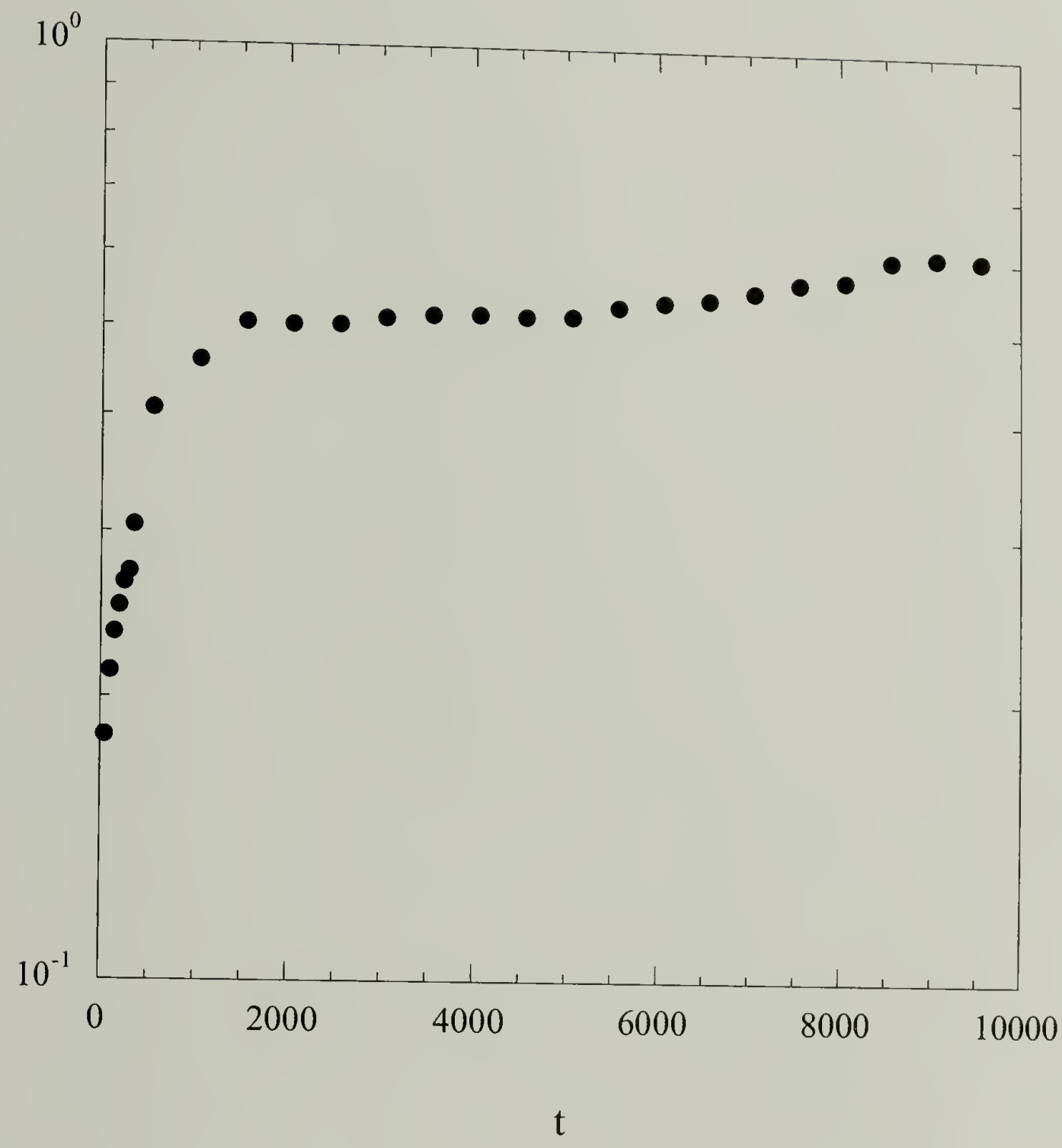

Figure 4.5: Total scattering intensity as a function of time. Data for $N = 2000$ shown.

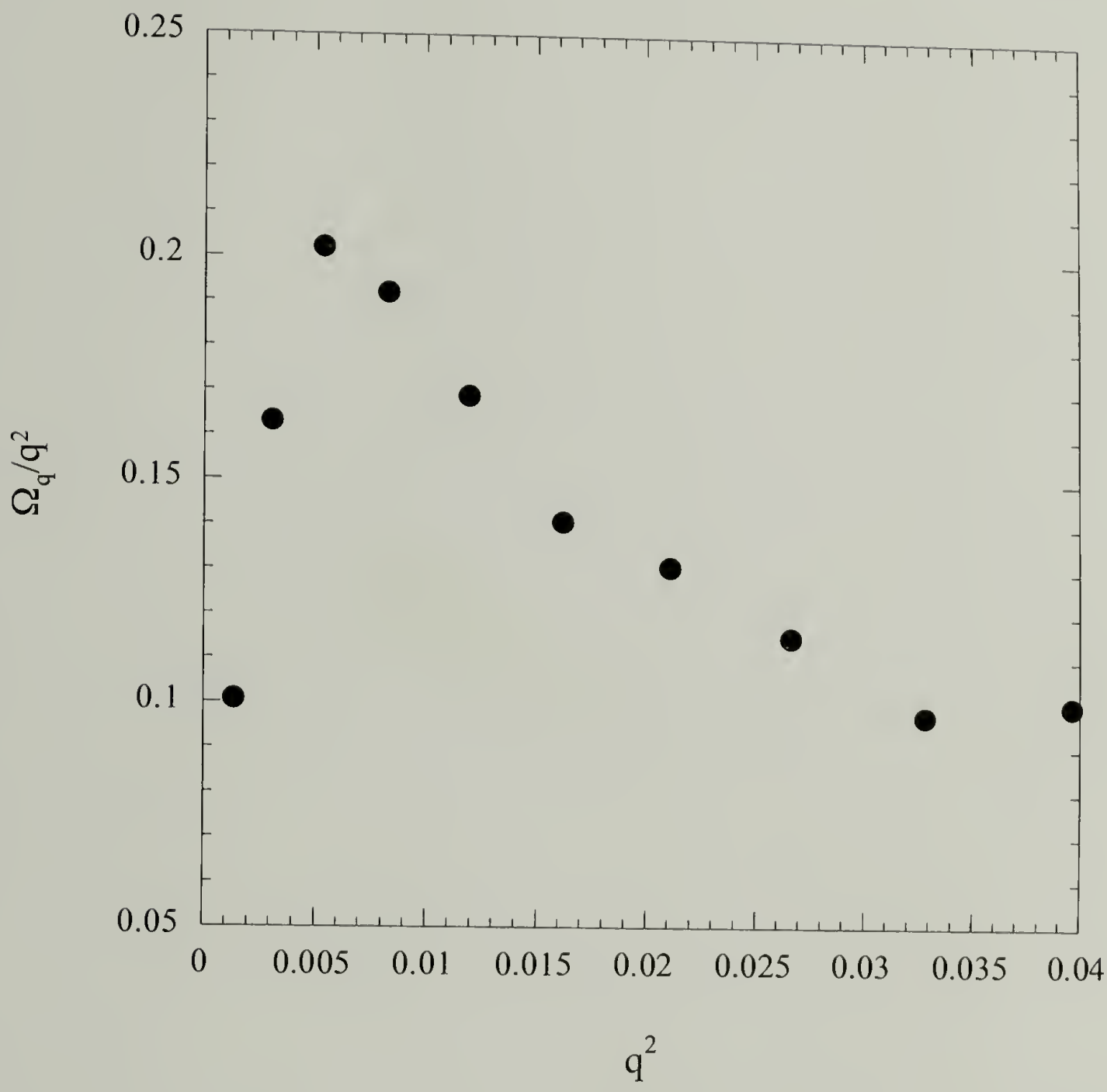

Figure 4.6: Fluctuation growth rates as a function of q^2. Data for $N = 2000$ shown.

Figure 4.7: Typical chain conformational evolution spanning time from the early stages to the terminal stages of crystallization. The homopolymer chain is partially shaded to illustrate movement of chain segments into the crystalline domains. Snapshots for $N = 2000$ shown.

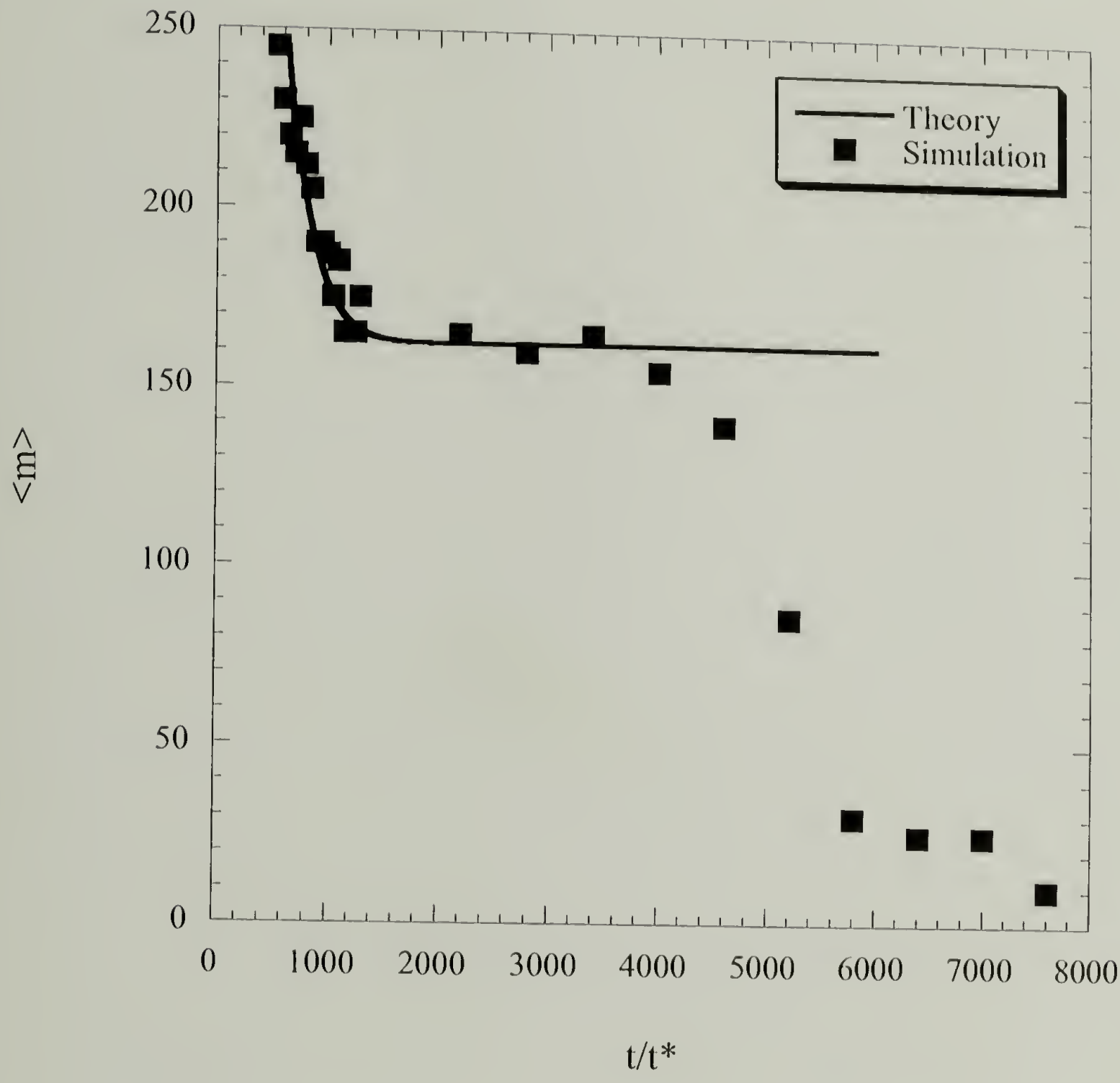

Figure 4.8: Number of chain segments between two crystal nuclei as a function of time. Points indicate simulation results. The line is calculated from via the Fokker-Plank equation.

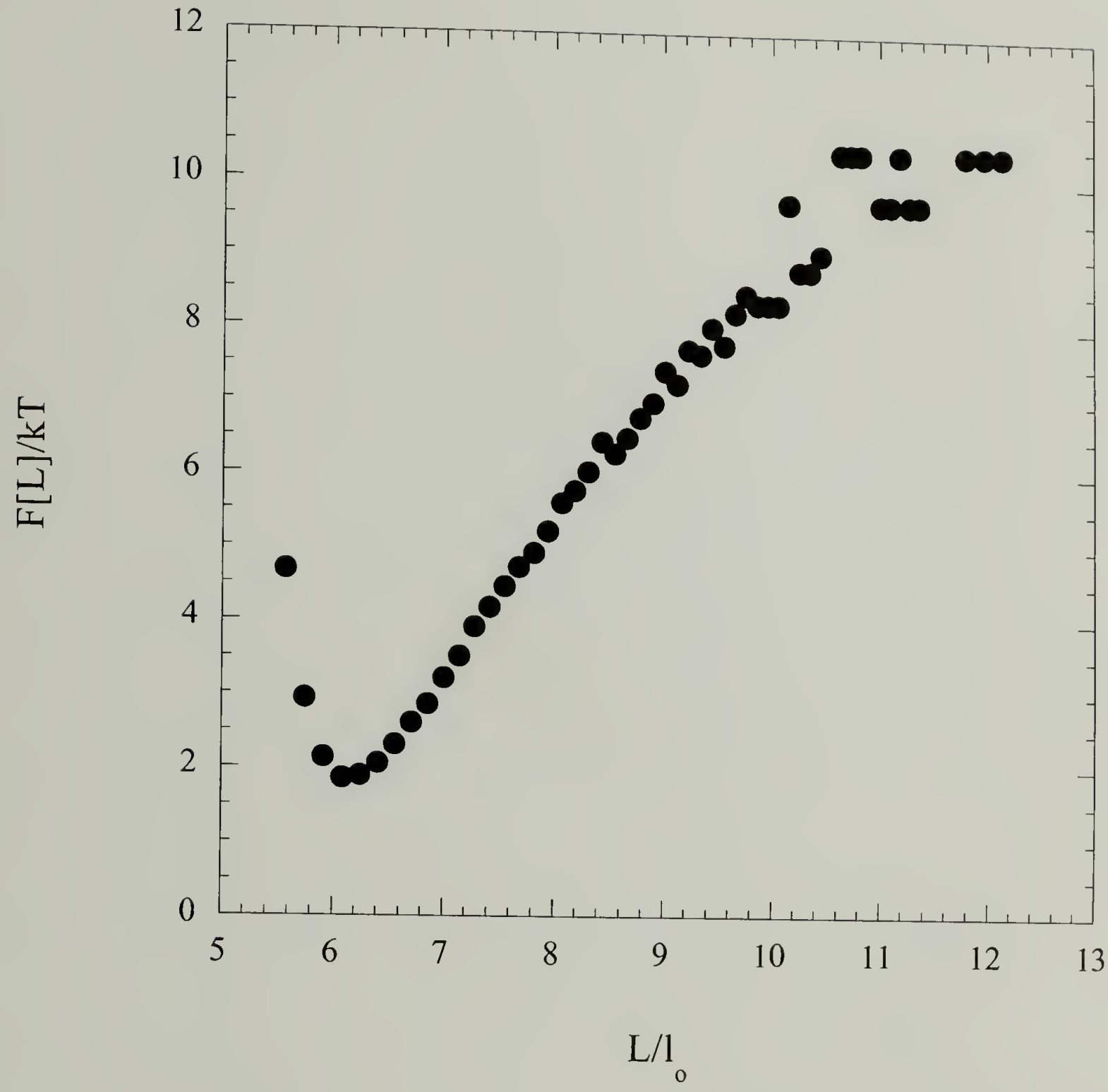

Figure 4.9: The free energy density as a function of L for $N = 2000$ without torsional constraints at $kT/\epsilon = 9.0$.

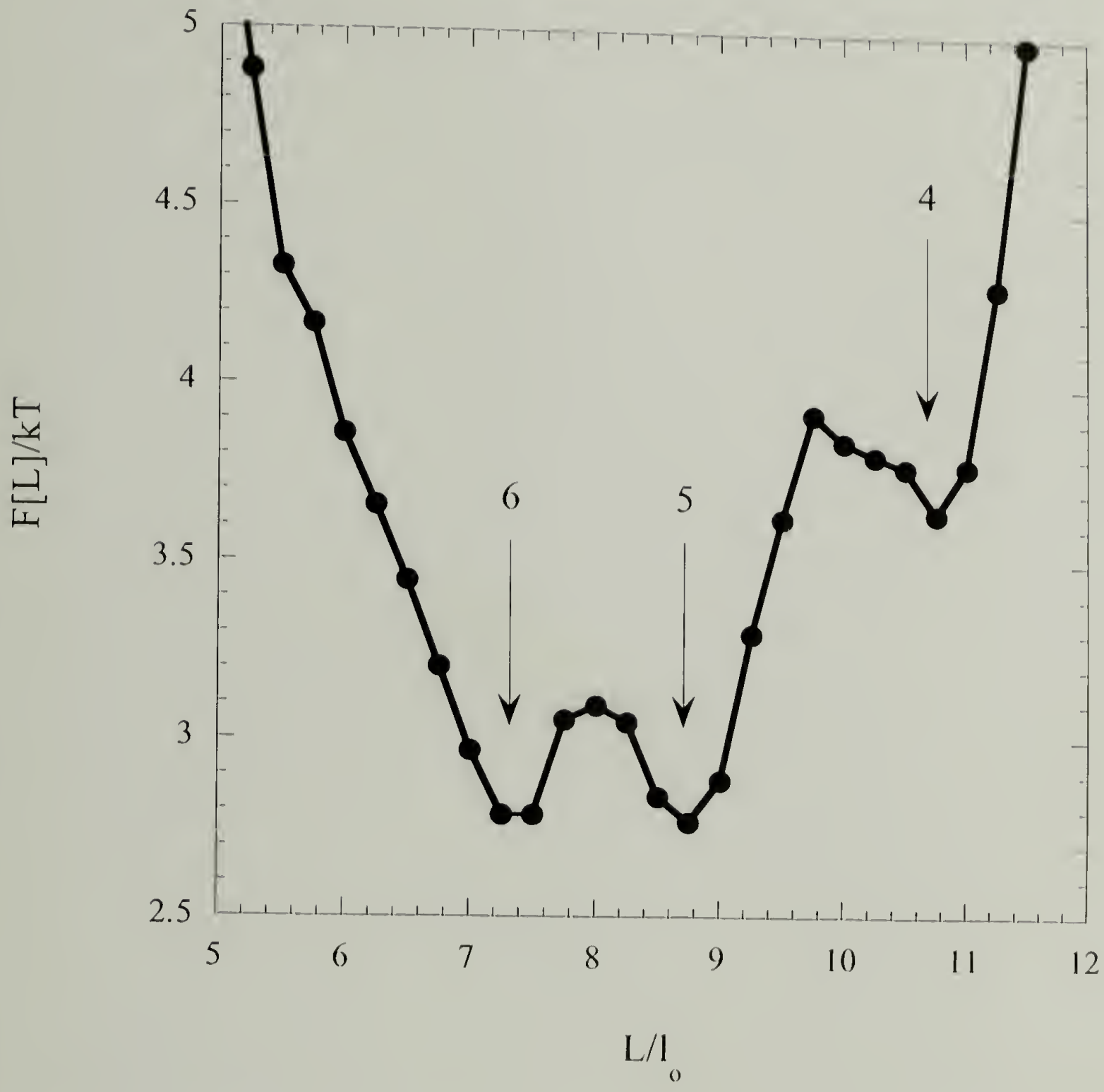

Figure 4.10: The free energy density as a function of L for $N = 200$ at $kT/\epsilon = 9.0$.

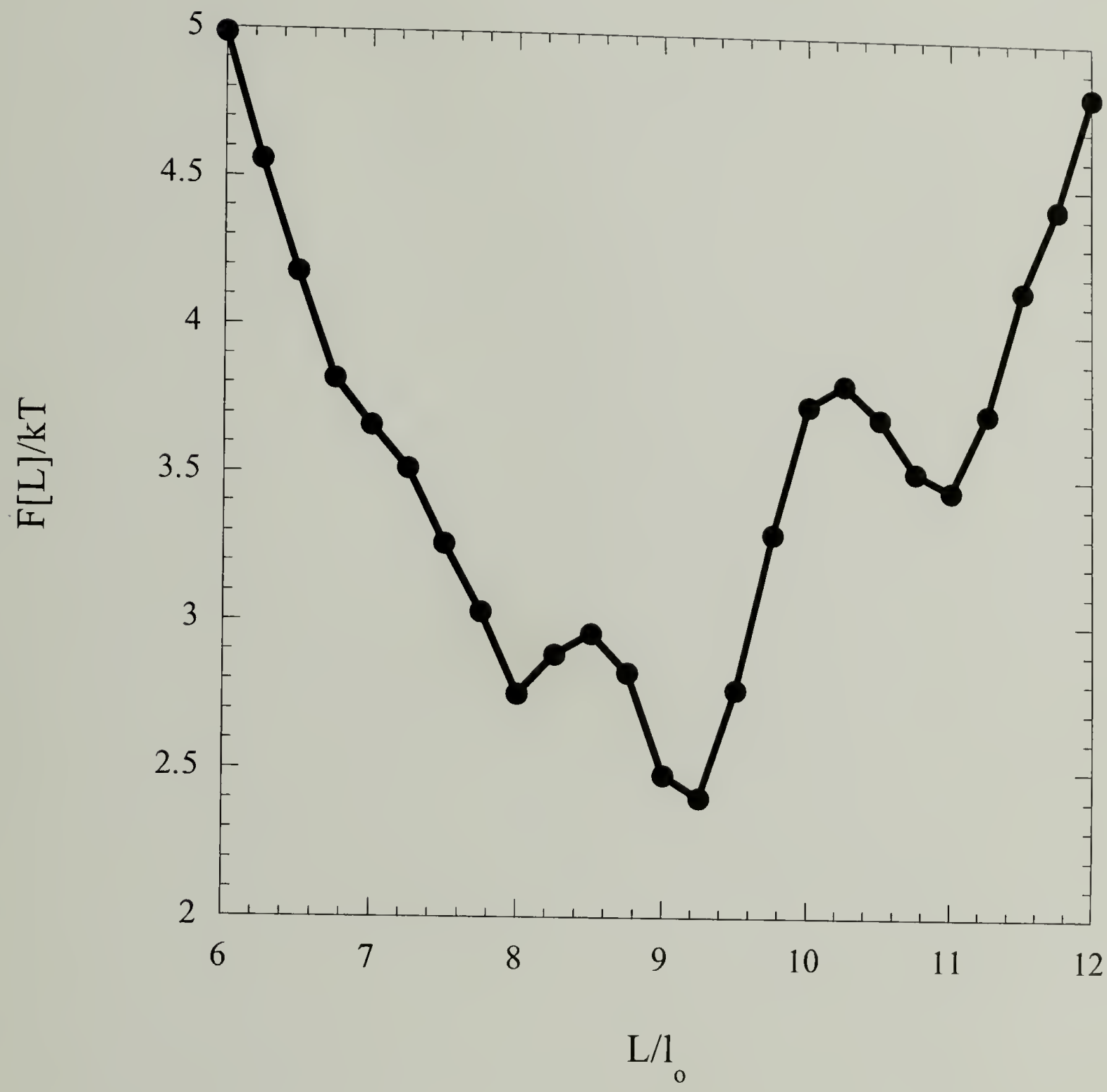

Figure 4.11: The free energy density as a function of L for $N = 250$ at $kT/\epsilon = 9.0$.

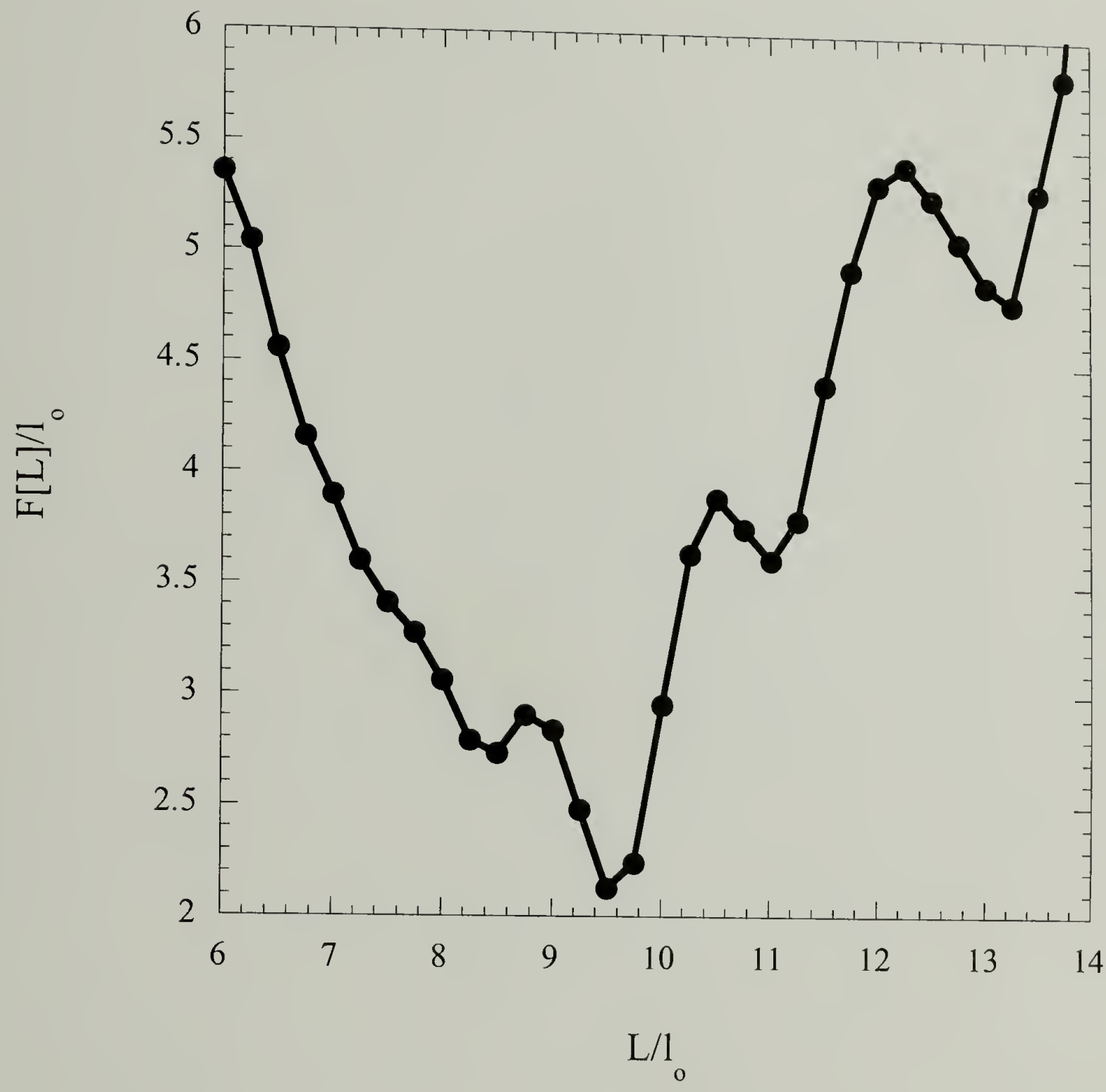

Figure 4.12: The free energy density as a function of L for $N = 300$ at $kT/\epsilon = 9.0$.

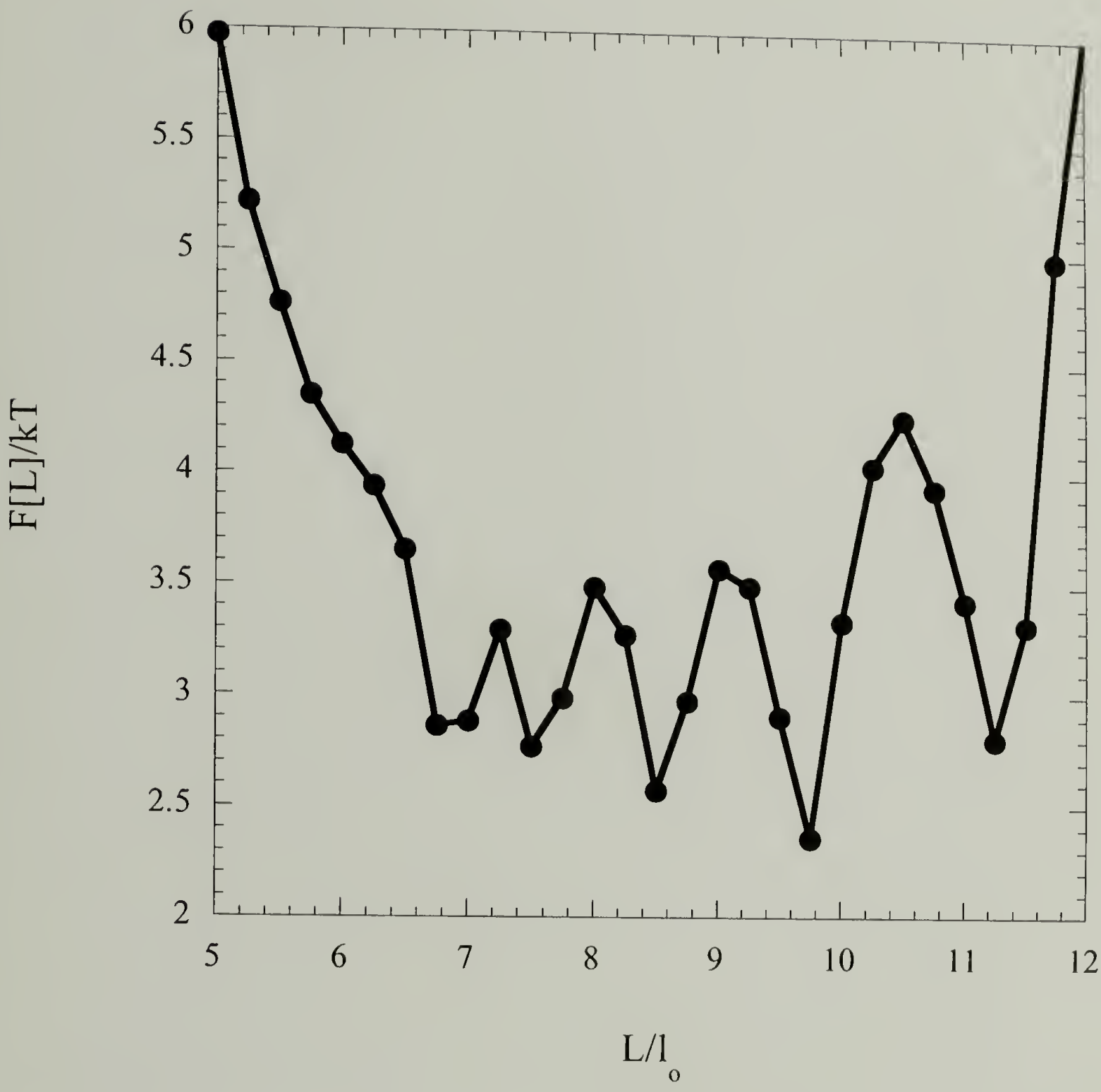

Figure 4.13: The free energy density as a function of L for $N = 300$ at $kT/\epsilon = 7.0$.

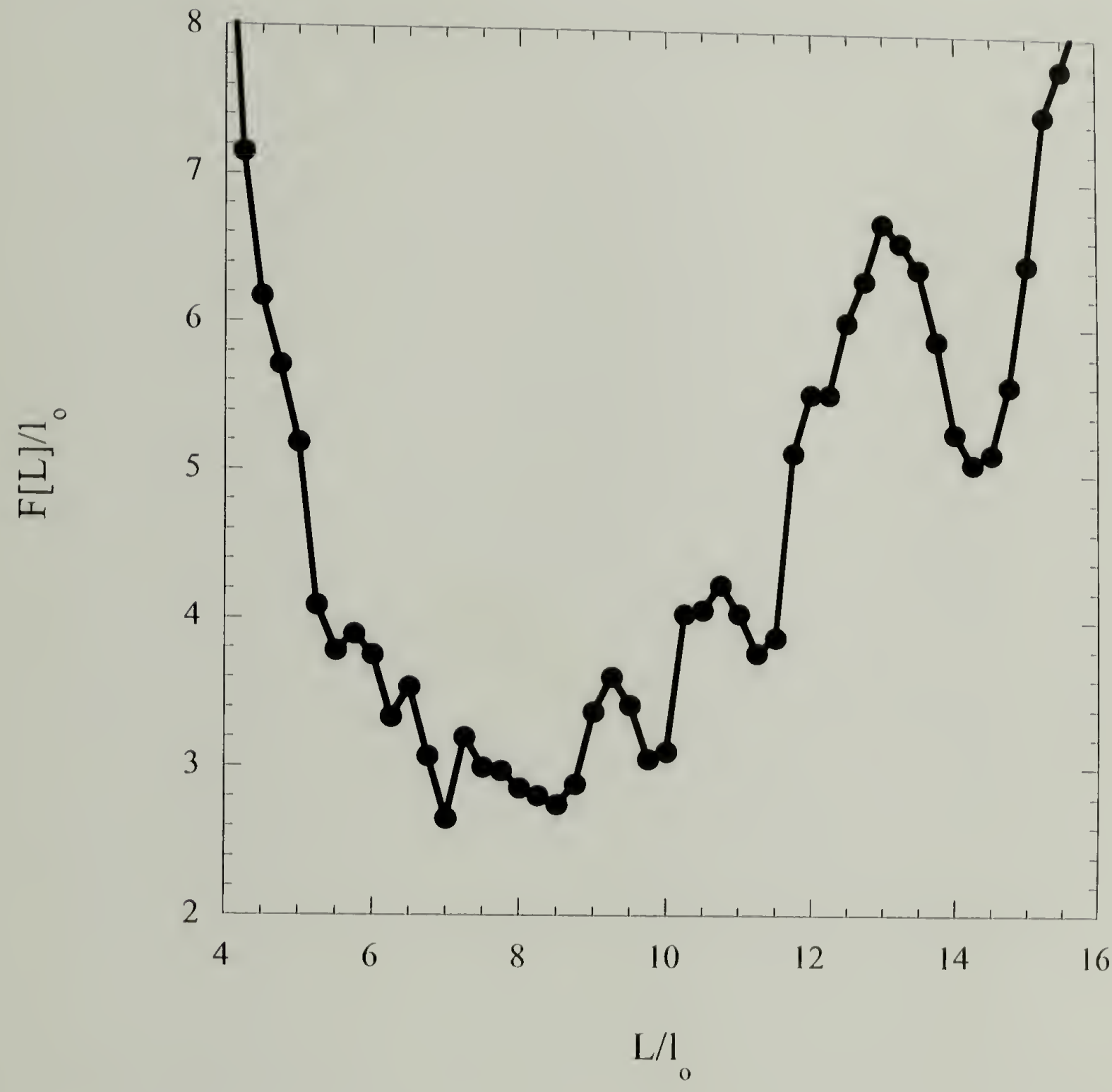

Figure 4.14: The free energy density as a function of L for $N = 300$ at $kT/\epsilon = 5.0$.

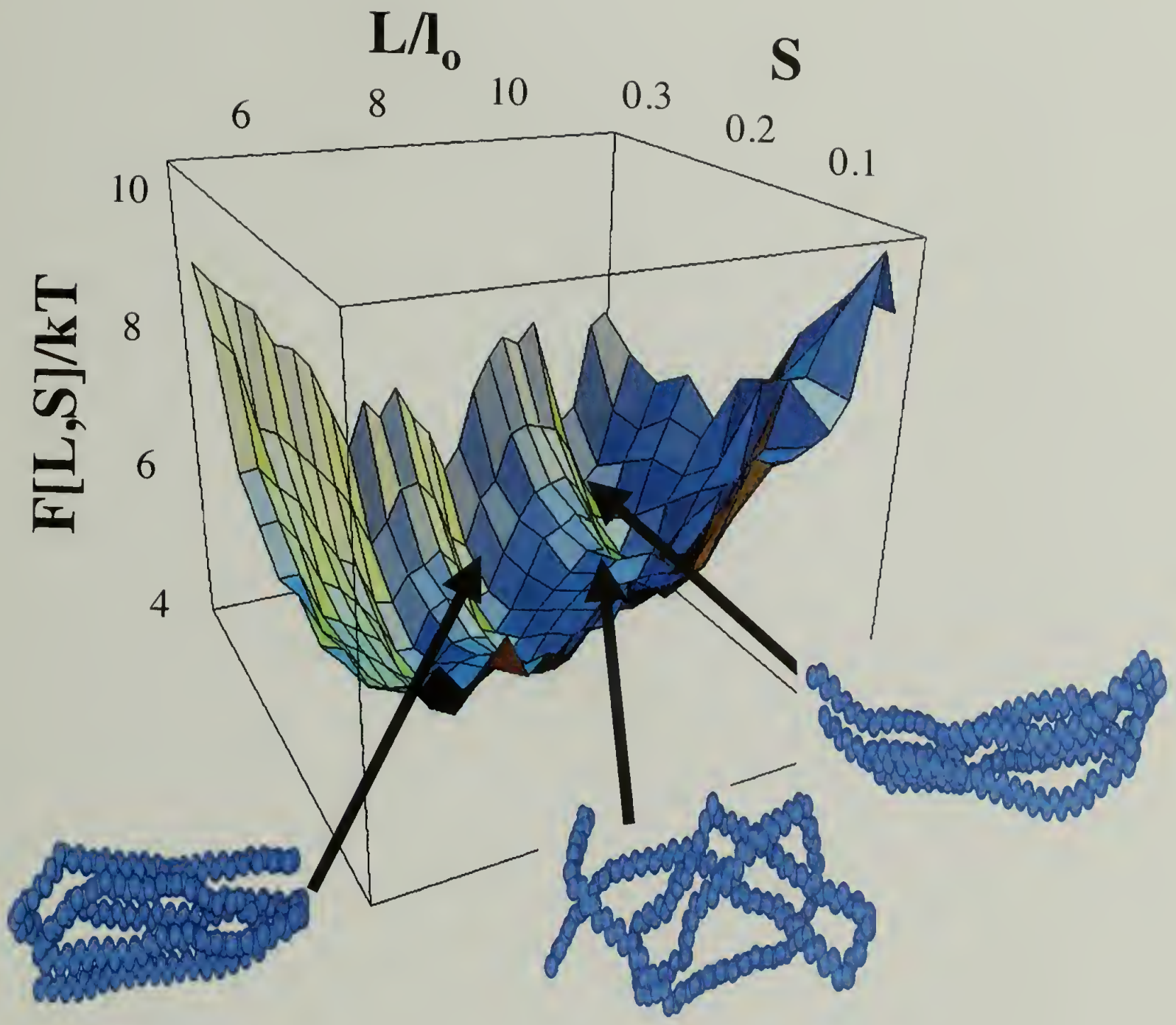

Figure 4.15: The free energy density as a function of both L and S for $N = 200$ at $kT/\epsilon = 9.0$. The snapshots indicate the ordered configurations typical of the wells and the disordered structures of the saddles.

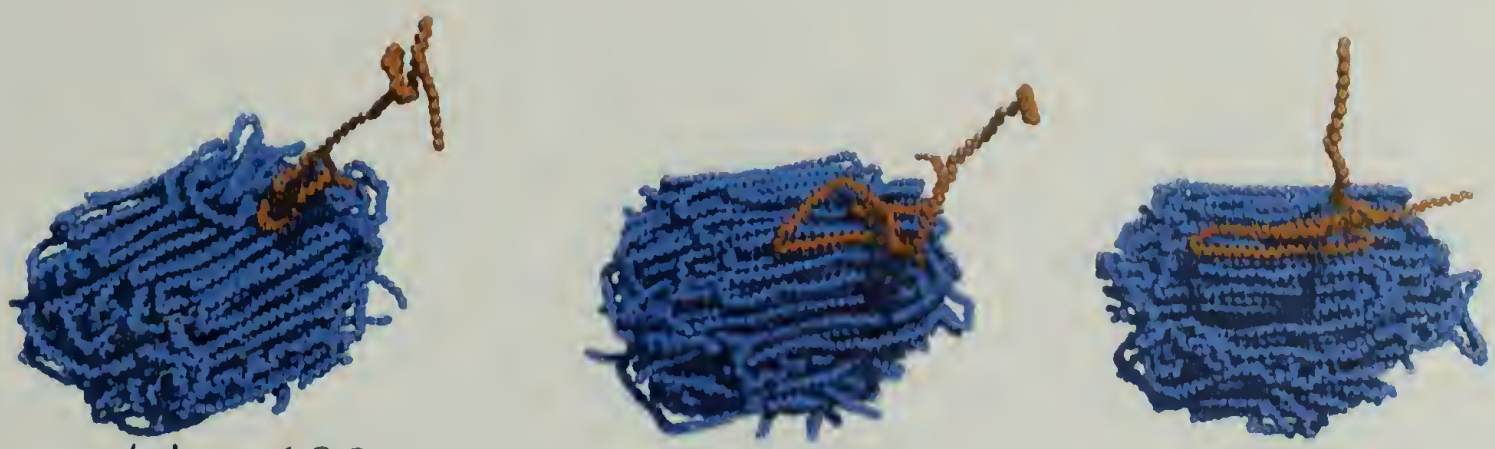

Figure 4.16: The 40^{th} chain adding to a 39 chain crystal at $\Delta T \approx 2.0$.

t/t* = 240 t/t* = 640 t/t* = 1340

Figure 4.17: The 22^{nd} chain adding to a 21 chain crystal at $\Delta T \approx 4.0$.

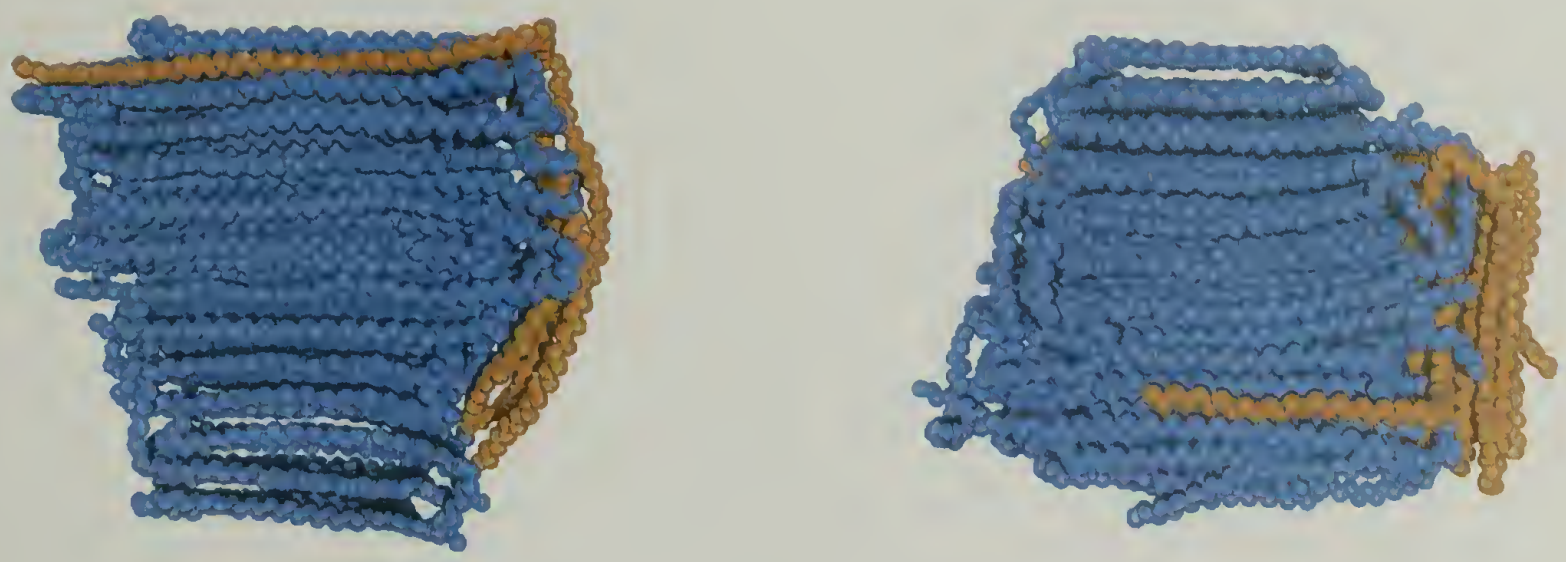

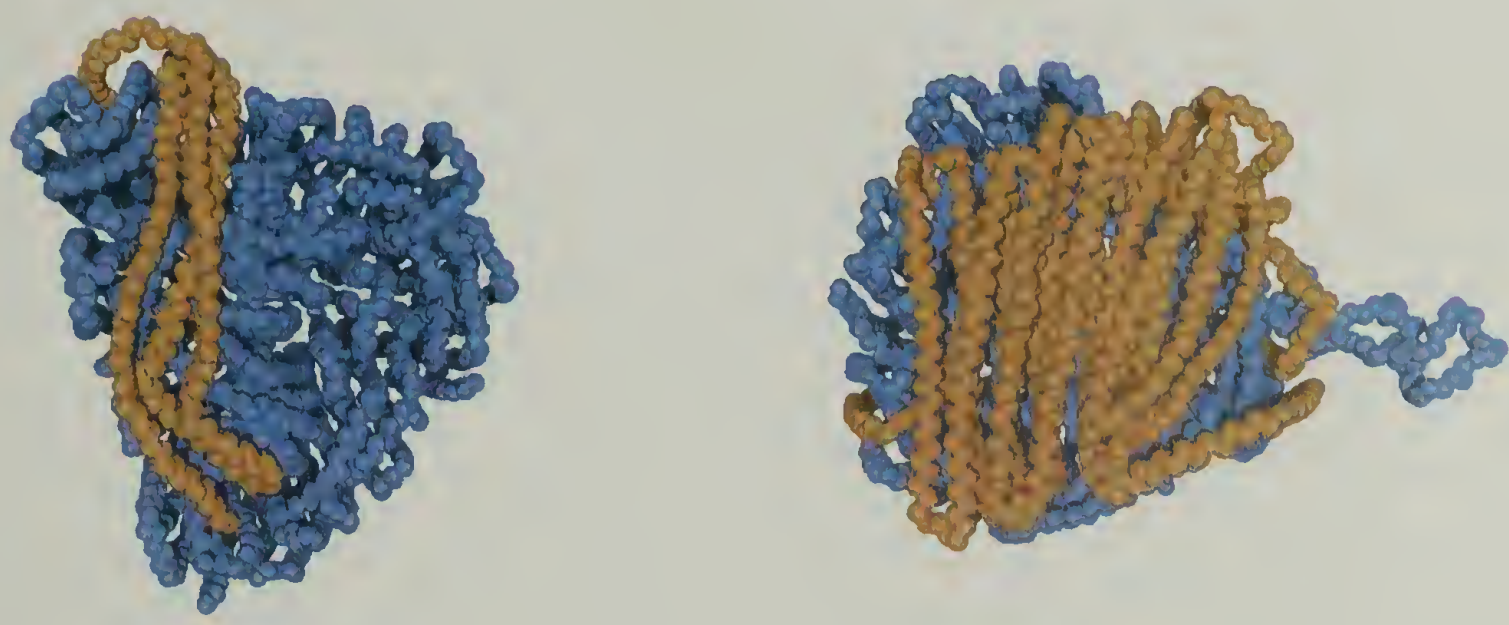

Figure 4.18: The misregistry of the 25^{th} chain leads to further growth at the fold surface by chain 30 for a crystal grown at $\Delta T \approx 4.0$.

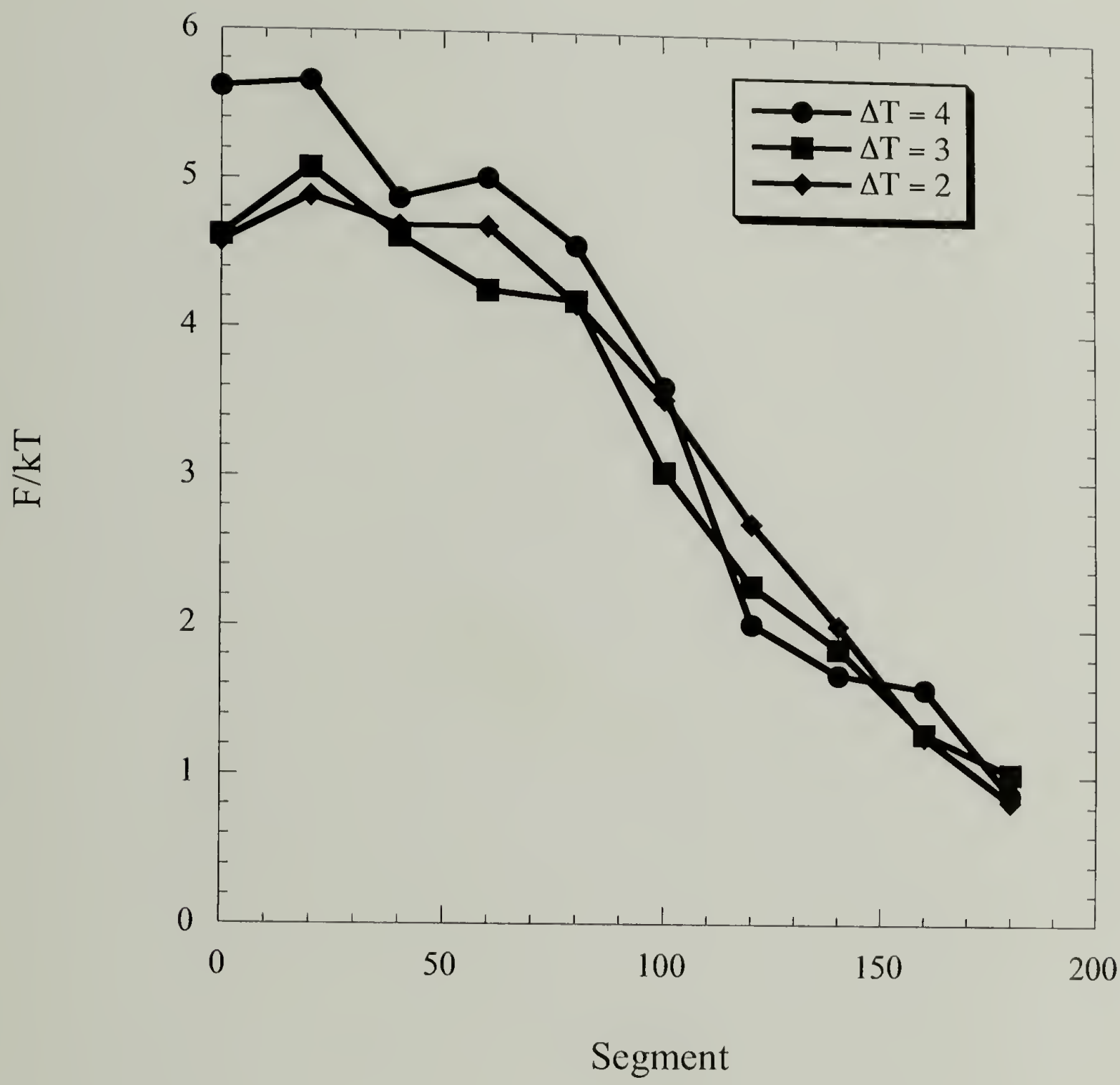

Figure 4.19: Estimate of the free energy for adding new chain segments to the growth face.

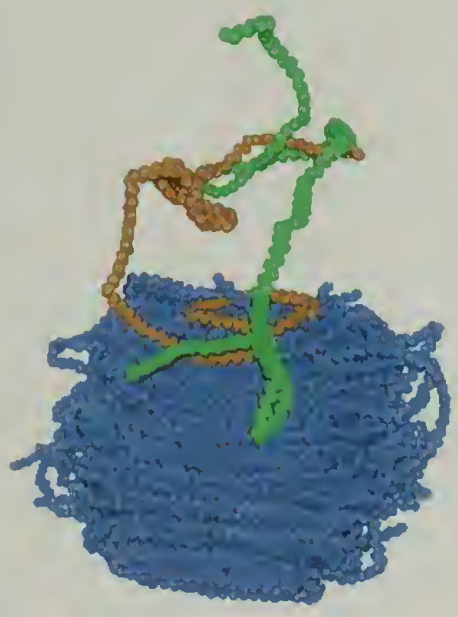

t/t* = 50

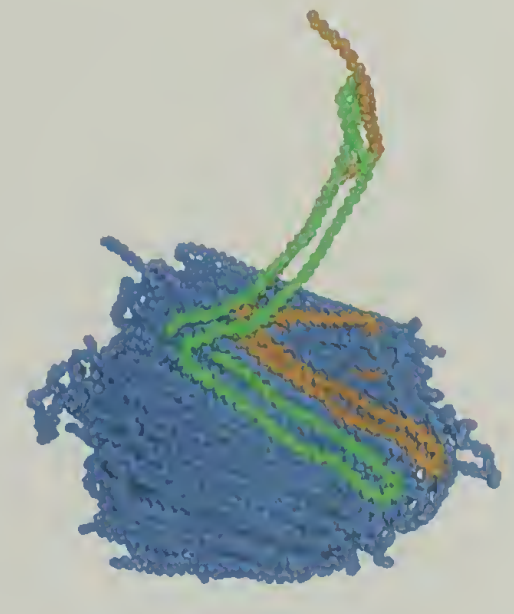

t/t* = 750

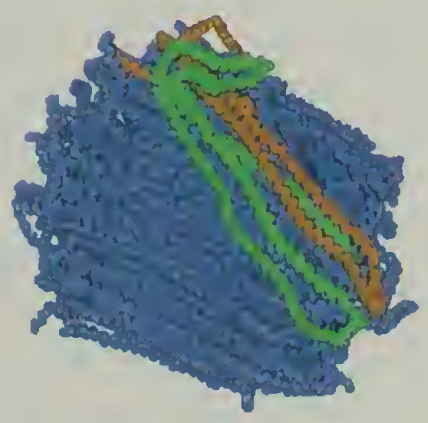

t/t* = 1450

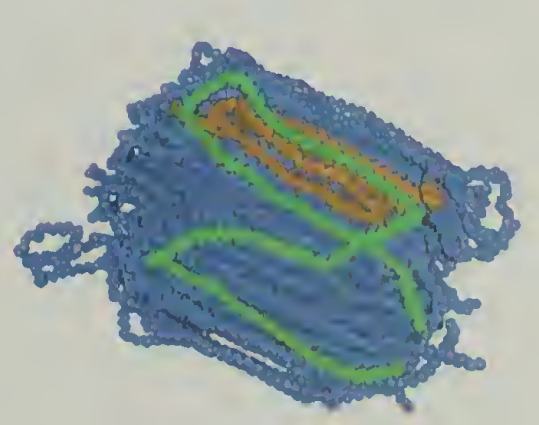

t/t* = 4850

Figure 4.20: Representative snapshots from the simulation of two chains simultaneously adding to the growth front at $\Delta T \approx 2.0$.

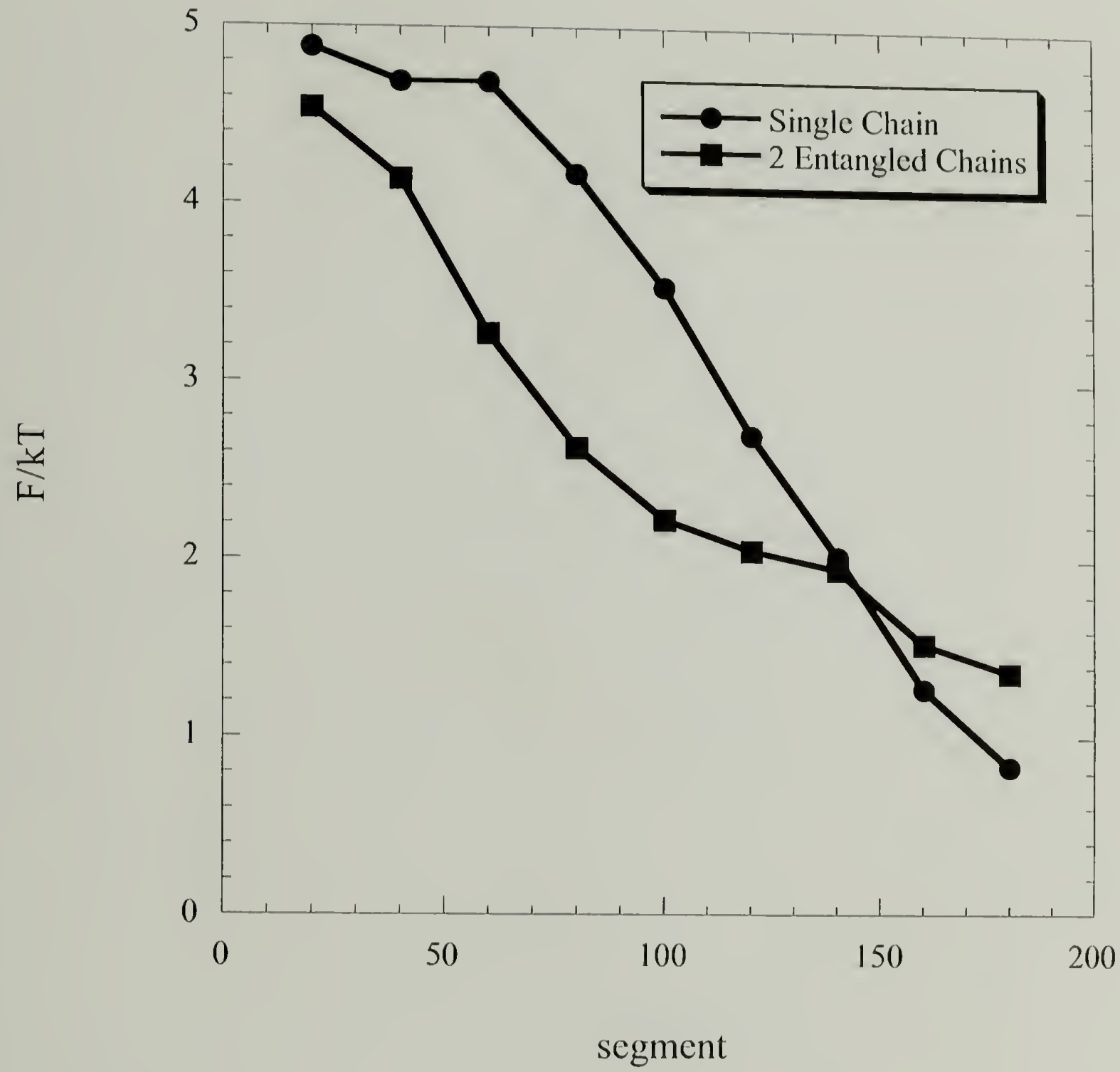

Figure 4.21: Estimate of the free energy for adding new chain segments to the growth face when two chains are adding simultaneously.

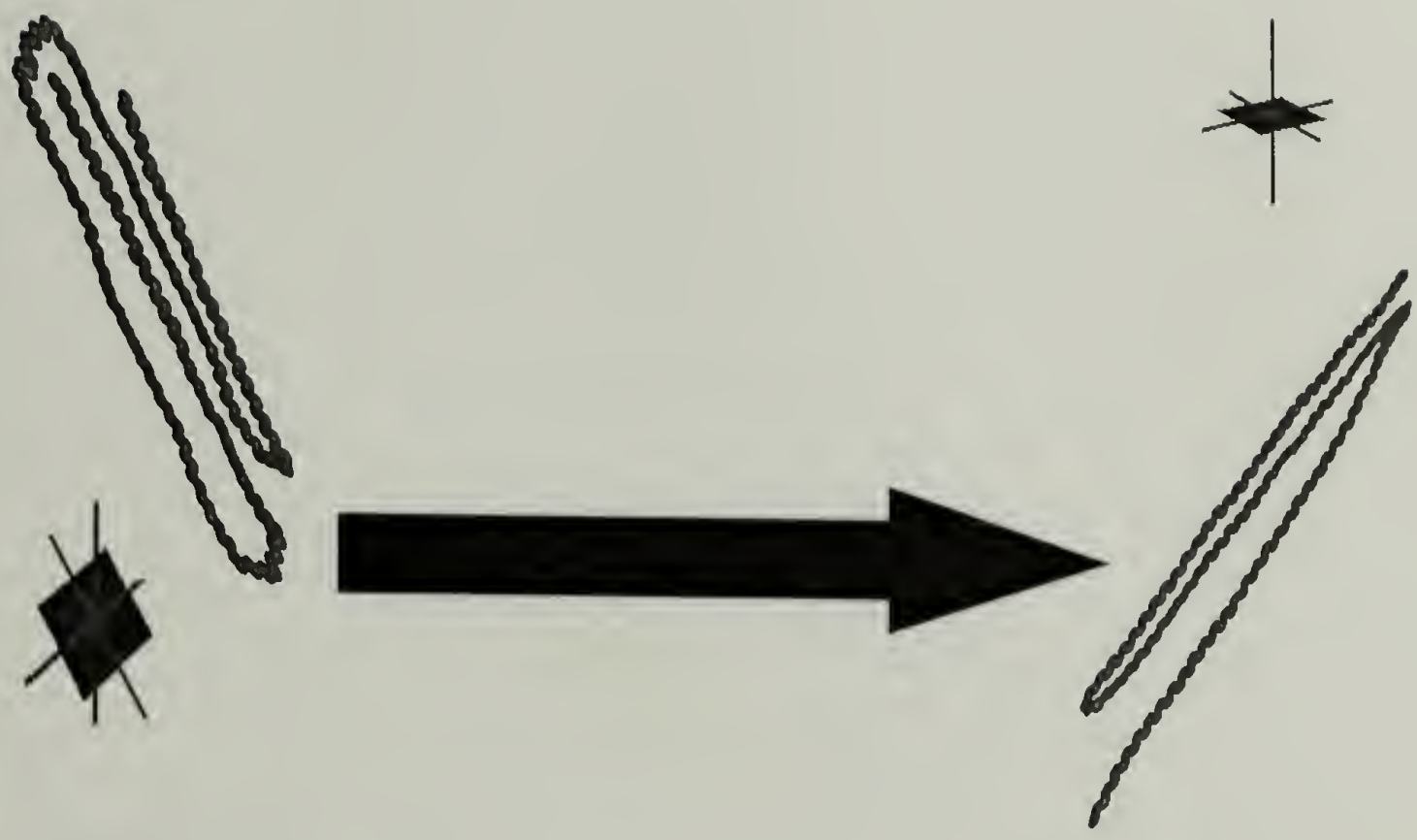

Figure 4.22: Snapshots of the first chain in the midst of other chains at different stages of crystal growth at $\Delta T' \approx 2.0$.

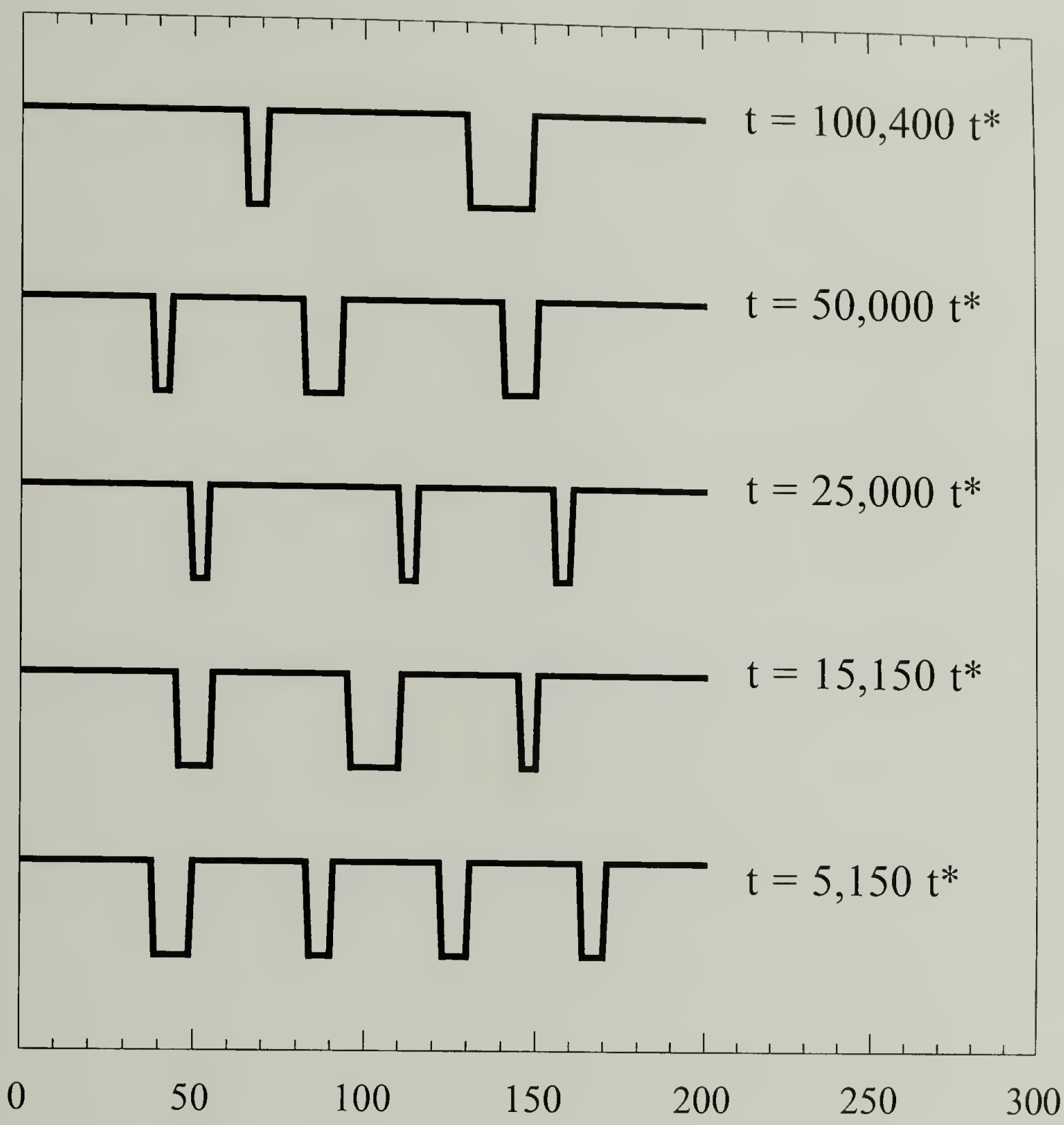

Figure 4.23: Phase map for the location of the first chain's segments at different times at $\Delta T \approx 2.0$. The wells correspond to the fold surface. The remainder of the curves represent the crystal regions.

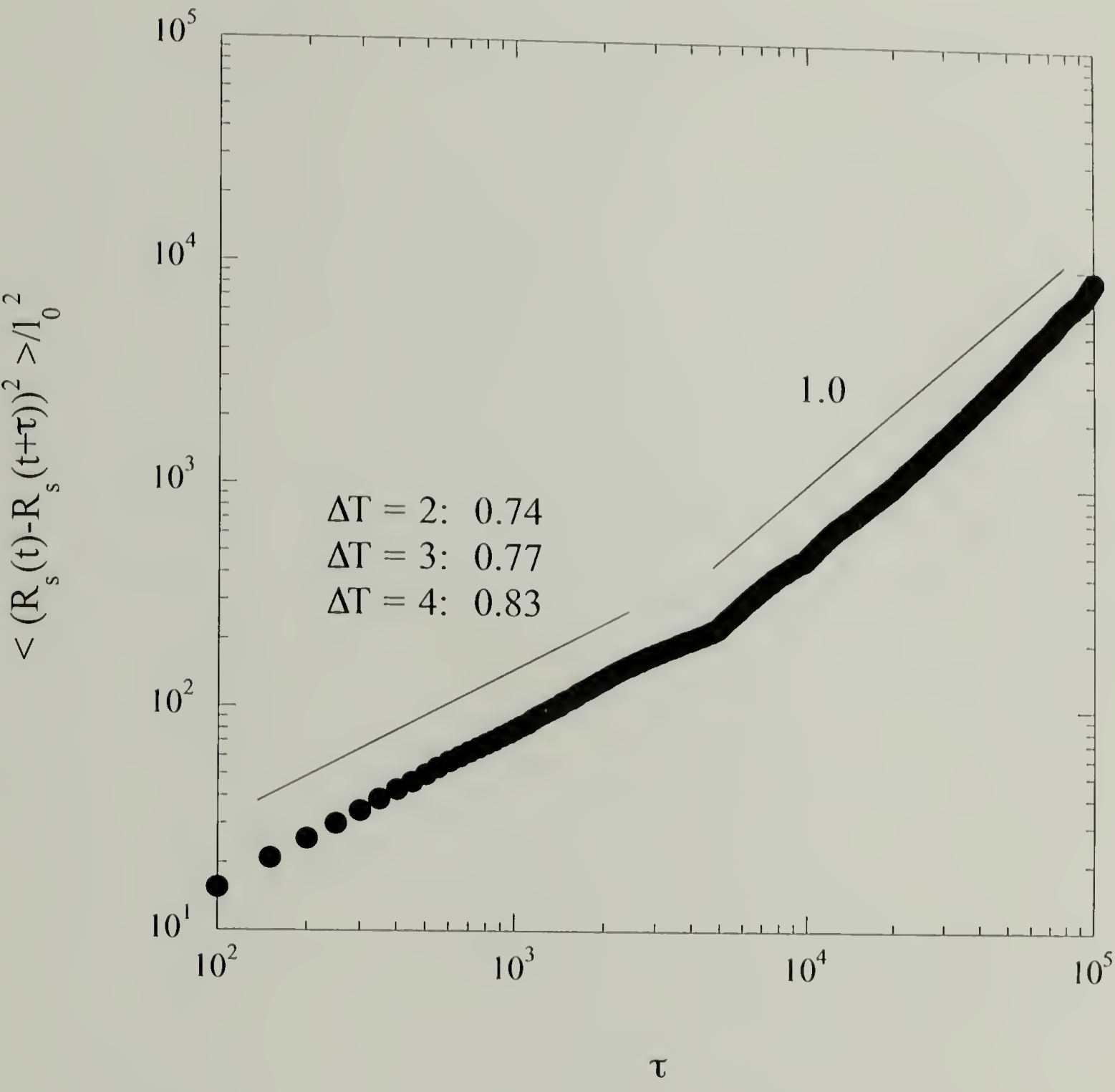

Figure 4.24: The squared displacement in time for a tagged chain segment. Data shown for segment 60 of the first chain in a crystal grown at $\Delta T \approx 2.0$.

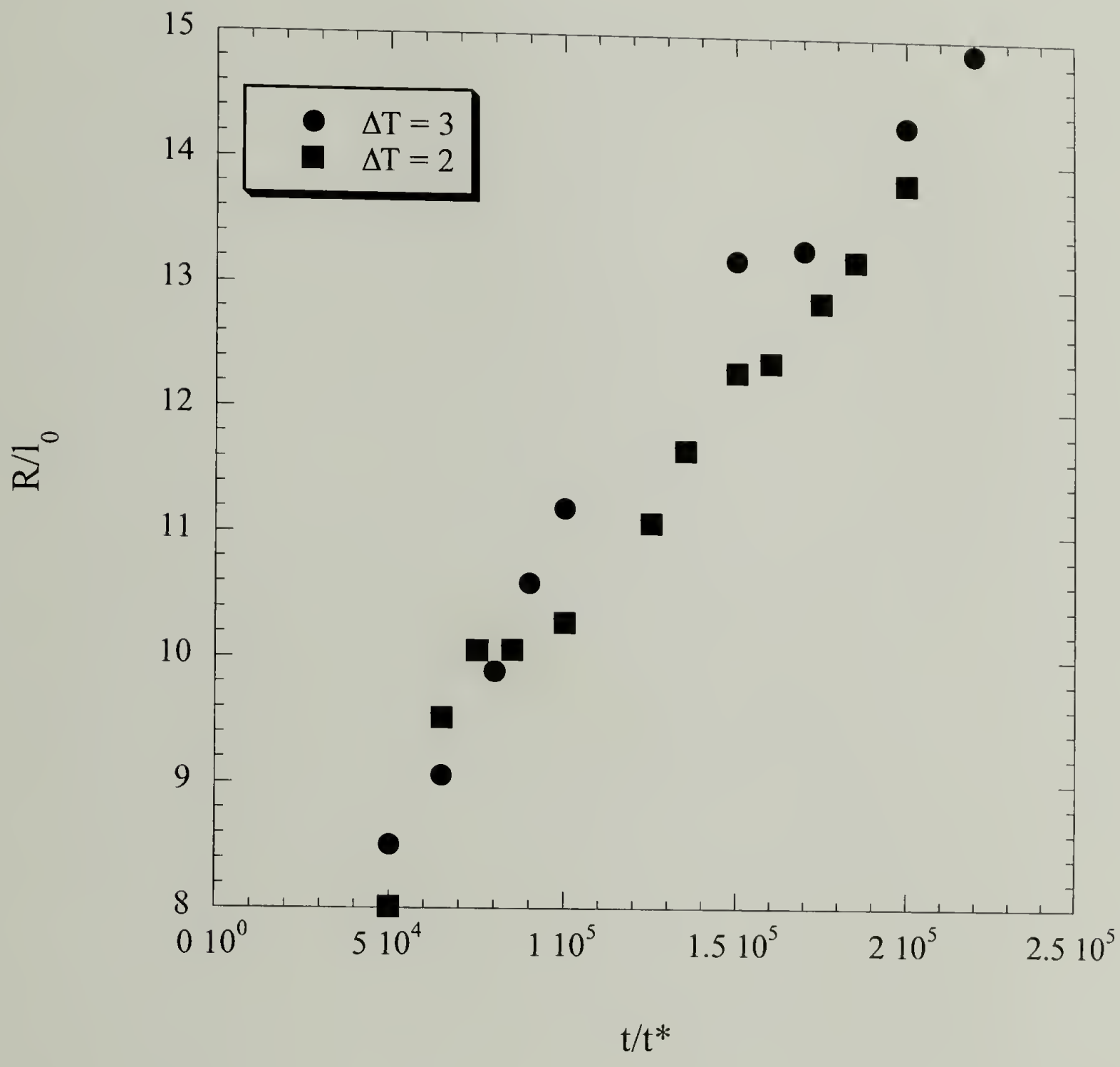

Figure 4.25: The radius of gyration perpendicular to the growth face as a function of time.

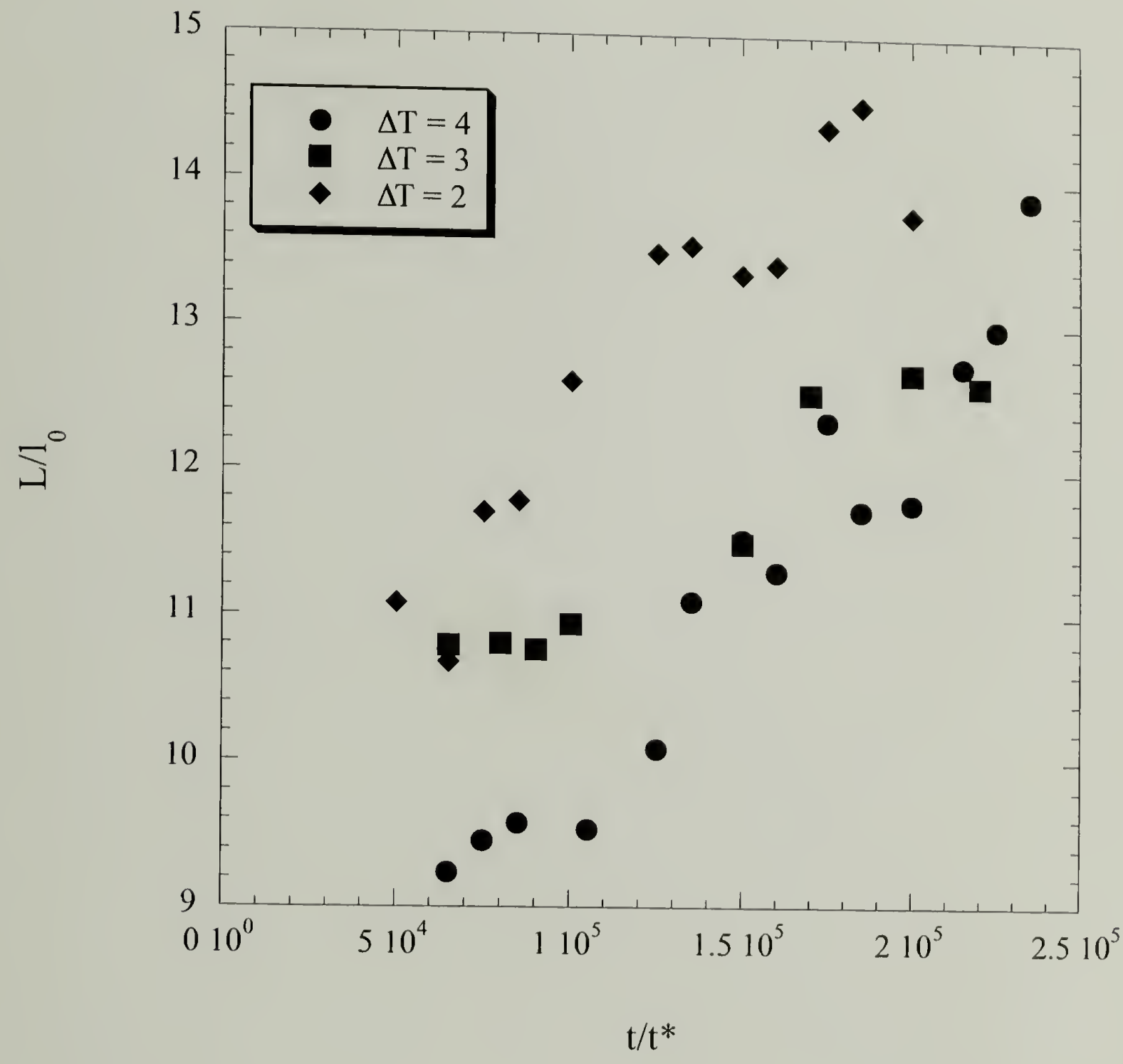

Figure 4.26: The radius of gyration parallel to the growth face as a function of time.

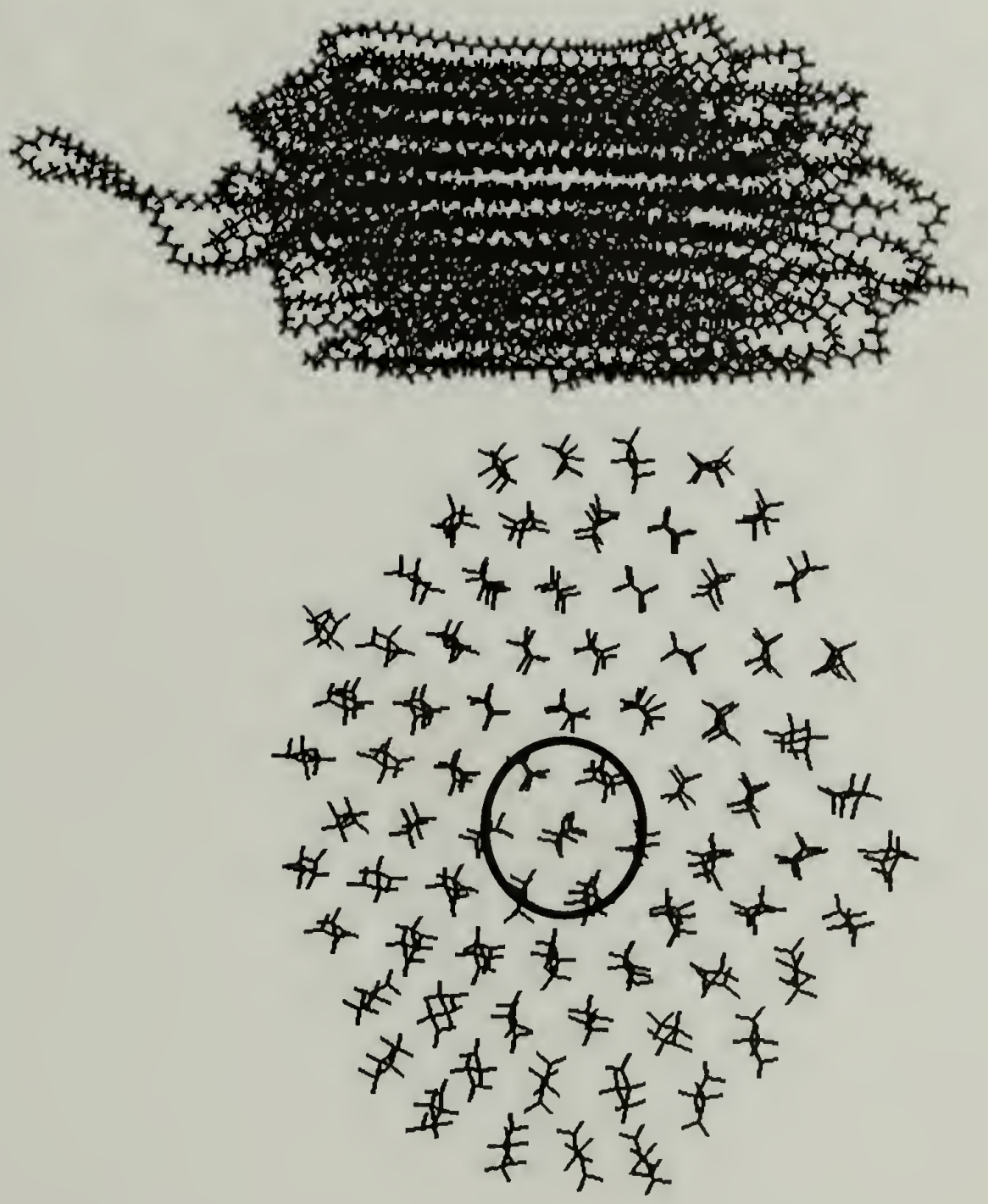

Figure 4.27: On the bottom is a cross section of the 20 chain polyethylene crystal shown on the top. Each chain is 200 methylene units long.

CHAPTER 5

SINGLE MOLECULE FORCE SPECTROSCOPY

5.1 Introduction

The physical response of single polymer molecules to applied forces impacts many processes of both biological and synthetic significance, spanning a range of phenomena as broad as DNA transcription to macroscopic rubber elasticity. Recently, great strides have been made in examining these forces with the development of several tools capable of probing these responses in a direct fashion. These techniques include atomic force microscopy (AFM), optical tweezers, micropipet/glass bead displacement, and magnetic vices.[112] These experimental advances offer both new insight into the processes studied and new challenges to provide more accurate theoretical descriptions. Computer modeling may prove an excellent tool for bridging the gap between existing mathematical treatments and the wealth of new data from the experimental studies. [113–126]

Toward this end, the goal of this chapter is to develop a suitable computational method for predicting the force response of individual chains while examining a fundamentally interesting system. Specifically, we consider the simplest case of a non-charged flexible chain tethered to an athermal substrate. The freely jointed chain model may be expected to describe the retractive force exerted by the chain in this system when it is pulled by one end. The recent results of Kamiti[113],

Jensenius[114], Kikuchi[115], Ortiz[116], and their coworkers on neutral polymers that seem to yield behavior corresponding to this model further motivates a computational affirmation of their results, free of any experimental difficulties.

Section 5.2 describes the details of our model and numerical algorithm which consists of a Brownian dynamics simulation of a Lennard-Jones chain attached at one end to a hard-wall and at the other to a retracting phantom spring. In Section 5.3 we show that our computational approach yields good agreement with the observations of Ortiz and the theoretical expectations of the freely jointed chain model. We also demonstrate that the recent technique for elucidating the free energy of a molecular construction based upon these dynamic experiments can be applied to polymeric systems, as well. Finally, in Section 5.4, we suggest future elaborations to our methodology that may yield insight into the wide array of problems that are currently the focus of experimental studies.

5.2 Model and Simulation Technique

5.2.1 Model

The experimental system considered here consists of three elements. It contains a neutral polymer in a good solvent. The polymer is tethered at one end to a retracting cantilever, such as an AFM probe, and an athermal substrate covalently tethers the other end of the chain. The model employed in this study must therefore include sufficient details to capture the characteristics of the polymers, the coupled cantilever probe, and the binding surface upon which the polymers are supported. In our simulations, a united atom, bead-spring model represents the polymers while

a retracting phantom spring attached to one end of the polymer represents the cantilever. The substrate is modeled as a hard-wall in the x-y plane.

The bead-spring model includes bonded and non-bonded intra-molecular forces acting on each of the N beads that compose the chain. The Lennard-Jones potential, U_{LJ}, describes the pairwise interactions due to van der Waals attractions and hard-core repulsions . U_{LJ} has the form

$$\frac{U_{LJ}}{k_BT} = \frac{\epsilon}{k_BT}\left[(\sigma/r)^{12} - 2\,(\sigma/r)^{6}\right] \tag{5.1}$$

where r is the distance between the two beads. ϵ and σ are the strength and range parameters, respectively. The bonds were modeled by a simple harmonic potential

$$\frac{U_b}{k_BT} = \frac{k_b}{k_BT}\,(l - l_0)^2 \tag{5.2}$$

where l is the bond length, l_0 is the equilibrium bond length, and k_b is the spring constant.

The substrate always interacts with the beads via a hard-wall potential, reversing the momentum of any bead whose z coordinate falls below $\sigma/2$. The covalent bonds between the chains and substrate are modeled by immobilizing one terminal bead of the polymer at $z = \sigma/2$.

Finally, the cantilever's phantom spring obeys the harmonic potential described above, replacing k_b and l_0 with k_p and l_p, respectively. One end of the spring is connected to a terminal bead of the polymer while the other is attached to a point moving with a constant velocity, $\frac{\vec{dz}}{dt}$, as described below. Figure 5.1 illustrates this model.

Chains with values of N spanning 10 to 80 were studied. The basic unit of length in the simulations is σ while the standard for energy is ϵ. The fundamental unit of time is defined as $t^* = \frac{1}{\sqrt{\epsilon/M\sigma^2}}$, where M is the mass per bead which is set to

the arbitrary value of 1.00. Working within the good solvent regime, $k_BT/\epsilon = 5.0$. The bonded forces are characterized by $k_b/\epsilon = 10,000$ and $l_o/\sigma = 0.875$. The model cantilever spring is retracted at a rate $\frac{dz}{dt}\left(\frac{t*}{\sigma}\right) = 1.25$ or 0.625 and has an equilibrium length $l_p/\sigma = 1.25$. Two values for the probe's stiffness k_p/ϵ are examined, 1.00 and 0.50.

5.2.2 Algorithm

The Brownian dynamics algorithm described in Chapter 4 was employed to investigate the dynamic response of the models to the constant displacement rate, $\frac{dz}{dt}$, applied to one end of the phantom spring. Specifically, the Langevin equation[98, 99]

$$\frac{d^2\vec{R}}{dt^2} = -\zeta\frac{d\vec{R}}{dt} - \vec{\nabla}U + \vec{F}_{rand} \tag{5.3}$$

describes the motion of all of the chain segments except the terminal bead tethered to the substrate. The first term on the right hand side represents the viscous drag on the chain segments as they move through the solvent. ζ is the frictional coefficient and has the arbitrary value of $1.0/t^*$. The second term on the right hand side derives from the interaction of the beads with all non-solvent species. U is the sum of the potentials described above. This term includes the force due to the phantom spring acting on one of the terminal beads. The last term describes the molecule's coupling to the solvent thermal bath such that the random force $\vec{F}_{rand}$ obeys

$$< \vec{F}_{rand} >= 0 \tag{5.4}$$

and

$$\langle \vec{F}_{rand}(t) \cdot \vec{F}_{rand}(t') \rangle = 6k_BT\zeta\delta(t - t'). \tag{5.5}$$

The Box-Muller algorithm[100] provides values for the random forces from the Maxwell distribution $W(\vec{F}_{rand})$.

$$W(\vec{F}_{rand}) = \left(\frac{1}{4\pi\zeta k_B T}\right)^{3/2} exp\left[\frac{-\vec{F}_{rand}^2}{4\zeta k_B T}\right] \tag{5.6}$$

The velocity Verlet integration scheme[99, 101, 102] was used to calculate the motions of the beads with a time step $H/t^* = 0.0001$. Lookup tables were precalculated for all of the forces with bin widths $\Delta l/\sigma = 7.50X10^{-4}$ and $\Delta r/\sigma = 1.09X10^{-3}$ for bond lengths and inter-bead distances, respectively.

Prior to introducing the probe spring into the system ($k_p = 0$), the tethered chain was equilibrated for $t/t^* = 4$. At the beginning of the elongation simulations, the phantom spring is attached to the non-bound terminal chain segment regardless of the location of that bead. The spring is initially oriented perpendicular to the substrate, but during the course of the retraction reorients as per the motion of the chain end. The chains are elongated until a retractive force equal to the force required to stretch a single bond by 1% is reached. Carrying out the simulations to higher elongations results only in probing the uninteresting force response due to stretching our model bonds. This constraint also prevents the occurrence of "phantom" chains because the individual bonds never stretch enough to allow unrealistic bond crossing.

5.3 Results and Discussions

Figure 5.2 illustrates representative snapshots from the simulations for $N = 80$, $k_p/\epsilon = 1.0$, and $\frac{dz}{dt}\left(\frac{t^*}{\sigma}\right) = 1.25$. The retractive force, $F_r(z)$, is approximated as the magnitude of the force due to the elongation of the phantom spring. Thus, this includes contributions from the x and y components as well as the z components

of the force. However, these contributions are only slight and may in fact be expected to play a role in the corresponding experiment. The typical behavior of $F_r(z)$ is given in Figure 5.3 for the full range of values of N with $k_p/\epsilon = 1.0$ and $\frac{dz}{dt}\left(\frac{t^*}{\sigma}\right) = 1.25$. Cutting the extension rate and cantilever stiffness in half produces no noticeable difference in the trends. The primary requirements for these parameters, that $\frac{dz}{dt}$ be small enough to allow the chain to relax and that the probe is considerably more compliant than our model bonds, are thus met. The line shape of each curve in Figure 5.3 indicates that the well-known Langevin[127] equation, eq. (5.7) below, for chain elongation applies to these results.

$$z/L = cot\left(\frac{F_r l_o}{k_B T}\right) - \frac{k_B T}{F_r l_o} \tag{5.7}$$

L is the contour length of the chain. Strictly speaking, this expression applies to chains without pairwise interactions in free-space (no hard-walls, for example). However, as a chain is elongated, the probability of a segment's contact with either the wall or another bead decreases. Thus, the expression nicely reduces the eight curves of Figure 5.3 to one master curve given in Figure 5.4. The solid line represents the theoretical force response calculated with the parameters of the simulations.

The underlying free energy as a function of chain elongation can be elucidated from these dynamic simulations, as put forth by Hummer and Szabo.[128] Considering a system who's behavior is dictated by a time dependent Hamiltonian, they derive a relation between the non-equilibrium trajectories and the equilibrium Boltzmann distribution for the system. From this, they arrive at a histogram estimate of the free energy, given in eq. (5.8).

$$Fe((j-1/2)\Delta z) = -k_B T ln\left(\frac{\Sigma_{i=0}^{n} h_i(j)/\eta_i}{\Sigma_{i=0}^{n} exp(-H(z,i)/k_B T)/\eta_i}\right) \tag{5.8}$$

For a given slice of time i, $h_i(j)$ is the work-based Boltzmann penalty for having the tethered end of the spring at $(j-1/2)\Delta z$, averaged over all trajectories.

$$h_i(j) = \frac{1}{N_t}\Sigma_{k=1}^{N_t} exp(-w_{i,k}/k_BT)\Theta(z_{i,k}) \tag{5.9}$$

Here, N_t is the total number of different trajectories collected (different simulation runs, for example). The total work done on the system up to time slice i in trajectory k is $w_{i,k}$. $z_{i,k}$ is the position of the tethered end of the probe at time slice i in trajectory k. $\Theta(z_{i,k})$ is 1 if $z_{i,k}$ falls within δz of the value centered in bin j and 0 otherwise. η_i is the normalization for the Boltzmann weights.

$$\eta_i = \frac{1}{N_t}\Sigma_{k=1}^{N_t} exp(-w_{i,k}/k_BT) \tag{5.10}$$

$H(zi,i)$ is the time dependent portion of the Hamiltonian. For our particular simulation, this is

$$H(zi,i) = k_p\left(\frac{dz}{dt}t + l_p + z_o - z_i - l_p\right)^2 = k_p\left(\frac{dz}{dt}t + z_o - z_i\right)^2. \tag{5.11}$$

z_o and z_i are the heights above the hard-wall initially and in time slice i, respectively. This Hamiltonian leads to a work function given by

$$w_t = 2k_p\frac{dz}{dt}\left(1/2\frac{dz}{dt}t^2 + z_o t - \int_0^t z_\tau d\tau\right). \tag{5.12}$$

We employ a finite differencing scheme to approximate the work function at time slice i in trajectory k as

$$w_{i,k} = k_p\frac{dZ}{dt}\left(\frac{dz}{dt}t^2 + 2z_o t - \Sigma_{j=1} i(t_j - t_i)(z_{j,k} + z_{j-1,k})\right). \tag{5.13}$$

The explicit algorithm for applying these expressions to find $Fe(z)$ is i) extract $z_{i,k}$, ii) calculate $w_{i,k}$, iii) construct $h_i(j)$, iv) calculate h_i, and finally v) calculate Fe. Figure 5.5 presents $Fe(z)$ for $N = 50$. To minimize the error due to lateral fluctuations in the phantom spring's orientation, $l_p/\sigma = 1.25X10^{-2}$ and $k_p/\epsilon = 10$ while

$\frac{dz}{dt}\left(\frac{t*}{\sigma}\right) = 3.13X10^{-2}$. Fifty independent trajectories where used in the estimation of $Fe(z)$, each beginning with the terminal groups positioned such that they formed the end points of a line perpendicular to the hard-wall. The minimum corresponds to the average end-to-end distances for the unperturbed, tethered chain. The left-most side of the potential was recovered by first pressing the chain-end attached to the probe cantilever closer to the hard-wall before beginning the retraction of the phantom spring.

5.4 Conclusions

In conclusion, we have shown that a simple model combined with the Brownian dynamics simulation algorithm yields behavior consistent with both theoretical expectations and experimental observations of the force response of elongating polymer chains. Further, we show for the first time that the the method of Hummer and Szabo[128] for extracting the underlying free energy of a molecular system from dynamics experiments can be adapted to macromolecular systems. While we have studied the simplest case, our approach is amenable to many more complicated problems. We have carried out preliminary studies of numerous other experimentally interesting constructions. These include removing an adsorbed polyelectrolyte from a charged surface,[117] pulling apart the two strands of model DNA, [118–120, 129, 130] and the extensional melting of single polymer crystals. The results of each of these initial studies show quite good agreement with the corresponding experimental investigations and we hope that future computational explorations will be inspired by the success of the first steps taken here.

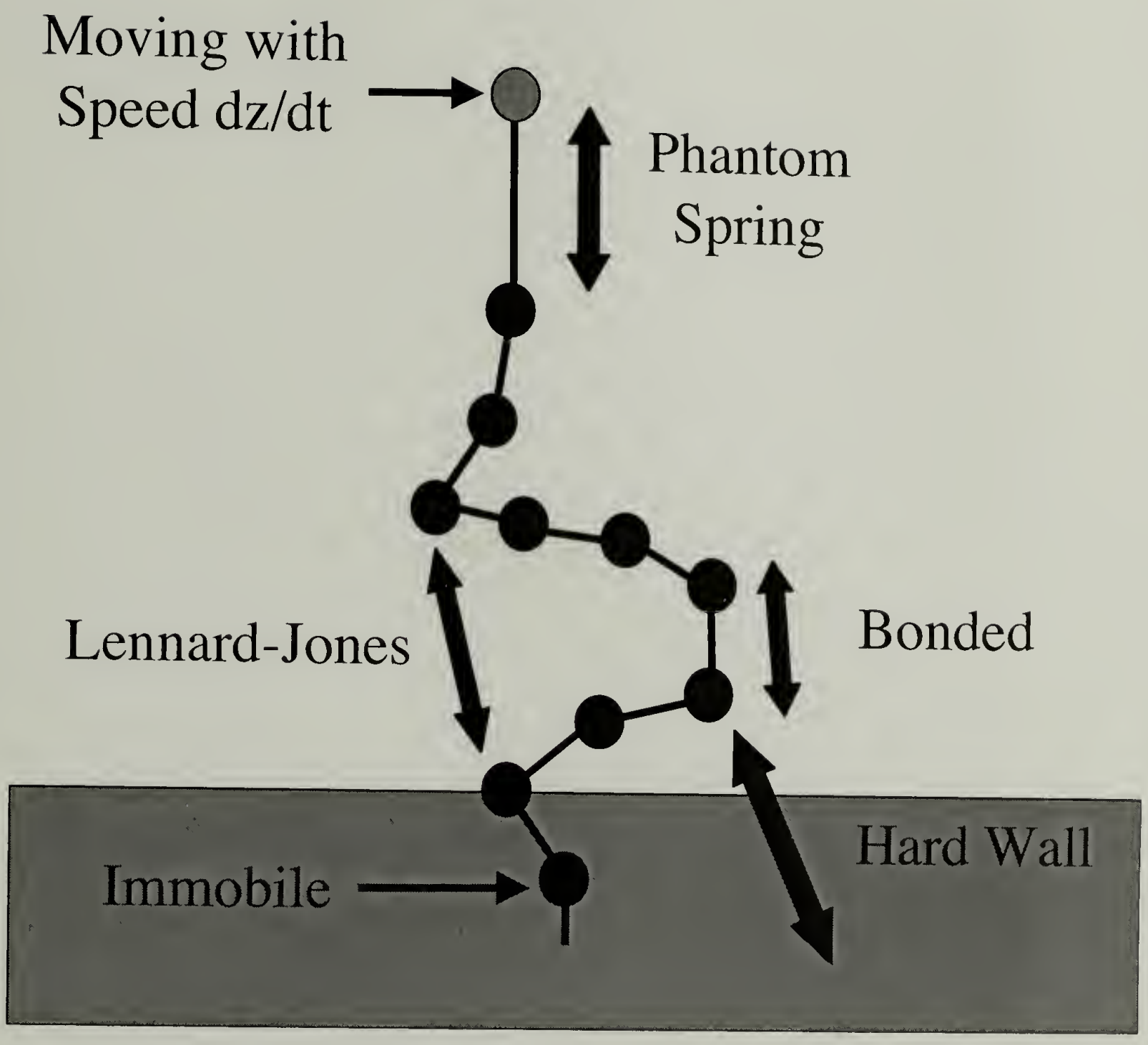

Figure 5.1: The united atom model employed in this study.

Figure 5.2: Typical chain conformational evolution during elongation. Snapshots for $N = 80$ shown.

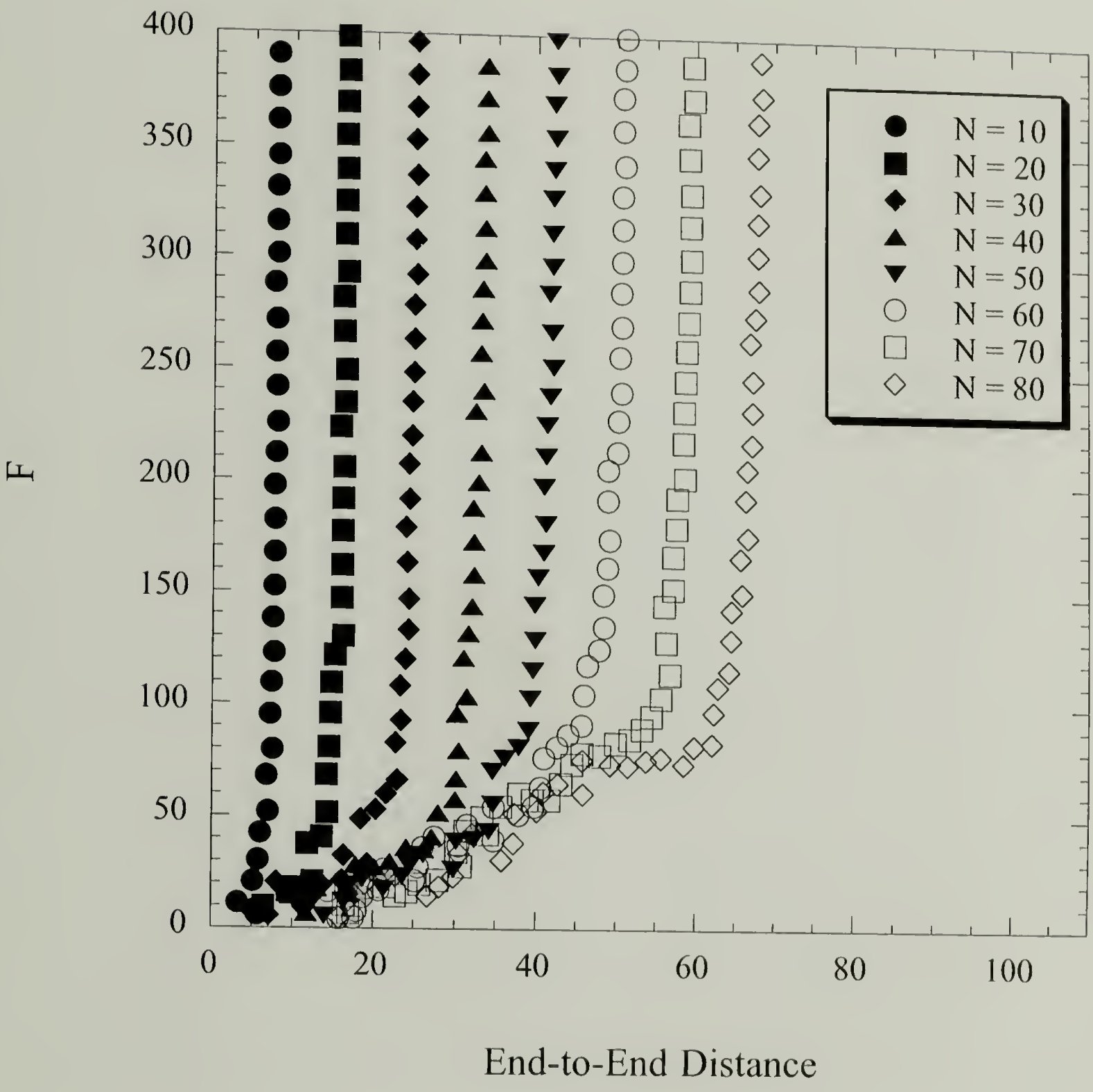

Figure 5.3: Retractive force versus end-to-end distance. Force in units of σ/t^{*2}.

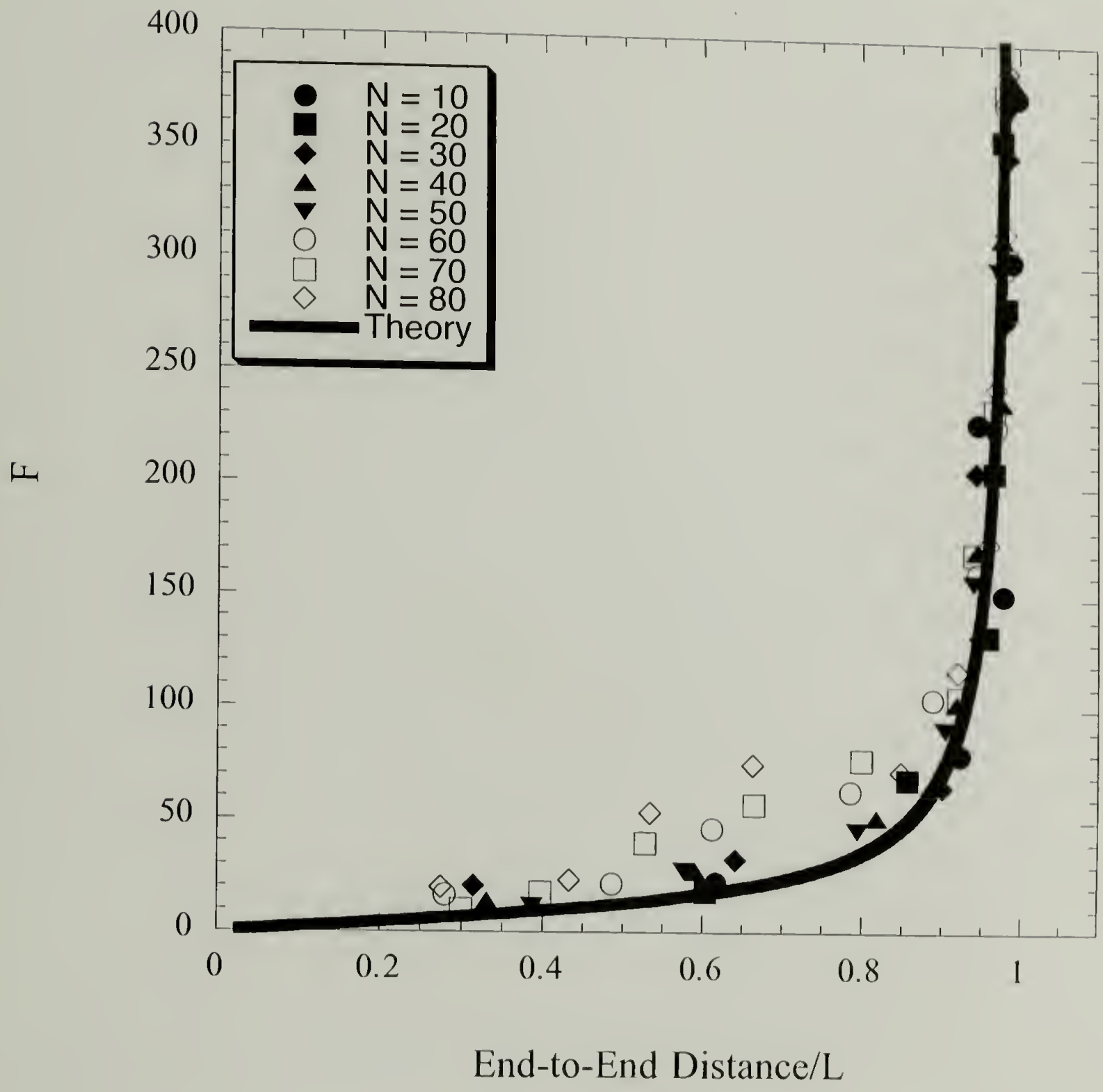

Figure 5.4: Collapse of all data sets onto the Langevin function.

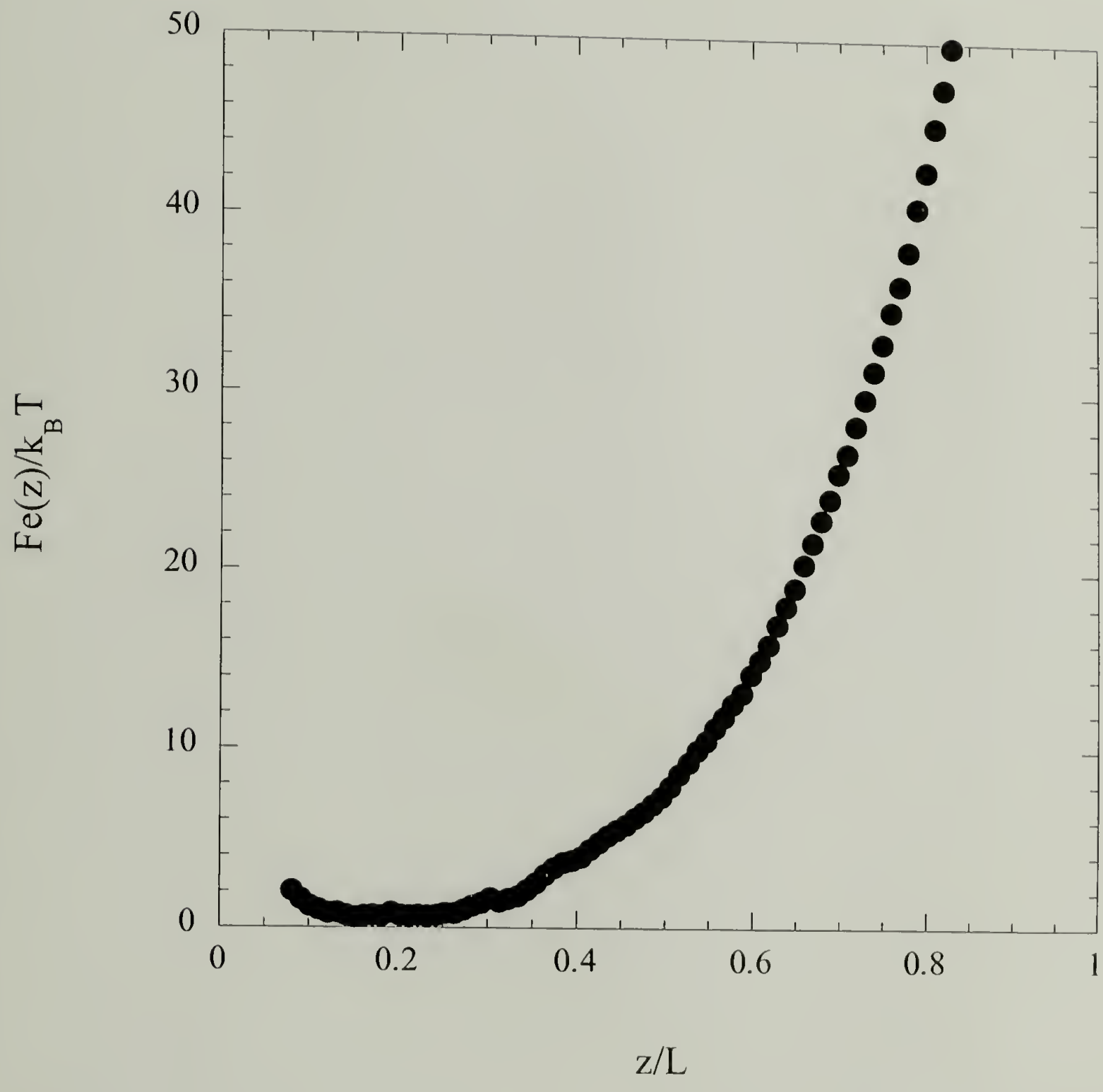

Figure 5.5: Estimate of the underlying free energy as a function of end-to-end distance for a $N = 50$ chain.

APPENDIX A

VARIATIONAL PREDICTION OF THE CRITICAL COMPLEXATION CONDITIONS FOR A POLYELECTROLYTE-DENDRIMER SYSTEM

Here we provide a brief derivation of our prediction for the critical complexation conditions given by eq. (3.8) in the text. The polyelectrolyte chain in the presence of our concentric shell model dendrimer is characterized by the end-to-end vector probability, $G[\vec{R}_e; 0, L]$. $\vec{R}_e \equiv \vec{R}_0 - \vec{R}_L$ is the end-to-end vector and L is the chain contour length. The Edwards' path integral[28, 131] description for $G[\vec{R}_0, \vec{R}_L; 0, L]$ is

$$G[\vec{R}_e; 0, L] = \int_{\vec{R}(0)=\vec{R}_0}^{\vec{R}(L)=\vec{R}_L} D[\vec{R}(s)] e^{\left[\frac{-3}{2b}\int_0^L ds\left(\frac{\delta\vec{R}(s)}{\delta s}\right)^2 - \int_0^L ds\Upsilon[\vec{R}(s)]\right]}. \tag{A1}$$

s is the chain contour position variable and $\vec{R}(s)$ is the location of the chain segment that lies at s along the backbone. $\int_{\vec{R}(0)=\vec{R}_0}^{\vec{R}(L)=\vec{R}_L} D[\vec{R}(s)]$ denotes integration over all possible configurations for $\vec{R}(s)$. The first integral in the exponential captures the chain's connectivity. The second represents the chain segments' non-bonded interactions with itself and the model dendrimer. Explicitly,

$$\int_0^L ds\Upsilon[\vec{R}(s)] = \frac{w}{2b^2}\int_0^L ds\int_0^L ds'\delta[\vec{R}(s)-\vec{R}(s')]$$
$$+\frac{l_B|q^2|}{2b^2}\int_0^L ds\int_0^L ds'\frac{e^{\left[-\kappa|\vec{R}(s)-\vec{R}(s')|\right]}}{|\vec{R}(s)-\vec{R}(s')|}$$
$$-\frac{4\pi l_B|q|}{b}\frac{\Delta i}{\Delta a}\int_0^L ds\frac{e^{\left[-\kappa|\vec{R}(s)|\right]}}{\kappa|\vec{R}(s)|}\int_A^B da|\sigma(a)|a\,Sinh(\kappa a). \qquad \text{(A2)}$$

The first term represents the chain's excluded volume intramolecular interactions. The excluded volume parameter is given by the binary cluster integral:

$$w = \int d\vec{r}\left[1-e^{\frac{-u_\varepsilon}{k_BT}}\right]. \qquad \text{(A3)}$$

$\frac{u_\varepsilon}{k_BT}$ is given by eq. (3.5) in the text. The chain's intramolecular charge-charge repulsion is approximated by the Debye-Hückel potential in the second term. The third term is the attractive interaction between the concentric shells and the chain. Note that we have placed the origin at the center of the model dendrimer.

We are interested primarily in how the interaction between the chain and the model dendrimer affects the complexation requirements and are not interested in the chain's internal degrees of freedom. Therefore we assume that the first two terms in eq. (A2) above, the chain's self-interactions, have the effect of creating an effective step length, b_e, as defined by eq. (3.9) in the text. Thus, the analysis is simplified to investigating a random walk of chain segments that interact with the model dendrimer via the potential in eq. (3.7). With this approximation, the end-to-end vector probability is given by

$$G[\vec{R}_e;0,L] = \int_{\vec{R}(0)=\vec{R}_0}^{\vec{R}(L)=\vec{R}_L} D[\vec{R}(s)]\times$$
$$e^{\left[-\frac{3}{2b_e}\int_0^L ds\left(\frac{\delta\vec{R}(s)}{\delta s}\right)^2+\frac{4\pi l_B|q|}{b}\frac{\Delta i}{\Delta a}\int_0^L ds\frac{e^{\left[-\kappa|\vec{R}(s)|\right]}}{\kappa|\vec{R}(s)|}\int_A^B da|\sigma(a)|a\,Sinh(\kappa a)\right]}. \qquad \text{(A4)}$$

Equivalently, $G[\vec{R}_e;0,L]$ must satisfy

$$\left[\frac{\delta}{\delta L}-\frac{b_e}{6}\vec{\nabla}^2_{\vec{R}_e}+V\right]G[\vec{R}_e;0,L]=\delta(\vec{R}_e)\delta(L) \tag{A5}$$

with the implicit boundary conditions that $G[\vec{R}_e;0,L]=0$ at the surface of our impenetrable shell at Z and $\lim_{\vec{R}_e\to\infty}G[\vec{R}_e;0,L]=0$. V is given by eq. (3.7) in the text.

This differential form may be further simplified into a spherically symmetric eigenvalue problem. We begin to do this by introducing the bilinear expansion of $G[\vec{R}_e;0,L]$,

$$G[\vec{R}_e;0,L]=\sum_{\alpha=1}^{\infty}\Psi^*_\alpha(\vec{R}_L)\Psi_\alpha(\vec{R}_0)e^{-\lambda_\alpha L}, \tag{A6}$$

where $\Psi_\alpha(\vec{R})$ is the α^{th} eigenfunction and λ_α is the corresponding eigenvalue of the operator

$$\hat{H}=\frac{-b_e}{6}\vec{\nabla}^2_{\vec{R}}+V. \tag{A7}$$

Since we are interested in the high molecular weight limit, $L\gg 1$, the ground state Ψ_0 will dominate[131, 132] the sum in eq. (A6). Thus, we have

$$G[\vec{R}_e;0,L]\approx\Psi^*_0(\vec{R}_L)\Psi_0(\vec{R}_0)e^{-\lambda_0 L} \tag{A8}$$

with $\Psi_0(\vec{R})$ satisfying

$$\left[\frac{-b_e}{6}\vec{\nabla}^2_{\vec{R}}+V\right]\Psi_0(\vec{R})=\lambda_0\Psi_0(\vec{R}). \tag{A9}$$

We now take advantage of the spherical symmetry of the problem and obtain:

$$\hat{H}'\Psi_0 = \lambda'\Psi_0 \tag{A10}$$

where we have defined

$$\hat{H}' \equiv -\frac{1}{\Gamma^2}\frac{\delta}{\delta\Gamma}\left(\Gamma^2\frac{\delta(\,)}{\delta\Gamma}\right) + \frac{Ee^{-\Gamma}}{\Gamma}, \tag{A11}$$

$$E \equiv \frac{-24\pi l_B|q|}{\kappa^2 b_e b}\frac{\Delta i}{\Delta a}\int_A^B da|\sigma(a)|a\,Sinh(\kappa a), \tag{A12}$$

$\Gamma \equiv \kappa r$, and $\lambda' \equiv \frac{6\lambda_0}{b_e\kappa^2}$. Unfortunately, there is no known exact analytical solution to this equation for Ψ_0. We therefore proceed with the variational approach. The technique is to guess a functional form for Ψ_0 based upon the boundary conditions stated above for $G[\vec{R}_e; 0, L]$. We choose

$$\Psi_0 = \frac{\Gamma - \Gamma_0}{\Gamma}e^{-\nu\Gamma}. \tag{A13}$$

Here, we have defined $\Gamma_0 \equiv \kappa Z$ with Z being our hard-core radius. The test function is expressed in terms of a variational parameter, ν, that may be adjusted to minimize the energy of the system. Within this approach, λ' is estimated using eq. $(A14)$ below.

$$\lambda' = \frac{\int_{\Gamma_0}^{\infty} d\Gamma\,\Gamma^2\hat{H}'\Psi_0}{\int_{\Gamma_0}^{\infty} d\Gamma\,\Gamma^2\Psi_0} = \frac{\nu^3}{\nu\Gamma_0 + 2}\left[\Gamma_0 + e^{-\Gamma_0}\frac{E}{(\nu+1)^2}\right] \tag{A14}$$

Complexed states are those that correspond to $\lambda' < 0$ with $\nu > 0$. The first term in the product is positive for $\nu > 0$ and the term within the bracket is monotonically

increasing for $\nu > 0$. Thus, the necessary and sufficient condition for a bound state to exist is

$$\left(1 - e^{-2\kappa Z}\right) \frac{12\pi |q| l_B \sigma_e}{\kappa^3 b_e b} > 1. \tag{A15}$$

Finally, we account for lost normalization prefactors by correcting our prediction with the known solution for planar adsorption[28] and obtain eq. (3.8) in the text.

APPENDIX B

THE DESIGN, CONSTRUCTION, AND UTILIZATION OF A DISTRIBUTED MEMORY MULTI-PROCESSOR COMPUTER

General Construction

The bulk of this research was carried out on two 24-node 21164-Alpha based clusters. The art of performing large-scale computer simulations on relatively cheap workstations connected over networks is growing daily and rapidly evolving. Thus, this appendix will be, by virtue of the nature of its subject, outdated shortly after it is written. However, I present the basic design as a starting point for future constructions. The complete parts list is given below. Essentially, these clusters are composed of individual high-end compute node workstations stripped of all i/o components other than a network card and hard drive. They are connected to one another and a head-node via a 10/100 megabit per second network for primary inter-processor communications. A Cyclades serial network connects the compute nodes directly to the head node for backup access to the machines in the event of an Ethernet failure. The operating system is RedHat Linux. The communications library I used in my code is the freely available Parallel Virtual Machine, PVM. Others, such as the Message Passing Interface (MPICH or LAM) exist.

Parts List

24 EV56-LX M/B, 533 MHz 21164CPU, 300W P/S, 2MB cache, HDFD, 7Bay tower Case

48 8x72, 64MB 3.3 Volt 10ns SDRAM-DIMMS

24 3.2GB Quantum IDE Drive

25 Kingston PCI Ethernet Card 10/100mbs

24 Category 5 PVC Ethernet cable - 25ft length

01 Elsa Gloria Synergy II Video Accelerator w/8MB SGRAM

01 40xIDE Toshiba CD-ROM

01 101 Keyboard and Logitech 3 button mouse

01 Red Hat Linux Bundle - including V. 6.0 and documents

01 3Com 3900 24 port stackable 100 Mbps switch

01 24 port serial concentrator Cyclom YeP PCI

24 25 pin to 9 pin NULL modem serial cables

OS Setup

The following steps are required for the initial system setup.

1) Configure and compile the kernel the way you want it.

2) Add a user other than root.

3) Add the following entry to /etc/inittab:

    s1:2345:respawn:/sbin/getty ttyS0 T9600 vt100

4) Add the following entries to /etc/securetty: ttyS0 ttyS1 ttyS2 ttyS3.

5) Add any other software you think you might want on every machine (PVM, MPI, apcd, ect.).

6) Edit /etc/hosts to add a table of hostnames and I.P. numbers.

7) Configure each node with a hostname and I.P. number.

Networks

The clusters are setup as a private network. This has a few advantages such as not having to obtain a block of 48 new I.P. numbers and providing a natural firewall. The head node has two network cards and two I.P. addresses. One card plugs into the cluster's switch, the other into the building's Ethernet network port. This allows the head to communicate with the outside world transparently. The routed daemon is running and I.P. forwarding is set. The default gateway is set and the default gateway device is the card connected to the outside world. The gated daemon is not running.

The compute nodes do not have a default gateway and I.P. forwarding is off. They can communicate with a few machines on the outside world for which I have set explicit route table entries. To accomplish this, edit /etc/rc.d/rc.local with a line like:

route add -net 128.119.70.0 netmask 255.255.255.0 gw 192.168.1.1

Here, 192.168.1.1 is the head node's private net address, 128* is the network I am trying to get to. Issue similar commands on the machines on the outside.

Efficient Use

To make effective use of each processor, I employed two types of parallelization. The simplest and most efficient is a load balancing scheme. I wrote a queuing program that accepts a number of serial jobs and distributes them to the available processors. Once a processor finishes a task, it reports its result to the que and requests another job. If any tasks are available, the queuing software issues a new task. Otherwise the processor leaves the work group and is available for non-qued jobs. Clearly this method is best applied to scenarios where many simulations on relatively small systems are required. Fortunately, many problems such as the dendrimer studies, are amenable to this approach.

The second type of parallelization is more elaborate and requires careful coding to mask the main limitation of distributed computing environments, the network. Large problems can take advantage of multiple processors by decomposing the computational tasks into suitably sized chunks for each node. In general, the most time consuming portion of any simulation is the calculation of the pairwise interactions. Thus, these should be the focus of any parallelization scheme. Depending upon the nature of the system, this step can be broken down in a "data decomposition" partitioning of the problem, such as is described in Chapter 4, or a "spatial decomposition" technique in which each processor is responsible for an a subsection of space. The key to making either approach useful is to ensure that the processors never wait for data from other nodes before proceeding with their calculations. To accomplish this, one must either use a ratio of processors to particles such that each node spends more time calculating than is required for the asynchronous communication over the network, or one must mask the network via use of approximations such as that detailed in Chapter 4.

BIBLIOGRAPHY

[1] Frechet, J. M. J. *Science* **1994**, *263*, 1710.

[2] Jansen, J. F. G. A.; de Brabander-van den Berg, E. M. M.; Meijer, E. W. *Science* **1994**, *266*, 1226.

[3] Jansen, J. F. G. A.; Meijer, E. W.; de Brabander-van den Berg, E. M. M. *Macromol. Symp.* **1996**, *102*, 27.

[4] de Gennes, P.-G.; Hervet, H. *J. Phys. Lett.* **1983**, *44*, L351.

[5] Lescanec, R. L.; Muthukumar, M. *Macromolecules* **1990**, *23*, 2280.

[6] Naylor, A.; Goddard, W.; Kiefer, G.; Tomalia, D. *J. Am. Chem. Soc.* **1989**, *111*, 2339.

[7] Mansfield, M.; Klushin, L. *Macromolecules* **1993**, *26*, 4262.

[8] Murat, M.; Grest, G. *Macromolecules* **1996**, *29*, 178.

[9] Mansfield, M. *Polymer* **1994**, *35*, 1827.

[10] Boris, D.; Rubinstein, M. *Macromolecules* **1996**, *29*, 7251.

[11] Chen, Z.; Cui, S. *J. Macromolecules* **1996**, *29*, 7943.

[12] Lue, L.; Prausnitz, J. *Macromolecules* **1997**, *30*, 6650.

[13] Bauer, B. J.; Topp, A.; Prosa, T. J.; Amis, E. J.; Yin, R.; Qin, D.; Tomalia, D. A. *PMSE Proceedings* **1997**, *77*, 87.

[14] Amis, E. J.; Topp, A.; Bauer, B. J.; Tomalia, D. A. *PMSE Proceedings* **1997**, *77*, 183.

[15] Valachovic, D. E.; Bauer, B. J.; Amis, E. J.; Tomalia, D. A. *PMSE Proceedings* **1997**, *77*, 230.

[16] Meltzer, A.; Tirrell, D.; Jones, A.; Inglefield, P.; Hedstrand, D.; Tomalia, D. *Macromolecules* **1992**, *25*, 4541.

[17] Mansfield, M.; Klushin, L. *J. Phys. Chem.* **1992**, *96*, 3994.

[18] Mourey, T. H.; Turner, S. R.; Rubinstein, M.; Frechet, J. J.; Hawker, C. J.; Wooley, K. L. *Macromolecules* **1992**, *25*, 2401.

[19] Wooley, K. L.; Klug, C. A.; Tasaki, K.; Schaefer, J. *J. Am. Chem. Soc.* **1997**, *119*, 53.

[20] Gorman, C. B.; Hager, M. W.; Parkhurst, B. L.; Smith, J. C. *Macromolecules* **1998**, *31*, 815.

[21] Young, J. K.; Baker, G. R.; Newkome, G. R.; Morris, K. F.; Johnson, C. S. *Macromolecules* **1994**, *27*, 3464.

[22] Briber, R; Bauer, B.; Hammouda, B.; Tomalia, D. *PMSE Proceedings* **1992**, *67*, 430.

[23] Hara, M. *Polyelectrolytes*; Marcel Dekker: New York, 1993.

[24] Milchev, A.; Binder, K. *Macromol. Theory Simul.* **1994**, *3*, 915.

[25] Welch; P. M.; Mathias, L. J.; Lescanec, R. L. *Polymer Preprints* **1996**, *37*, 250.

[26] Metropolis, N.; Rosenbluth, A. W.; Rosenbluth, M. N.; Teller, A. H.; Teller, E. J. *J. Chem. Phys.* **1953**, *21*, 1098.

[27] Zimm, B.; Stockmayer, W. *J. Chem. Phys.* **1949**, *17*, 1301.

[28] Muthukumar, M. *J. Chem. Phys.* **1987**, *86*, 7230.

[29] Yamakawa, H. *Modern Theory of Polymer Solutions*; Harper and Row: New York, 1971.

[30] de Brabander, E. M. M.; Brackman, J.; Mure-Mak, M.; de Man, H.; Hogeweg, M.; Keulen, J.; Scherrenberg, R.; Coussens, B.; Mengerink, Y.; van der Wal, S. *Macromol. Symp.* **1996**, *102*, 9.

[31] Welch, P.; Muthukumar, M. *Macromolecules***1998**,*31*, 5892.

[32] Nisato, G.; Ivkov, R.; Amis, E. J. *Macromolecules***2000**,*33*, 4172.

[33] Mansfield, M. *Macromolecules***2000**, *33*, 8043.

[34] Potschke, D.; Ballauff, M.; Lindner, P.; Fischer, M.; Vogtle, F. *Macrmol. Chem. Phys.***2000**,*201*, 330.

[35] Ballauff, M. *Top. Curr. Chem.***2001**,*212*, 177.

[36] Weigel, F. W. *J. Phys. A* **1977**, *10*, 299.

[37] Hesselink, F. T. J. *J. Colloid Interface Sci.* **1977**, *60*, 448.

[38] Varoqui, R., in *Macro-ion Characterization: From Dilute Solutions to Complex Fluids*; K. S. Schmitz, ed.; ACS: Washington, D.C., **1994**.

[39] von Goeler, F.; Muthukumar, M. *J. Chem. Phys.* **1994**, *100*, 7796.

[40] Muthukumar, M. *J. Chem. Phys.* **1995**, *103*, 4723.

[41] Châtellier, X.; Joanny, J. F *J. Phys. II* **1996**, *6*, 1669.

[42] Muthukumar, M., in *Interfacial Aspects of Multicomponent Polymer Materials*; D. J. Lohse, T. P. Russell, L. H. Sperling, ed.; Plenum Press: New York, New York, **1997**.

[43] Haronska, P.; Vilgis, T. A.; Grottenmüller, R.; Schmidt, M. *Macromol. Theory Simul.* **1998**, *7*, 241.

[44] Muthukumar, M. *Curr. Opinion in Colloid & Interface Sci.* **1998**, *3*, 48.

[45] Bruinsma, R.; Mashl, J. *Europhys. Lett.* **1998**, *41*, 165.

[46] Rudnick, J.; Bruinsma, R. *Biophys. J.* **1999**, *76*, 1725.

[47] Srivastava, D.; Muthukumar, M. *Macromolecules* **1994**, *27*, 1461.

[48] Wallin, T.; Linse, P. *Langmuir* **1996**, *12*, 305; *J. Phys. Chem.* **1996**, *100*, 17873; *J. Phys. Chem. B* **1997**, *101*, 5506.

[49] Kong, C. Y.; Muthukumar, M. *J. Chem. Phys.* **1998**, *109*, 1522.

[50] Matthews, O. A.; Shipway, A. N.; Stoddart, J. F. *Prog. Polym. Sci.* **1998**, *23*, 1 and the references therein.

[51] Margerum, L. D.; Campion, B. K.; Koo, M.; Shargill, N.; Lai, J. J.; Marumoto, A.; Sontum, P. C. *J. Alloys and Compounds* **1997**, *249*, 185.

[52] Kukowska-Latallo, J. F.; Bielinska, A. U.; Johnson, J.; Spindler, R. Tomalia, D. A; Baker, J. R *Proc. Natl. Acad. Sci. USA* **1996**, *93*, 4897.

[53] Bielinska, A.; Kukowska-Latallo, J. F.; Johnson, J.; Tomalia, D. A.; Baker, J. R. *Nucleic Acids Res.* **1996**, *24*, 2176.

[54] Ottaviani, M. F.; Sacchi, B.; Turro, N. J.; Chen, W.; Jockusch, S.; Tomalia, D. A. *Macromolecules* **1999**, *32*, 2275.

[55] Li, Y.; Dubin, P. L.; Spindler, R.; Tomalia, D. A. *Macromolecules* **1995**, *28*, 8426.

[56] Kabanov, V. A; Zezin, A. B.; Rogacheva, V. B.; Gulyaeva, Zh. G.; Zansochva, M. F.; Joosten, J. G. H.; Brackman, J. Macromolecules **1999**, *32*, 1904.

[57] Tomalia, D. A.; Baker, H.; Dewald, J.; Hall, M.; Kallos, G.; Martin, S.; Roeck, J.; Ryder, J.; Smith, P. *Polymer Journal* **1985**, *17*, 117.

[58] de Brabander - van den Berg, E. M. M.; Meijer, E. W. *Angew. chem. Int. Ed. Engl.* **1993**, *32*, 1308.

[59] Armstrong, R. *J. Chem. Phys.* **1974**, *60*, 724.

[60] McQuarrie, D. *Statistical Mechanics*; Harper Collins: New York, 1976.

[61] Binder, K.; Heermann, D. W. *Monte Carlo Simulation in Statistical Physics*, Springer-Verlag: New York, **1992**.

[62] Scherrenberg, R.; Coussens, B.; van Vliet, P.; Edouard, G.; Brackman, J.; de Brabander, E. *Macromolecules* **1998**, *31*, 456.

[63] Skripov, V.P. *Metastable Liquids*; John Wiley: New York, 1973.

[64] Strobl, G. *The Physics of Polymers*; Springer: New York, 1997.

[65] Bassett, D.C. *Principles of Polymer Morphology*; Cambridge Univ. Press: Cambridge, 1981.

[66] Muthukumar, M. *Eur. Phys. J. E* **2000**, *3*, 199.

[67] Storks, K.H. *J. Amer. Chem. Soc.* **1938**, *60*, 1753.

[68] Keller, A. *Phil. Mag.* **1957**, *2*, 1171.

[69] Imai, M.; Mori, K.; Mizukami, T.; Kaji, K.; Kanaya, T. *Polymer* **1992**, *33*, 4451; *Polymer* **1992**, *33*, 4457.

[70] Imai, M.; Kaji, K.; Kanaya, T. *Phys. Rev. Lett.* **1993**, *71*, 4162.

[71] Imai, M.; Kaji, K.; Kanaya, T. *Macromolecules* **1994**, *27*, 7103.

[72] Imai, M.; Kaji, K.; Kanaya, T.; Sakai, Y. *Phys. Rev. B* **1995**, *52*, 12696.

[73] Ezquerra, T.A.; Lopez-Cabarcos, E.; Hsiao, B.S.; Balta-Calleja, F.J. *Phys. Rev. E* **1996**, *54*, 989.

[74] Terrill, N.J.; Fairclough, P.A.; Towns-Andrews, E.; Komanschek, B.U.; Young, R.J.; Ryan, A.J. *Polymer* **1998**, *39*, 2381.

[75] Olmsted, P.D.; Poon, W.C.K.; McLeish, T.C.B.; Terrill, N.J.; Ryan, A.J. *Phys. Rev. Lett.* **1998**, *81*, 373.

[76] Akpalu, Y. A.; Amis, E. J. *J. Chem. Phys.* **1999**, *111*, 8686.

[77] Akpalu, Y. A.; Amis, E. J. *J. Chem. Phys.* **2000**, *113*, 392.

[78] Lauritzen, J.I.; Hoffman, J.D. *J. Res. Natl. Bur. Stand., Sect. A* **1961**, *64*, 73; *J. Res. Natl. Bur. Stand., Sect. A* **1961**, *65*, 297; *J. Appl. Phys.* **1973**, *44*, 4340.

[79] Hoffman, J.D.; Davies, G.T.; Lauritzen, J.I. *Treatise on Solid-State Chemistry, Vol. 3*; Plenum: New York, 1976.

[80] Hoffman, J.D.; Miller, R.L. *Polymer* **1997**, *38*, 3151.

[81] Allegra, G. *J. Chem. Phys.* **1977**, *66*, 5453; Allegra, G.; Meille, S.V. *Phys. Chem. Chem. Phys.* **1999**, *1*, 5179.

[82] *Disc. Faraday Soc.* **1979**, *68*.

[83] Armitstead, K.; Goldbeck-Wood, G. *Advances in Polymer Science, Vol. 100*; Springer-Verlag: New York, 1992.

[84] Point, J.J. *Macromolecules* **1979**, *12*, 770.

[85] Sadler, D.; Gilmer, G.H. *Polymer* **1984**, *25*, 1446; *Phys. Rev. Lett.* **1986**, *56*, 2708; *Phys. Rev. B* **1988**, *38*, 5684.

[86] Doye, J.P.K.; Frenkel, D. *J. Chem. Phys.* **1999**, *110*, 7073.

[87] Liu, C.; Muthukumar, M. *J. Chem. Phys.* **1998**, *109*, 2536.

[88] Paul, W.; Yoon, D.Y.; Smith, G.D. *J. Chem. Phys.* **1995**, *103*, 1702.

[89] Liang, G. L.; Noid, D. W.; Sumpter, B. G.; Wunderlich, B. *Acta Polymer***1993**, *44*, 219.

[90] Kavassalis, T.A.; Sundararajan, P.R. *Macromolecules* **1993**, *26*, 4144.

[91] Doherty, D. C.; Hopfinger, A. J. *Phys. Rev. Letts.***1994**, *72*, 661.

[92] Sundararajan, P.R.; Kavassalis, T.A. *J. Chem. Soc., Faraday Trans.* **1995**, *91*, 2541.

[93] Yamamoto, T. *J. Chem. Phys.* **1997**, *107*, 2653; *J. Chem. Phys.* **1998**, *109*, 4638.

[94] Takeuchi, H. *J. Chem. Phys.* **1998**, *109*, 5614.

[95] Fujiwara, S.; Sato, T. *J. Chem. Phys.***1999**, *110*, 9757.

[96] Gautam, S.; Balijepalli, S.; Rutledge, G.C. *Macromolecules* **2000**, *33*, 9136.

[97] Sommer, J-U.; Reiter, G. *J. Chem. Phys.* **2000**, *112*, 4384.

[98] Sumpter, B.G.; Noid, D.W.; Liang, G.L.; Wunderlich, B. *Adv. in Polym. Sci.* **1994**, *116*, 73.

[99] Allen, M.P.; Tildesley, D.J. *Computer Simulation of Liquids*, Clarendon: Oxford, 1987.

[100] Press, W. H. *Numerical Recipies in C: The Art of Scientific Computing*; Cambridge University Press: New York, 1999.

[101] Swope, W.C.; Andersen, H.C.; Berens, P.H.; Wilson, K.R. *J. Chem. Phys.* **1982**, *76*, 637.

[102] Rapaport, D.C. *The Art of Molecular Dynamics Simulation*, Cambridge University Press: Cambridge, 1995.

[103] Kumar, S.; Bouzida, D.; Swendsen, R. H.; Kollman, P. A.; Rosenberg, J. M. *J. Comput. Chem.* **1992** *13*, 1011.

[104] Organ, S.J.; Keller, A. *J. Mater. Sci.* **1985**, *20*, 1602.

[105] DiMarzio, E.A. *J. Chem. Phys.* **1967**, *47*, 3451.

[106] Sanchez, I.C.; DiMarzio, E.A. *J. Chem. Phys.* **1971**, *55*, 893; *Macromolecules* **1971**, *4*, 677; *J. Res. Nat. Bur. Stands.* **1972**, *76A*, 213.

[107] DiMarzio, E.A.; Guttman, C.M. *J. Appl. Phys.* **1982**, *53*, 6581.

[108] DiMarzio, E.A.; Passaglia, E. *J. Chem. Phys.* **1987**, *87*, 4901, 4908.

[109] Schmidt-Rohr, K.; Spiess, H.W. *Macromolecules* **1991**, *24*, 5288.

[110] Doi, M.; Edwards, S. F. *The Theory of Polymer Dynamics*, Oxford University Press: New York, 1986.

[111] Cornell, W. D.; Cieplak, P.; Bayly, C. I.; Gould, I. R. ; Merz, Jr., K. M.; Ferguson, D. M.; Spellmeyer, D. C.; Fox, ;T.; Caldwell, J. W. ; Kollman, P. A. *J. Am. Chem. Soc.* **1995**, *117*, 5179.

[112] Strick, T.; Allemand, J.-F.; Croquette, V.; Bensimon, D. *Physics Today* **2001**, *October*, 46.

[113] Kamiti, M.; van de Ven, T. G. M. *Macromolecules* **1996**, *29*, 1191.

[114] Jensenius, H.; Zocchi, G. *Phys. Rev. Lett.* **1997**, *79*, 5030.

[115] Kikuchi, H.; Yokoyama, N.; Kajiyama, T. *Chem. Lett.* **1997**, 1107.

[116] Ortiz, C.; Hadziioannou, G. *Macromolecules* **1999**, *32*, 780.

[117] Chatellier, X.; Senden, T. J.; Joanny, J.-F.; Di Meglio, J.-M. *Europhys. Lett.* **1998**, *41*, 303.

[118] Essevas-Roulet, B.; Bockelmann, U.; Heslot, F. *Proc. Natl. Acad. Sci. USA* **1997**, *94*, 11935.

[119] Bockelmann, U.; Essevaz-Roulet, B.; Heslot, F. *Phys. Rev. Lett.* **1997**, *79*, 4489.

[120] Marko, J. F.; Stiggia, E. D. *Macromolecules* **1995**, *28*, 8759.

[121] Kellermayer, M. S. Z. ; Smith, S. B.; Granzier, H. L.; Bustamante, C. *Science* **1997**, *276*, 1112.

[122] Rief, M.; Gautel, M.; Oesterhelt, F.; Fernandez, J. M.; Gaub, H. E. *Science* **1997**, *276*, 1109.

[123] Courvoisier, A.; Isel, F.; Francois, J.; Maaloum, M. *Langmuir* **1998**, *14*, 3727.

[124] Volpert, E.; Selb, J.; Candau, F.; Green, N.; Argillier, J. F.; Audibert, A. *Langmuir* **1998**, *14*, 1870.

[125] Liphardt, J.; Onoa, B.; Smith, S. B.; Tinoco, I.; Bustamante, C. *Science* **2001**, *292*, 733.

[126] Brower-Toland, B. D.; Smith, C. L.; Yeh, R. C.; Lis, J. T.; Peterson, C. L.; Wang, M. D. *Proc. Natl. Acad. Sci. USA* **2002**, *99*, 1960.

[127] Grosberg, A. Y.; Khokhlov, A. R. *Statistical Physics of Macromolecules* AIP Press: New York, 1994.

[128] Hummer, G.; Szabo, A. *Prog. Natl. Acad. Sci. USA* **2001**, *98*, 3658.

[129] Lubensky, D. K.; Nelson, D. R. *Phys. Rev. Lett.* **2000**, *85*, 1572.

[130] Rouzina, I.; Bloomfield, V. A. *Biophys. J.* **2001**, *80*, 882.

[131] Edwards, S.F. *Proc. Phys. Soc.* **1965**, *85*, 613.

[132] de Gennes, P.-G. *Rep. Prog. Phys.* **1969**, *32*, 187.